

**FACULTY
OF MATHEMATICS
AND PHYSICS**
Charles University

BACHELOR THESIS

Martin Vavřík

**Simulation and Reconstruction
of Charged Particle Trajectories in an
Atypic Time Projection Chamber**

Institute of Particle and Nuclear Physics

Supervisor of the bachelor thesis: Mgr. Tomáš Sýkora, Ph.D.

Study programme: Physics

Prague 2025

I declare that I carried out this bachelor thesis on my own, and only with the cited sources, literature and other professional sources. I understand that my work relates to the rights and obligations under the Act No. 121/2000 Sb., the Copyright Act, as amended, in particular the fact that the Charles University has the right to conclude a license agreement on the use of this work as a school work pursuant to Section 60 subsection 1 of the Copyright Act.

In date
Author's signature

I would like to thank my parents and my grandma for supporting me throughout my studies, and my supervisor Tomáš Sýkora and my consultant Hugo Natal da Luz for their encouragement, patience, and valuable insights.

Title: Simulation and Reconstruction of Charged Particle Trajectories in an Atypic Time Projection Chamber

Author: Martin Vavřík

Institute: Institute of Particle and Nuclear Physics

Supervisor: Mgr. Tomáš Sýkora, Ph.D., Institute of Particle and Nuclear Physics

Abstract: In this work, we describe the development of a reconstruction algorithm for atypical Time Projection Chambers (TPCs) that will be used at IEAP, CTU to search for the ATOMKI anomalous internal pair creation [1]. The chambers have an inhomogeneous toroidal magnetic field orthogonal to their electric field, hence we call them Orthogonal Fields TPCs (OFTPCs). This arrangement causes a distortion of the drift inside the chamber and complicates the shape of electron/positron trajectories. We present a few approaches to tackle these problems, the best of which uses a simulated ionization electron drift map for track reconstruction, and Runge-Kutta fit for energy reconstruction. Finally, we show from simulations that, for an ideal charge readout with no multiplication and no noise, and exact knowledge of initial position and direction, we can reach FWHM resolution 1.6 % for electrons, and 2.0 % for positrons without correcting systematic errors dependent on the track parameters.

Keywords: simulation, reconstruction, time projection chamber

Název práce: Simulace a rekonstrukce druh nabitých částic v atypické časově projekční komoře

Autor: Martin Vavřík

Ústav: Ústav čisticové a jaderné fyziky

Vedoucí bakalářské práce: Mgr. Tomáš Sýkora, Ph.D., Ústav čisticové a jaderné fyziky

Abstrakt: V této práci byl vyvinut rekonstrukční algoritmus pro atypickou časovou projekční komoru (TPC), jež bude použita na ÚTEF, ČVUT k hledání anomálie X17 [1] ve vnitřní kreaci páru. Tyto komory mají nehomogenní, toroidální magnetické pole, orientované kolmo k elektrickému, proto je nazýváme TPC s ortogonálními poli (OFTPC). Toto uspořádání způsobuje distorzi driftu v komoře a komplikuje tvar elektronových a pozitronových tracků. Představujeme několik řešení těchto komplikací, z nichž nejlepší využívá simulaci mapy ionizačních elektronů pro rekonstrukci tracků a Runge-Kutta fit pro rekonstrukci energie. Na závěr pomocí simulací demonstrujeme rozlišení (FWHM) 1.6 % pro elektrony a 2.0 % pro pozitrony, za předpokladu ideálního vyčítání náboje bez zesílení a šumu, bez korekce systematických odchylek závislých na parametrech tracků.

Klíčová slova: simulace, rekonstrukce, časová projekční komora

Contents

1 Motivation	3
1.1 ATOMKI Anomaly	3
1.1.1 ATOMKI Measurements	3
1.1.2 Other Experiments	4
1.2 X17 Project at IEAP CTU	6
2 Time Projection Chamber	9
2.1 Charge transport in gases	9
2.1.1 Drift	10
2.1.2 Diffusion	11
2.2 Examples of TPCs	11
2.2.1 The original TPC at PEP-4 at SLAC	11
2.2.2 ALICE TPC	12
2.2.3 CERES/NA45 radial-drift TPC	12
2.2.4 Other interesting radial-drift TPCs	13
2.3 Readout	16
2.3.1 Multi-Wire Proportional Chamber	16
2.3.2 Micro-Pattern Gaseous Detectors	16
2.4 Orthogonal Fields TPC at IEAP CTU	19
2.4.1 Motivation and Associated Challenges	19
2.4.2 Coordinate Systems and Dimensions	20
2.4.3 Magnetic Field Simulation	22
3 Track Simulation	25
3.1 Microscopic Simulation	25
3.1.1 First testing track	26
3.1.2 Grid-like testing sample	26
3.2 Runge-Kutta Simulation	26
3.2.1 Testing sample	29
4 Track Reconstruction	31
4.1 Reconstruction Assuming Steady Drift	31
4.2 Ionization Electron Map	33
4.2.1 Map Simulation	38
4.2.2 Gradient Descent Algorithm	38
4.2.3 Interpolation on the Inverse Grid	39
4.3 Reconstruction testing	40
4.4 Discrete Reconstruction	41
5 Energy Reconstruction	47
5.1 Cubic Spline Fit	47
5.2 Circle and Lines Fit	48
5.2.1 Two-dimensional fit	50
5.2.2 Three-dimensional fit	51
5.2.3 Testing on a Runge-Kutta sample	55

5.3 Runge-Kutta Fit	56
5.3.1 Testing on a microscopic sample	57
Conclusion	63
Future	65
Bibliography	69
List of Figures	75
List of Tables	81
List of Abbreviations	83

1. Motivation

A Time Projection Chamber (TPC)[2] is a gaseous detector that reconstructs charged particle trajectories by measuring the positions and drift times of ionization electrons (and sometimes also ions) created in the gas. The energies of these particles can be inferred from the curvatures of their trajectories in a magnetic field.

The goal of this thesis is to develop an algorithm for the reconstruction of charged particle trajectories and energy in an *atypic* TPC with orthogonal electric and magnetic fields, hereafter referred to as the OFTPC, used in the X17 project at the Institute of Experimental and Applied Physics, Czech Technical University in Prague (IEAP, CTU). Furthermore, we present the results of testing of several (gradually improving) developed algorithms with different samples of simulated data.

The X17 project in IEAP, CTU [3] aims to reproduce measurements of anomalous behavior in the angular correlation distribution of pairs produced by the Internal Pair Creation (IPC) mechanism [4] during the decay of certain excited nuclei (${}^8\text{Be}$ [1, 5], ${}^{12}\text{C}$ [6], and ${}^4\text{He}$ [7, 8]) observed by a team at ATOMKI in Hungary.

1.1 ATOMKI Anomaly

Many different theories propose the existence of *new light boson(s)* that are weakly coupled to ordinary matter [9]. These particles are potential dark matter candidates and could contribute to a solution of other issues with the Standard Model, such as the strong CP problem¹ and the anomalous muon magnetic moment.

A possible way of detecting such bosons with a short lifetime is to observe nuclear transitions of excited nuclei. If a boson was emitted during the transition and subsequently decayed into an electron-positron pair, we could observe this as a peak on top of the standard e^+e^- angular correlation from the Internal Pair Creation (IPC) and the External Pair Creation (EPC).

1.1.1 ATOMKI Measurements

Historically, there were several measurements of the IPC in nuclear transitions in ${}^8\text{Be}$ at Institute für Kernphysik (Frankfurt) [10, 11, 12] and at ATOMKI (Debrecen, Hungary) [13, 14] resulting in different anomalies with invariant mass in the range 5-15 MeV. This motivated the development of a better spectrometer at ATOMKI.

In 2015, a group at ATOMKI observed an anomalous IPC in ${}^8\text{Be}$ [1]. They used the ${}^7\text{Li}(p, \gamma){}^8\text{Be}$ reaction at the $E_p = 1030$ keV proton capture resonance to prepare the 18.15 MeV excited state ($J^\pi = 1^+$, $T = 0$). This state decays predominantly through M1 transitions to the ground state ($J^\pi = 0^+$, $T = 0$) and to the 3.03 MeV state ($J^\pi = 2^+$, $T = 0$) [15].

¹The CP symmetry could be violated in strong interactions according to the current formulation of quantum chromodynamics, but no such violation is observed.

The angular correlation of the e^+e^- pairs created internally in these transitions were measured and compared to the simulation; results from a narrow $E_{\text{sum}} = 18$ MeV region are shown in Fig. 1.1a. The simulation includes boson decay pairs for different boson masses. The disparity parameter y is used to describe the asymmetry of energy between the two particles. It is defined as

$$y = \frac{E_{e^-} - E_{e^+}}{E_{e^-} + E_{e^+}}, \quad (1.1)$$

where E_{e^-} and E_{e^+} are the kinetic energies of the electron and positron.

Their experimental setup was later upgraded and used for new measurements. In 2022 the ${}^8\text{Be}$ anomaly was also measured using the $E_p = 441$ keV resonance to produce the 17.64 MeV excited state ($J^\pi = 1^+$, $T = 1$) which again decays primarily to the ground state and the 3.03 MeV state [15]. The anomaly was also verified for $E_p = 650$ keV and 800 keV where E1 transitions from the direct proton capture dominate [5]. The results for e^+e^- with $E_{\text{sum}} \in [13.5, 20]$ MeV are shown in Fig. 1.1b.

The newer setup was also used in 2021 to study the ${}^3\text{H}(p, e^+e^-){}^4\text{He}$ reaction at $E_p = 510, 610$ and 900 keV [8], inducing direct and resonant capture populating the overlapping first 20.21 MeV ($J^\pi = 0^+$) and second 21.01 MeV ($J^\pi = 0^-$) excited states [16]. The comparison of simulated and measured e^+e^- pair angular correlations in the $E_{\text{sum}} \in [18, 22]$ MeV region is shown in Fig. 1.1c.

In 2022, another anomaly was measured in the ${}^{11}\text{B}(p, e^+e^-){}^{12}\text{C}$ process [6]. The $E_p = 1388$ keV resonance was used to populate the 17.23 MeV excited state ($J^\pi = 1^-, T = 1$) with a large width $\Gamma = 1.15$ MeV [17]. This state decays mainly through E1 transitions to the ground state $J^\pi = 0^+$ and to the 4.44 MeV state $J^\pi = 2^+$. To compensate for energy losses in the target, five energies in the range $E_p = 1.5 - 2.5$ MeV were used. The experimental angular correlation for the 17.23 MeV transition to the ground state is shown in Fig. 1.1d.

Possible explanations of the anomaly include experimental effects, higher order processes in the Standard Model [18, 19] or even a protophobic fifth force mediated by a new 17 MeV boson X17 [20].

1.1.2 Other Experiments

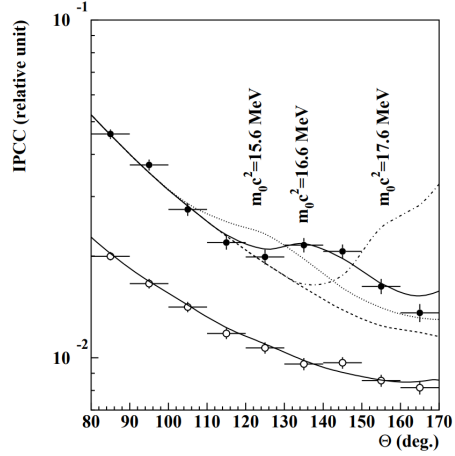
Since the ATOMKI measurements, several experiments have been initiated to attempt to replicate the results and search for the hypothetical X17 particle. The following experiments have already produced results [21].

Two-arm e^+e^- spectrometer in Hanoi

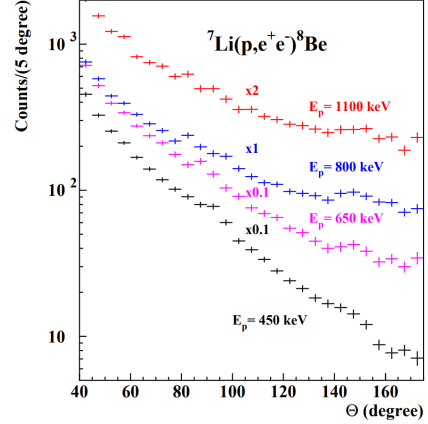
The anomaly in ${}^8\text{Be}$ has been observed with a high ($> 4\sigma$) confidence by a team at the Hanoi University of Sciences for $E_p = 1225$ keV [22]. They built a two-arm spectrometer in collaboration with ATOMKI and calibrated it using the 17.6 MeV M1 transition. The results are shown in Fig. 1.2.

Collisions at Nuclotron in Dubna

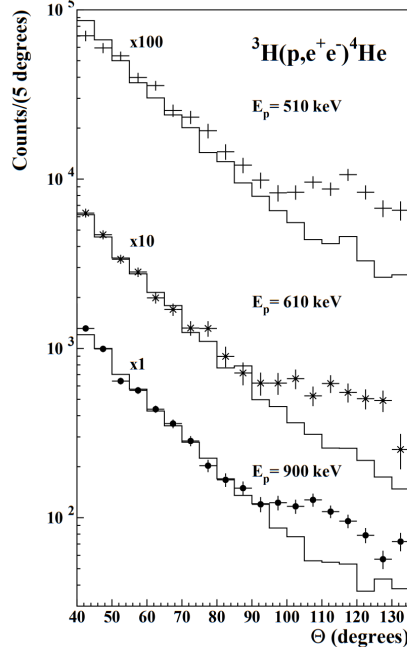
At the Joint Institute for Nuclear Research in Dubna, signal in the form of enhanced structures in the $\gamma\gamma$ spectra at ~ 17 and ~ 38 MeV invariant masses



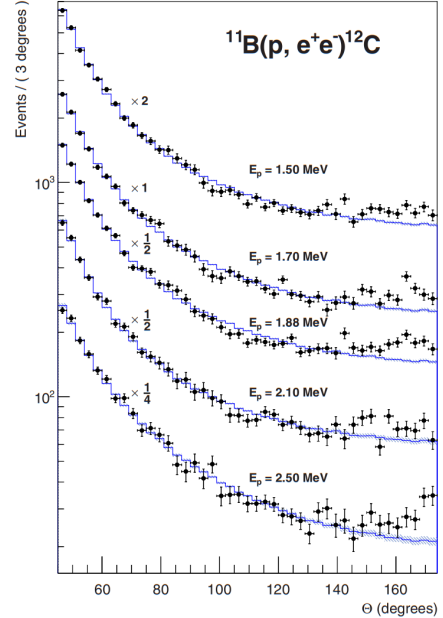
(a) Experimental e^+e^- pair correlations measured in the ${}^7\text{Li}(p, e^+e^-){}^8\text{Be}$ reaction with $|y| \leq 0.5$ (closed circles) and $|y| \geq 0.5$ (open circles) [1].



(b) Experimental e^+e^- pair correlations measured in the ${}^7\text{Li}(p, e^+e^-){}^8\text{Be}$ reaction with the improved setup for different proton beam energies [5].



(c) Experimental e^+e^- pair correlations measured in the ${}^3\text{H}(p, e^+e^-){}^4\text{He}$ reaction with $|y| \leq 0.3$ for different proton beam energies [8].



(d) Experimental e^+e^- pair correlations measured in the ${}^{11}\text{B}(p, e^+e^-){}^{12}\text{C}$ reaction for different proton beam energies [6].

Figure 1.1 The ATOMKI anomalous IPC measured for different nuclei.

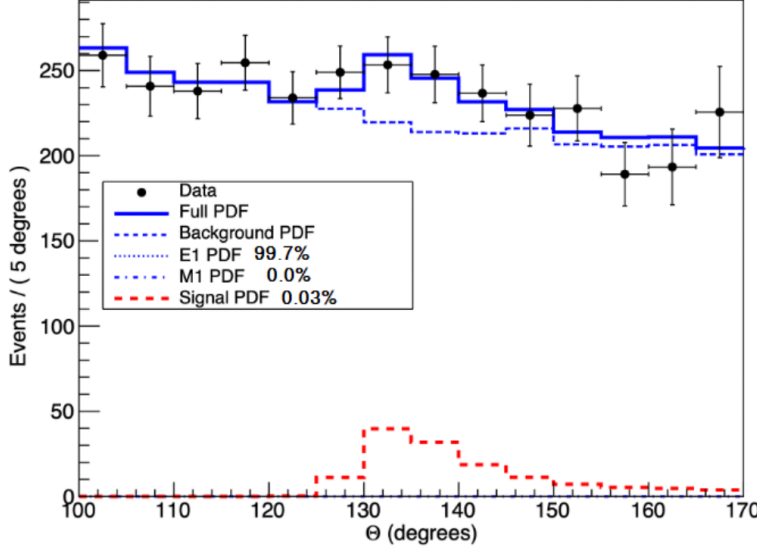


Figure 1.2 Results from the Hanoi spectrometer - angular e^+e^- pair correlations measured in the ${}^7\text{Li}(p, e^+e^-){}^8\text{Be}$ reaction at $E_p = 1225 \text{ keV}$ [22].

for $p + \text{C}$, $d + \text{C}$ and $d + \text{Cu}$ reactions at momenta 5.5, 2.75, and 3.83 GeV per nucleon [23]. Monte Carlo simulations support the conclusion that the signals are a consequence of a decay of unknown particles X17 and E38.

The MEG II (Muon Electron Gamma) experiment

Experiments using the ${}^7\text{Li}(p, e^+e^-){}^8\text{Be}$ reaction were carried out at the Paul Scherrer Institute with the MEG II superconducting solenoid spectrometer [24]. Analysis of the data with $E_p = 1080 \text{ keV}$ exciting both of the resonances (beam fully stopping in the target) found no significant evidence supporting the X17 hypothesis, results are shown in Fig. 1.3. An upper bound (at 90% confidence) on the X17-to- γ branching ratio was set at $1.2 \cdot 10^{-5}$ for the 18.15 MeV state (larger than the ratio $5.8 \cdot 10^{-6}$ obtained by ATOMKI in 2016).

1.2 X17 Project at IEAP CTU

The aim of the X17 project at the Van der Graaff facility of the Institute of Experimental and Applied Physics, Czech Technical University in Prague is to reproduce the results of the original ATOMKI experiments with ${}^7\text{Li}$ and ${}^3\text{H}$ targets using an independent e^+e^- spectrometer. In order to effectively measure the anomaly, we need to reconstruct both the energy and the angular correlation of the e^+e^- pairs. The spectrometer will use three layers of detectors to achieve this – Timepix3 (TPX3) silicon pixel detector and Multi-Wire Proportional Chamber (MWPC) layers for the angle reconstruction and a Time Projection Chamber (TPC) layer for the energy reconstruction. The schematics of the prepared detector is in Fig. 1.4.

The energy of e^+e^- pair produced in the reaction is given by the energy available E_r in the reaction and can be distributed between them arbitrarily. Nonetheless in the decay of the hypothetical X17 particle, electron and positron

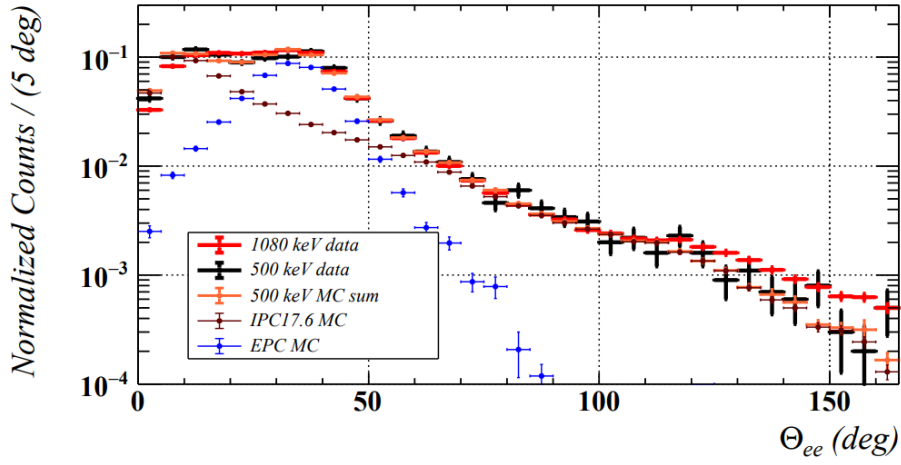


Figure 1.3 Results from the MEG II experiments – angular correlation of e^+e^- pairs with $E_{\text{sum}} \in [16, 20]$ MeV measured in the ${}^7\text{Li}(p, e^+e^-){}^8\text{Be}$ reaction with proton beam energies 500 and 1080 keV. The 500 keV dataset is fitted with Monte Carlo of both the IPC deexcitation and the EPC produced by gammas [24].

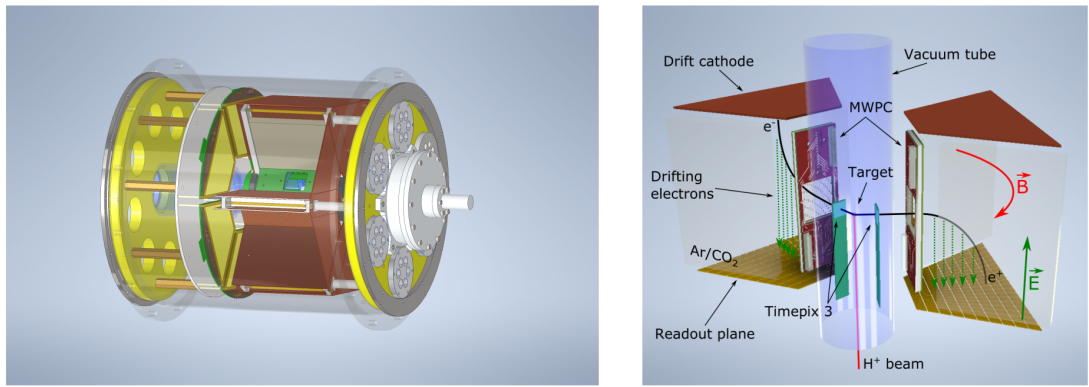


Figure 1.4 Schematics of the detector at the Van der Graaff facility at IEAP, CTU [3].

should have similar energy and we can therefore use a cut $|y| \leq 0.5$ in the disparity parameter (defined in Eq. 1.1). Interesting events should rarely have a particle with an energy below $E_r/4$ (roughly 4 MeV). Electrons with such low energies are scattered significantly by even a thin layer of relatively light material, for this reason the TPX3 layer will be inside of the vacuum tube and the tube will have a thinned aluminum segment or KaptonTM windows.

TPX3 can measure (in each $55 \times 55 \mu\text{m}^2$ pixel of its 256×256 grid) time-of-arrival (ToA) with 1.6 ns precision and time-over-threshold (ToT) which reflects the deposited energy. This potentially allows 3D tracking if we increase the chip thickness at the cost of increased scattering. The layer can reconstruct the reaction vertex and the angular correlation with high precision. Preparatory studies of the angular correlation reconstruction [25], and energy deposition in the sensor [26] have been made.

The layer of MWPCs with sensitive area $40 \times 38 \text{ mm}^2$ will be outside of the beam pipe. It will provide an extra point on the particle trajectory which can help with the estimation of the reaction vertex and improve the TPC performance by providing its entry point.

The TPCs that are the subject of this thesis, are in a magnetic field generated by permanent magnets positioned between them and provide 3D track reconstruction and subsequent momentum and particle identification (its charge, or even type based on its stopping power). They avoid radiative losses thanks to the low density and atomic number of the gas mixture. For the readout, triple Gas Electron Multiplier (GEM) will be used. The magnetic field layout in our TPCs is atypical – orthogonal to the electric field inside the chamber, this is why we call them Orthogonal Fields TPC (OFTPC). Further details about our OFTPCs are provided in Sec. 2.4.

2. Time Projection Chamber

A Time Projection Chamber (TPC) is a gaseous detector that uses the drift times of ionization electrons produced by a charged particle in an (ideally uniform) electric field to reconstruct the particle's 3D trajectory. The 2D projection is measured by an amplification stage at the end of the drift volume. When placed inside a magnetic field (typically parallel to the electric field), the momentum of the incident particle can be inferred from the curvature of its trajectory. Particle identification is also possible using the ionization energy loss inside the TPC (see Fig. 2.1). The following text (including Secs. 2.1 and 2.3) is based primarily on the reviews by Hilke [27] and the Particle Data Group [28].

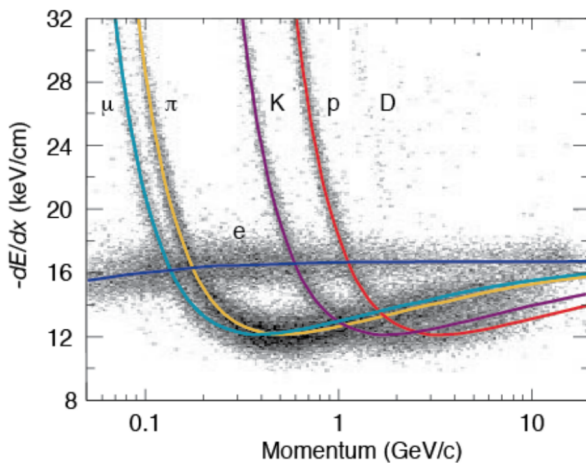


Figure 2.1 Particle identification in the PEP-4 TPC at SLAC based on the energy loss per distance $\frac{dE}{dx}$ in the 80:20 Ar:CH₄ filling at 8.5 atm pressure [29, 30].

Large TPCs are sensitive to small distortions in the electric field (imperfections in the field cage, accumulation of positive ions in the gas volume) and to $\mathbf{E} \times \mathbf{B}$ effects on the drift velocity (see Eq. 2.1 below). Diffusion of the drifting electrons deteriorates the spacial resolution significantly, but it can be reduced up to ~ 10 times by a strong $\mathbf{B} \parallel \mathbf{E}$ field (see Eq. 2.8).

In neutrino and other rare-event experiments, large (up to 600 tons) Liquid Argon TPCs (LArTPCs) are used for particle identification and calorimetry. The ionization electrons can be drifted for many meters with a small diffusion. Scintillation photons are also measured.

2.1 Charge transport in gases

When a charged particle crosses the volume of a TPC, it loses energy by excitation and ionization of the detector gas¹. Most ionizing collision produce a single ionization electron, sometimes a few electrons of secondary ionization are produced near the collision vertex, creating a cluster. In rare cases, the ionization

¹A minimum ionizing particle loses in the order of keV per centimeter traveled at 1 atm pressure.

electron has energy large enough to create a measurable track, such an electron is called a δ -electron.

After their release, the ionization electrons are separated from positive ions by the electric field and they both drift and diffuse in opposite directions towards the electrodes. The charges are accelerated by the electric field inside the chamber, and they lose speed by colliding with the gas particles, quickly reaching a constant (for a given field \mathbf{E}, \mathbf{B}) mean drift velocity. The electrons can be absorbed by electronegative impurities, such as halides, O_2 , and H_2O .

In mixtures with a noble gas component, if the excitation energy of the noble gas is higher than the ionization potential of an admixture, more free electrons can be produced through collisions of the gas particles (so-called Penning transfer) and through absorption of emitted photons.

If the electric field is strong enough, the electrons can cause further ionization and excitation of the gas, leading to the development of a Townsend avalanche [31].

2.1.1 Drift

In many gases (called "hot", e.g., Ar or CH_4), the drift velocity is much greater than that of their thermal motion thanks to a high proportion of elastic collisions. On the other hand, "cold" gases like CO_2 have a higher proportion of inelastic collisions (e.g., thanks to the excitation of rotational and vibrational states) and therefore much lower drift velocity².

The ions produced by the ionization lose a significant portion of their energy during each collision since their mass is close to the mass of the gas particles³. This, together with their large collision cross section, makes their drift velocity much smaller (about three orders of magnitude) and their energy is close to thermal.

The drift is also influenced by the magnetic field. Langevin derived a good approximation for the drift velocity vector:

$$\mathbf{v}_d = \left(\frac{\mathbf{E}}{\|\mathbf{E}\|} + \omega\tau \frac{\mathbf{E} \times \mathbf{B}}{\|\mathbf{E}\| \|\mathbf{B}\|} + \omega^2\tau^2 \frac{\mathbf{E} \cdot \mathbf{B}}{\|\mathbf{E}\| \|\mathbf{B}\|} \cdot \frac{\mathbf{B}}{\|\mathbf{B}\|} \right) \frac{q\tau}{m(1 + \omega^2\tau^2)} \|\mathbf{E}\|, \quad (2.1)$$

where q is the charge of the particle, m is its mass, τ is the mean time between collisions and $\omega = \frac{q}{m} \|\mathbf{B}\|$ is the Larmor frequency. For orthogonal fields $\mathbf{E} \perp \mathbf{B}$, it can be shown that the magnetic field bends the direction of the drift by the so-called Lorentz angle:

$$\tan \psi = -\omega\tau. \quad (2.2)$$

The drift of ions is only negligibly influenced by the magnetic field ($\omega\tau \sim 10^{-4}$ is small due to the low drift velocity). In a standard TPC, \mathbf{E} is parallel to \mathbf{B} and the influence of the magnetic field on the drift is minimal. Without magnetic field, we can write

$$\mathbf{v}_d = \frac{q\tau}{m} \mathbf{E} = \mu \mathbf{E}, \quad (2.3)$$

where μ is called charge mobility.

²It is not always so simple, sometimes, when the electrons are slowed down by inelastic collisions, they reach a minimal cross-section for elastic collisions (so-called Ramsauer-Townsend effect), making them drift faster, due to a less chaotic motion.

³Average energy loss of ions with mass m_i during collision with mass M is $\Delta E = \frac{2m_i M}{(m_i + M)^2}$.

2.1.2 Diffusion

Due to collisions, a cloud of electrons or ions originating from the same point will show a Gaussian density distribution at time t while drifting in the electric field $\mathbf{E} = (0, 0, E_z)$ along the z -coordinate:

$$\rho(x, y, z, t) = (4\pi Dt)^{-\frac{3}{2}} \exp\left(-\frac{x^2 + y^2 + (z - v_d t)^2}{4Dt}\right), \quad (2.4)$$

where the diffusion coefficient D can be expressed as

$$D = \frac{\lambda^2}{3\tau} = \frac{\lambda v_d}{3} = \frac{v_d^2 \tau}{3} = \frac{2\varepsilon \tau}{3m}, \quad (2.5)$$

where λ is the mean free path and ε the mean kinetic energy. The lateral diffusion width σ_x after a drift distance L can be expressed as

$$\sigma_x^2 = 2Dt = \frac{4\varepsilon L}{3qE_z}. \quad (2.6)$$

The minimal diffusion width is given by the lowest possible energy of the particles $\varepsilon_{\text{th}} = \frac{3}{2}kT$ (corresponding to the thermal motion):

$$\sigma_{x, \text{min}}^2 = \frac{2kTL}{qE}. \quad (2.7)$$

For electrons in "cold gases" (e.g., Ar/CO₂ mixture), the diffusion approaches this limit up to a certain field intensity (~ 100 V/cm at 1 atm pressure)⁴. In reality, the transversal diffusion of electrons can differ significantly from their longitudinal diffusion and simulations are necessary to get a precise result. Ions do not change their direction in between collisions significantly, and their diffusion is therefore much smaller.

In most TPCs, the transversal (but not the longitudinal) diffusion is reduced by the magnetic field, since it is parallel to the electric field and curves the diffusing electrons around their mean trajectory:

$$\frac{D_T(B)}{D_T(0)} = \frac{1}{C + \omega^2 \tau_2^2}, \quad (2.8)$$

where C and τ_2 are parameters dependent on the gas used. At low intensity of the magnetic field, we can use an approximation $C \approx 1$ and $\tau_2 \approx \tau$.

2.2 Examples of TPCs

2.2.1 The original TPC at PEP-4 at SLAC

The original TPC used in the PEP-4 experiment at SLAC in the 1980s (Fig. 2.2) was a 2 m × 2 m hollow cylinder with a central cathode that produced a strong

⁴In our detector with 70:30 Ar:CO₂ mixture, the maximal drift distance is $L = 16$ cm, $E = 400$ V/cm, and therefore $\sigma_{x, \text{min}} = 0.45$ mm, quite close to the actual diffusion ~ 1 mm seen in the simulation of the map in Sec. 4.2.

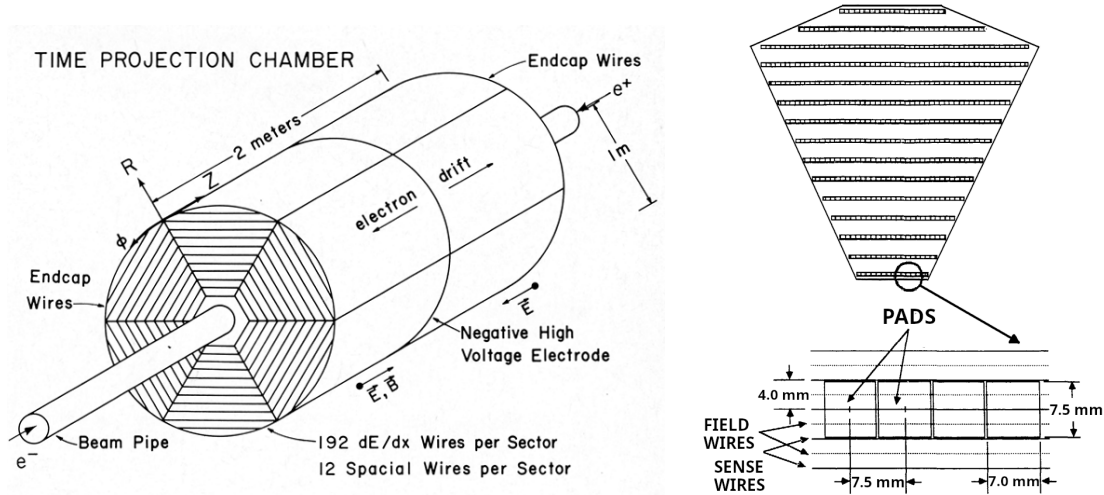


Figure 2.2 Schematic view of the PEP-4 TPC [33]. A charged particle produced in a collision in the beam pipe creates a spiral ionization track in the magnetic field. The central cathode then accelerates ionization electrons towards the endcap anode wires where they are multiplied and read out. A TPC sector with a detailed view of one of the pad rows is shown on the right [34].

electric field 750 V/cm, making the ionization electrons drift towards one of the endcaps [32]. It was filled with a 80:20 Ar:CH₄ mixture at 8.5 atm pressure and placed inside a 0.4 T solenoidal magnetic field. The readout consisted of MWPCs, where electrons are accelerated towards the anode wires fast enough to further ionize the gas and cause an avalanche (details are provided in Sec. 2.3.1). The wires had radial spacing 4 mm, fifteen of the sense wires had the cathode segmented into $7.0 \times 7.5 \text{ mm}^2$ pads 4 mm under them (Fig. 2.2 right). When collecting electrons on the anode wire, signal is induced on the nearest 2-3 cathode pads.

2.2.2 ALICE TPC

The ALICE TPC (Fig. 2.3) is the main detector used for charged particle tracking and recognition in collisions at the ALICE experiment at the CERN LHC [35]. Similarly to PEP-4, it is a hollow cylinder with outer radius 2.5 m and height 5 m. It is placed in a 0.5 T solenoidal magnetic field, and the central cathode generates a 400 V/cm electric field inside the field cage. The gas mixture in the detector is 90:10:5 Ne:CO₂:N₂ (molar fraction), mainly chosen for its higher ion mobility compared to Ar mixtures. In 2020, the readout of the TPC was upgraded from MWPCs to stacks of four GEM foils (principle described in Sec. 2.3.2). This allows reading events continuously at a higher rate.

2.2.3 CERES/NA45 radial-drift TPC

In 1998, the CERES/NA45 (Cherenkov Ring Electron Spectrometer) experiment (Fig. 2.4) at the CERN SPS was upgraded with the first radial-drift TPC (rTPC) to achieve a higher momentum resolution [38]. Unlike a standard TPC, the electric field 600-200 V/cm was arranged radially with the magnetic field (inhomogeneous, up to 0.5 T) by two solenoidal coils with opposite polarity. The

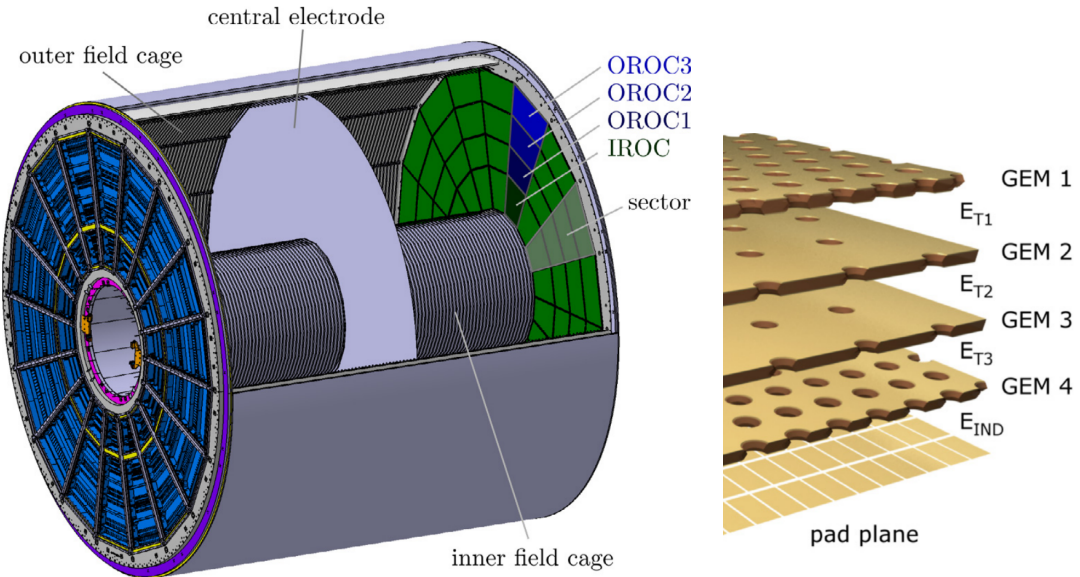


Figure 2.3 Schematic view of the ALICE TPC [36]. The readout at each endcap is divided into 18 sectors, each subdivided into an Inner Readout Chamber (IROC) with one GEM stack and Outer Readout Chamber (OROC) with three GEM stacks. A visualization of a GEM stack is on the right [37].

outward drift of the ionization electrons is affected by the crossing fields as shown in Eq. 2.1 and the drift velocity is not uniform due to the varying electric field. The rTPC was filled with an 80:20 Ne:CO₂ gas mixture, which has relatively small diffusion coefficients and Lorentz angle. The readout was handled by conventional MWPCs (Fig. 2.5).

The field configuration in an rTPC enables a larger number of pads compared to a standard TPC, leading to improved spatial resolution and possibility of larger multiplicity rates. Since the drift time is lower, the detector is faster.

After an algorithm described in this thesis was developed for our OFTPCs at IEAP, CTU, we noticed the similarities with the approach used by the CERES/NA45 rTPC, when accounting for the transport process of charged clusters in the complex fields. The detector hit coordinates (pad, time, and plane) were transformed using look-up tables. The tables were calculated using a Runge-Kutta method to integrate the Langevin approximation of the drift velocity (Eq. 2.1). The drift velocity in the radial field was calibrated using seven parallel laser rays. This calibration was then used to make a correction compared to the Magboltz Monte Carlo drift [39]. Measured mobility differed significantly from a Magboltz simulation. The tracks were fitted using reference tables with hit coordinates of tracks simulated with GEANT Monte Carlo.

2.2.4 Other interesting radial-drift TPCs

After CERES/NA45, several experiments adopted similar field layout for their TPCs. Here, we briefly describe BONuS12 and ALPHA-g rTPCs. Other noteworthy experiments are muon Electric Dipole Moment (muEDM) at the Paul Scherrer Institute [40], and the Solenoidal Tracker (STAR) at Relativistic Heavy Ion Collider (RHIC) featuring a Forward TPC (FTPC) [41].

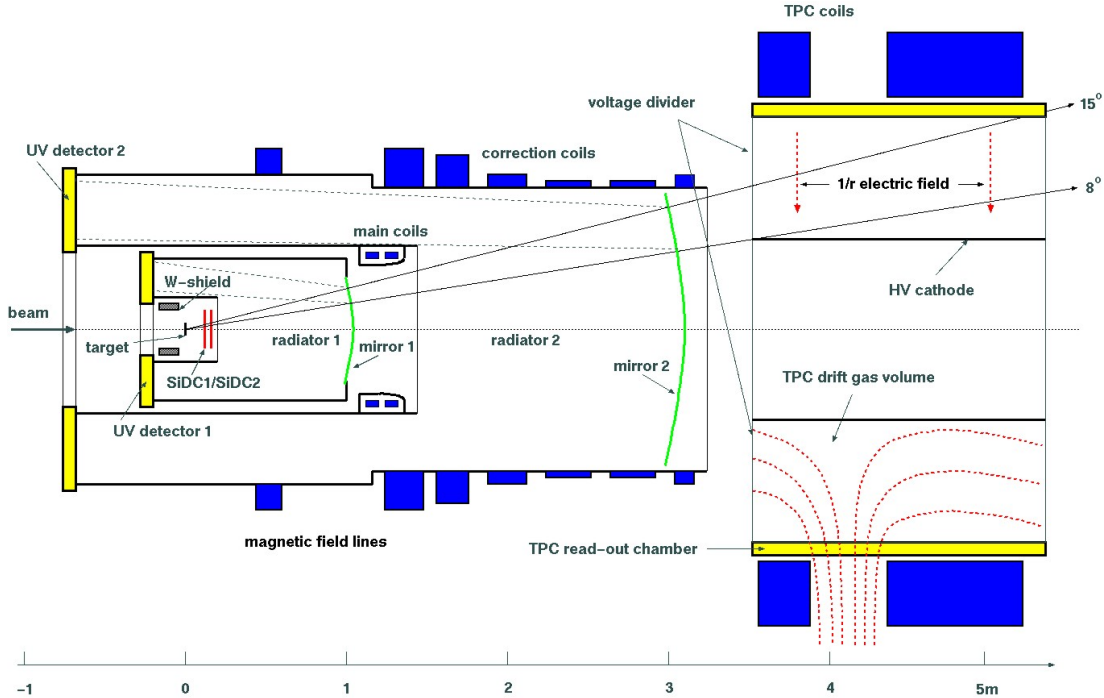


Figure 2.4 Experimental setup of the CERES/NA45 experiment with two Ring Imaging Cherenkov Counters (RICHs) on the left and a rTPC on the right. The magnetic field (red) is generated by two solenoidal coils (blue) with opposite polarity. Produced ionization electrons drift outward radially towards the readout chamber (yellow) [38].

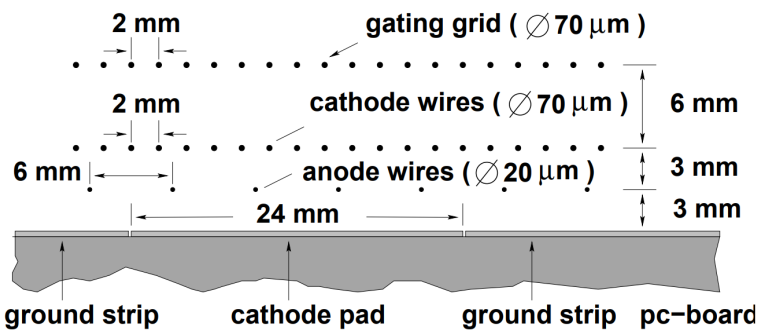


Figure 2.5 Cross section of a CERES/NA45 readout MWPC. The wires are stretched in the azimuthal direction above the pad plane. The gating grid controls the passage of electrons and ions. [38].

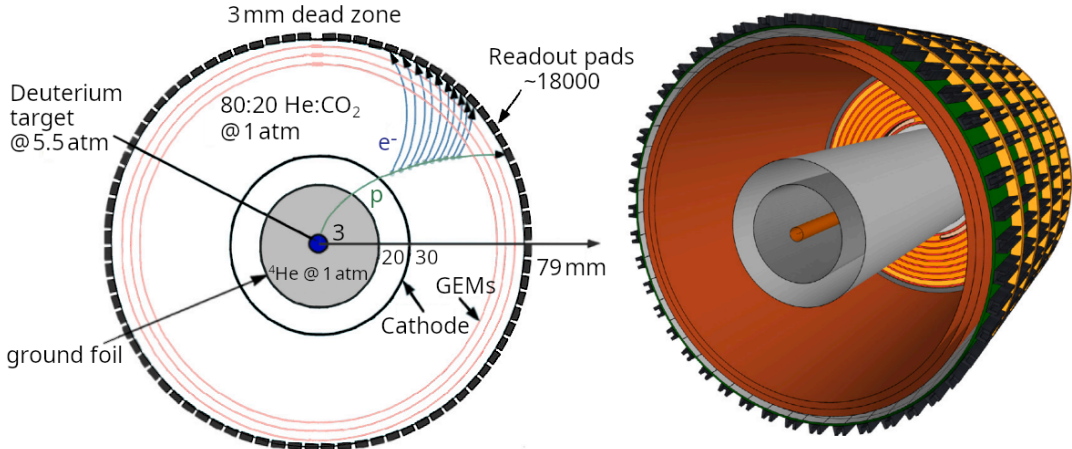


Figure 2.6 Schematic view of the BONuS12 rTPC [42].

BONuS12 rTPC

In 2020, the Barely Off-shell Neutron Structure 12 GeV (BONuS12) experiment used an rTPC (Fig. 2.6) to measure low-momentum spectator protons produced in $e^-d \rightarrow e^-p_sX$ scattering [42]. It was filled with a 80:20 He:CO₂ gas mixture and placed inside a 4 T solenoidal magnetic field, perpendicular to the radial electric field (1100 V/cm on average), tilting the drift (see Eq. 2.2). The amplification used cylindrical triple GEM stacks.

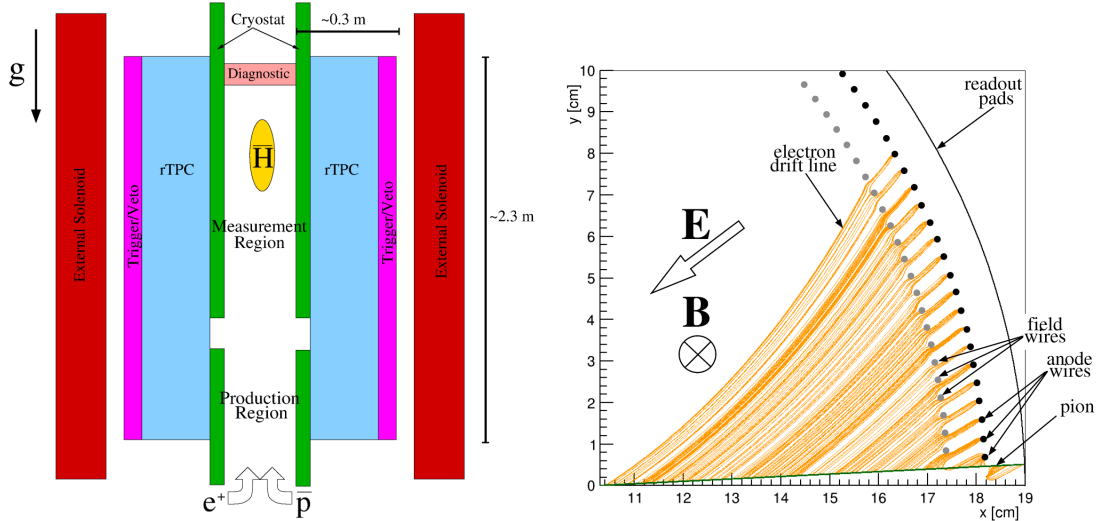
Garfield++ simulations and study of reconstructed tracks have shown that the radial component of the drift velocity almost proportional to the radial electric field, and the r -coordinate can be reconstructed using an analytical formula. Similarly, the azimuthal component is nearly proportional to the radial component, resulting in a largely constant Lorentz angle between the radial and actual direction, and the ϕ -coordinate can be solved analytically. The remaining z -coordinate stays undistorted. The momentum is determined by fitting tracks with a helix, while accounting for the energy losses (the small variability of magnetic field along the z -axis has a negligible effect).

ALPHA-g rTPC

In 2023, the Antihydrogen Laser Physics Apparatus (ALPHA) collaboration published results of measurements of antihydrogen (\bar{H}) annihilation⁵ after release from magnetic confinement, showing that it behaves in a way consistent with gravitational attraction to the Earth [43]. They used a 2.3 m long rTPC (Fig. 2.7a) with a 40 cm outer and 20 cm inner diameter in a 1 T solenoidal magnetic field, and filled with an Ar/CO₂ mixture [44]. The readout consists of an MWPC (Fig. 2.7b). The radial confinement of the cold \bar{H} is achieved with a superconducting octupole magnet, the axial with a set of so-called *mirror* coils.

The r -coordinate of the ionization cluster is reconstructed from the drift time using a tabulated space-time relation. The 3D position of the interaction (cluster) vertex is obtained by matching the wires and pads by drift time using a k-d tree

⁵The main \bar{p} annihilation mode is into several π^\pm and π^0 , only the π^\pm tracks are long enough to be reconstructed. The scattering of π^\pm is not negligible, and photons from π^0 decay create e^+e^- pairs as background.



(a) Sketch of ALPHA-g. Antiprotons and positrons are injected from the bottom and form \bar{H} in a Penning trap while being cooled by the cryostat (green). The annihilation is reconstructed by the rTPC (blue).

(b) Cross section view of the rTPC (Garfield++ simulation). The electrons (orange) produced by a pion track (green) drift towards the anode wires, while influenced by the axial magnetic field. The size of the field and anode wires is exaggerated.

Figure 2.7 Schematic view of the ALPHA-g detector [44].

algorithm. Reconstructed tracks are fitted with a helix using the least squares method [45].

2.3 Readout

2.3.1 Multi-Wire Proportional Chamber

In most TPCs operated in experiments, Multi-Wire Proportional Chamber (MWPC) was used for the readout (Fig. 2.8). The electrons enter the chamber through a cathode grid and get accelerated by a strong electric field towards the parallel, thin anode wires and create an avalanche, multiplying the signal. The trajectory can be reconstructed from the drift time and two coordinates measured using

- a) two segmented cathodes (wires or strips) rotated by 90° or
- b) the ratio of charge collected on two sides of the hit resistive wires.

For high counting rates, the positive ions from the avalanches accumulate, creating a space charge that distorts the electric field. This can be solved by using a gating grid near the readout plane to collect these ions at the cost of introducing a dead time in the detector.

2.3.2 Micro-Pattern Gaseous Detectors

In order to avoid MWPC limitations (e.g., diffusion, wire $\mathbf{E} \times \mathbf{B}$ effect, space charge effects), a family of Micro-Pattern Gaseous Detector (MPGD) technologies are being developed. The readouts can reach higher spatial resolution (down to $30\text{ }\mu\text{m}$) with faster response time (ns range) and much higher rate capability.

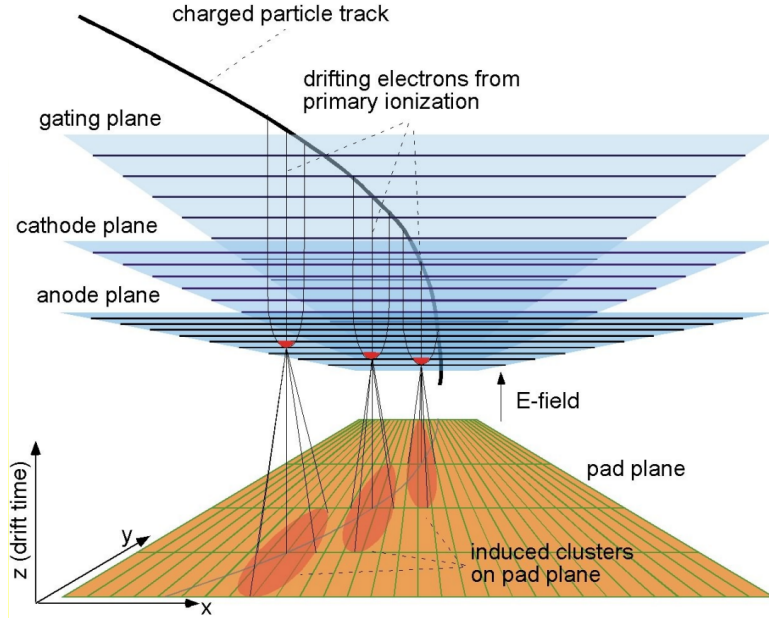


Figure 2.8 Schematic view of the ALICE MWPC readout (working principle) [46].

Gas Electron Multiplier

A Gas Electron Multiplier (GEM) is a thin metal-coated polyimide sheet with a dense pattern of small, chemically etched holes (Fig. 2.9). The amplification is achieved by applying voltage across the metal layers and placing the foil between two moderate uniform electric fields. This creates a strong electric field inside the holes that accelerates the incoming electrons and causes avalanches (see Fig. 2.10). Some charges may land on the dielectric surfaces due to diffusion, modifying the field and affecting gain.

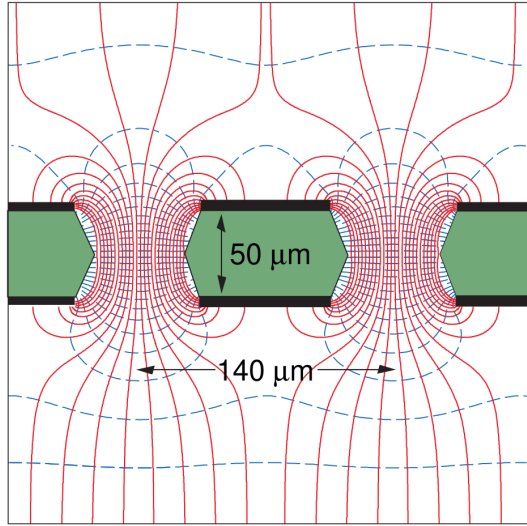
Double or triple stacks of GEMs are usually used to create a sufficient gain while maintaining stability (reducing discharges). From the last foil, the electrons drift to a segmented anode where the signal is read. The ion backflow is reduced compared to MWPC.

A cheaper alternative (especially for large area coverage) is a THick GEM (THGEM) with a \sim 10-fold upscaling of geometrical parameters. It can be made by mechanically drilling holes into a standard Printed Circuit Board (PCB) and creating a circular rim around the holes by etching the metal coating.

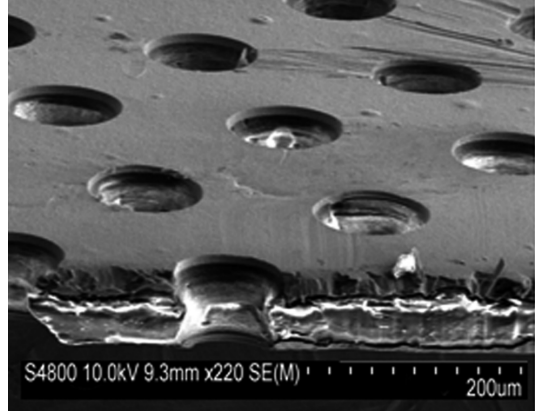
Micromegas

In a MICRO-MEsh GAseous Structure (Micromegas) electrons pass through a fine mesh (made out of very thin wires) into a narrow amplification gap where they are multiplied in the high field and read as a signal on the segmented anode (Fig. 2.11a). Very high field ($30\text{-}80\text{ kV/cm}$) is necessary to achieve sufficient gain. Ion backflow is heavily suppressed by the mesh.

A Timepix chip (a high granularity pixel detector) can be used for the readout anode to achieve the best spatial resolution, making an integrated readout called GridPix (Fig. 2.11b). Thanks to the high spatial resolution, it is possible to distinguish individual electron clusters, which enables a new method of particle identification.



(a) A schematic view of a GEM cell with its typical dimensions, electric field lines (red), and equipotentials (blue) [28].



(b) A scanning electron microscope image of a GEM foil [47].

Figure 2.9 Gas Electron Multiplier (GEM).

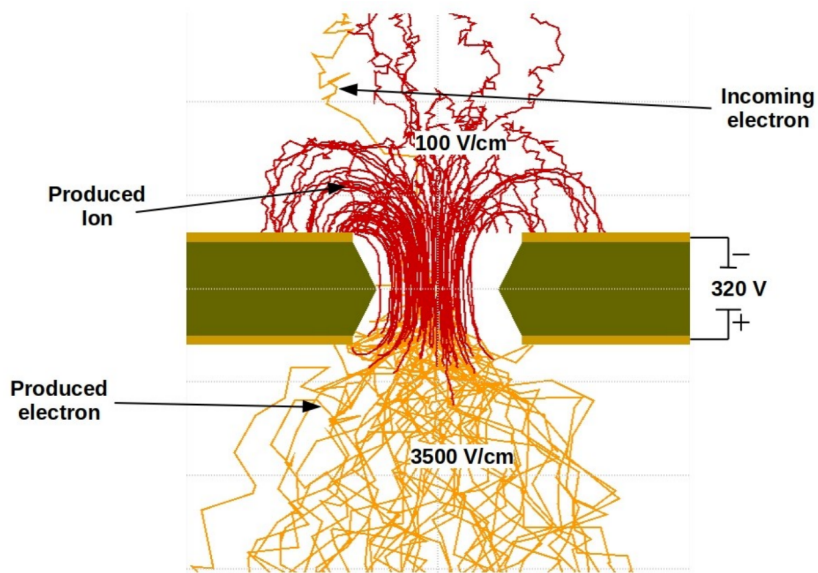


Figure 2.10 Garfield simulation of an avalanche in a GEM hole [48]. An incoming electron (orange) is accelerated in the strong electric field of the GEM and causes further ionization multiplying the number of free electrons (orange). Most of the produced cations (red) are captured by the GEM cathode.

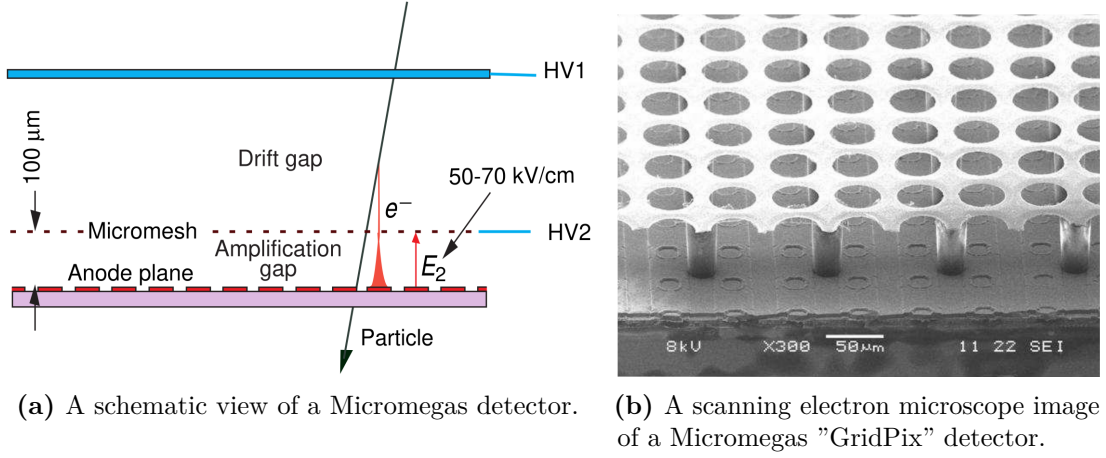


Figure 2.11 MICRO-MEsh GAsous Structure (Micromegas) [28].

Other MPGDs

A Resistive Plate WELL (RPWELL) consists of a THGEM with only the top side metal-coated, mounted on a resistive film deposited on a thin isolating sheet (which is read out similarly to a Resistive Plate Chamber (RPC)). Due to the higher field in the closed holes of the THGEM, a higher gain can be reached for the same voltage. A Micro-RWELL (μ -RWELL) is a similar architecture with ~ 7 times smaller pitch (distance between holes). These options provide a better spark resistance and could allow to cover large areas for a lower cost.

A Micro-Pixel Gas Chamber (μ -PIC) is a PCB with anode strips on one side and orthogonal cathode strips on the other. The cathode has a resistive coating and a regular pattern of uncoated regions with anode "dots" penetrating the PCB at the centers.

2.4 Orthogonal Fields TPC at IEAP CTU

At IEAP, CTU, we are going to use six identical atypical TPCs with inhomogeneous toroidal magnetic field **orthogonal** to the electric field, hereafter referred to as Orthogonal Fields TPC (OFTPC). It has the shape of isosceles trapezoidal prism with a height of 16 cm with triple-GEM readout on one of its bases. Dimensions of the OFTPC are discussed in detail in Sec. 2.4.2 below. Throughout this thesis, we assume a uniform electric field along the z axis with $E_z = -400 \text{ V/cm}$. Measured particles enter the OFTPC through a window after crossing the MWPC.

2.4.1 Motivation and Associated Challenges

The reasons for the unusual field layout are mostly related to construction feasibility:

- we use permanent magnets instead of a solenoid and parallel fields are difficult to accomplish this way,
- granularity of the TPC readout is limited in order to fit one SAMPA/SRS hybrid in each sector – parallel fields would bend the trajectories parallel to

the readout requiring more pads and different architecture.

In this thesis, we will show that such a setup can reach a similar energy resolution as common cylindrical TPCs while reducing the overall cost.

The layout introduces two complications to the track reconstruction – the trajectory in inhomogeneous field is not circular and the drift is distorted by the magnetic field as shown in Eq. 2.1(in our case $\omega\tau \approx 0.08^6$). We will deal with these effects in the upcoming chapters.

The diffusion in such setup is larger since parallel orientation reduces diffusion by curling the electrons in the x - y direction (see Eq. 2.8), but for our relatively weak magnetic field and short drift distance, the difference is negligible.

2.4.2 Coordinate Systems and Dimensions

In order to describe events in our detector, we use three distinct spaces: the detector space \mathcal{D} , the readout space \mathcal{R} and the pad space \mathcal{P} . Each space is later used to represent ionization electrons at different stages of the detection process: their creation in the gas, their final position when hitting the readout plane, and finally their representation in the discrete pad space.

Detector Space

The detector space \mathcal{D} represents the physical space of our detector. We describe it using Cartesian coordinates (x, y, z) . The z -axis is the detector's axis of symmetry, with its negative direction aligned with the proton beam. The origin $(0, 0, 0)$ is located at the center of the irradiated target. The positive x -axis passes through the center of one the OFTPCs along the intersection of its two planes of symmetry. The y -axis is then chosen to maintain a right-handed coordinate system.

Since the detector has a hexagonal symmetry, we use only one of its sectors in this work – the first sector $\mathcal{D}_1 \subset \mathcal{D}$ which is defined by the condition:

$$(x, y, z) \in \mathcal{D}_1 \Leftrightarrow |y| \leq x \tan \frac{\pi}{6}. \quad (2.9)$$

Simulations in this sector can be applied to all sectors by rotating the coordinates accordingly. The volume of the OFTPC in this sector, which has the shape of a trapezoidal prism, has these boundaries:

$$x \in [x_{\min}, x_{\max}] = [6.51 \text{ cm}, 14.61 \text{ cm}], \quad (2.10)$$

$$z \in [z_{\min}, z_{\max}] = [-8 \text{ cm}, 8 \text{ cm}], \quad (2.11)$$

$$y_{\max}(x_{\min}) = -y_{\min}(x_{\min}) = 2.75 \text{ cm}, \quad (2.12)$$

$$y_{\max}(x_{\max}) = -y_{\min}(x_{\max}) = 7.45 \text{ cm}, \quad (2.13)$$

where $y_{\max}(x)$ is the maximal value of the y -coordinate for a given x . The readout is located at $z = 8 \text{ cm}$; for some purposes, we also define the distance to the readout $d_r = 8 \text{ cm} - z$ as an alternative to the z -coordinate. The OFTPC window has width 3.8 cm and height 4.0 cm.

⁶This is the approximate value in the strongest field based on charged mobility computed from the fitted drift velocity in Sec. 4.1.

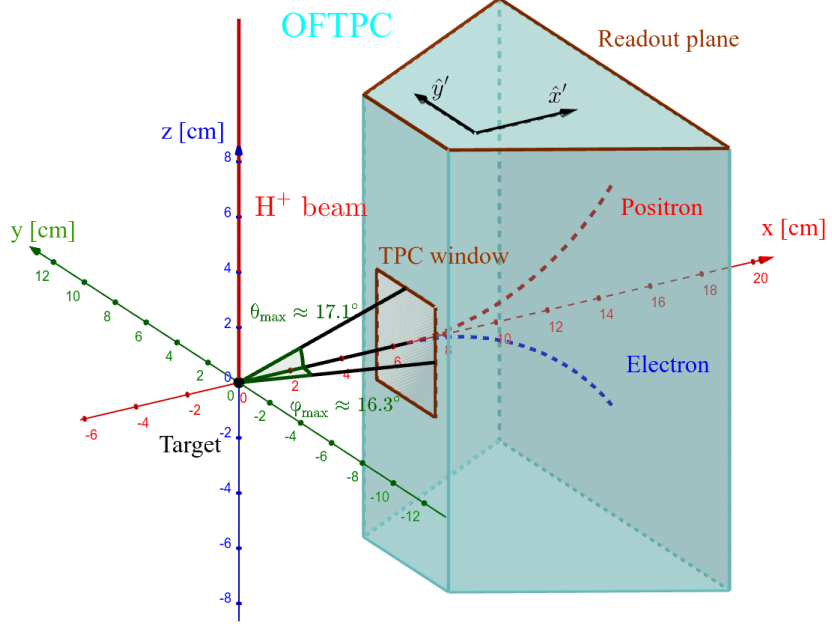


Figure 2.12 Schematics of the first sector OFTPC with detector space coordinates. Made with GeoGebra®.

We also use spherical coordinates (r, θ, φ) with the elevation angle θ measured relative to the xy plane. Angles θ and φ are useful when describing the direction of e^+/e^- tracks. Their maximal values considered for the initial direction in simulations are $\theta_{\max} \approx 17.1^\circ$ and $\varphi_{\max} \approx 16.3^\circ$ as shown in Fig. 2.12.

Readout Space

The readout space \mathcal{R} represents the drift time and final positions of ionization electrons as measured by an ideal continuous readout. We describe it using coordinates (x', y', t) , where x' and y' correspond to the detector coordinates at the readout plane ($z = 8$ cm). The drift time t is approximately proportional to the distance to the readout d_r .

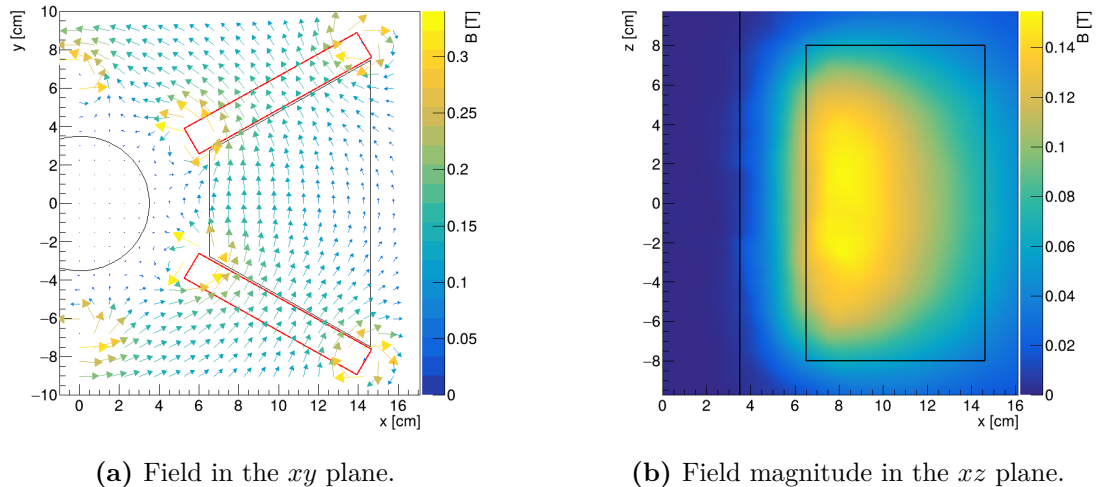
Pad Space

The pad space \mathcal{P} represents the time bin and pad number of ionization electrons as measured by an ideal discrete readout:

$$\mathcal{P} = \{(n_{\text{pad}}, n_t) \in \mathbb{N}^2 \mid n_{\text{pad}} \leq 128\}. \quad (2.14)$$

It is a discretization of a certain volume in \mathcal{R} that can be obtained from simulations.

The readout of the OFTPC will consist of 128 rectangular pads arranged in a staggered pattern. Parameters of the pad layout are shown in Fig. 2.13. The bottom left corner of n -th pad has coordinates $(x_{1,n}, y_{1,n})$, the top right $(x_{2,n}, y_{2,n})$ and its center has coordinates $(x_{c,n}, y_{c,n})$. The gap between neighboring pads is $g = 0.08$ cm, we consider it being shared equally between the neighboring pads. Time will be read out in discrete bins of size $t_{\text{bin}} = 100$ ns.



(a) Field in the xy plane.

(b) Field magnitude in the xz plane.

Figure 2.14 Magnetic field simulation results. The OFTPC volume and the vacuum tube are marked with black lines, the magnets are marked with red lines. In current design of the real detector, magnets are slightly shifted compared to the simulation.

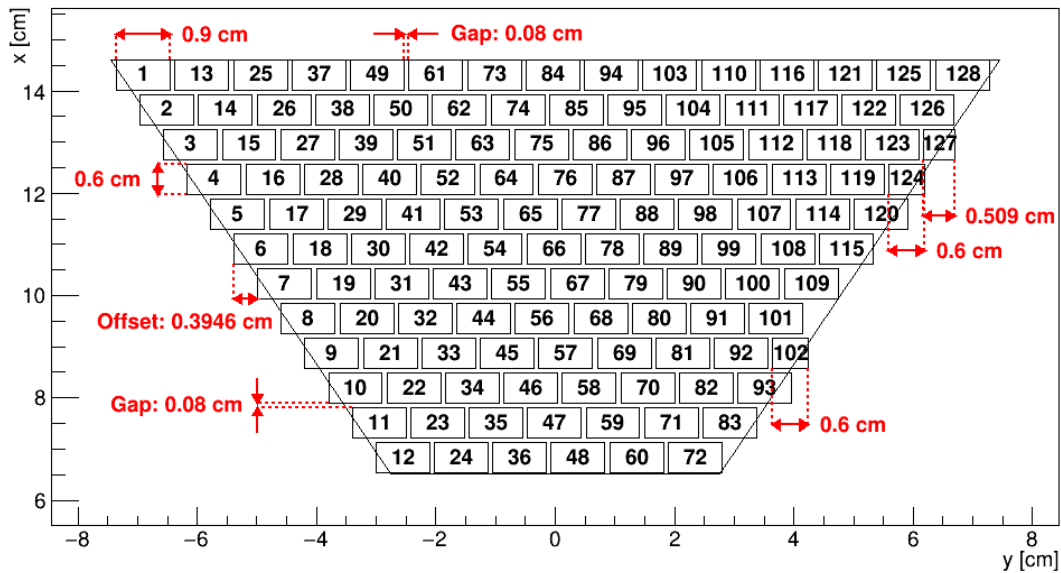


Figure 2.13 Pad layout of the OFTPC and its parameters. Pads 102, 124 and 127 are irregular, the rest has the same dimensions.

2.4.3 Magnetic Field Simulation

The magnetic field inside our detector is produced by six permanent magnets. It was simulated using Ansys Maxwell [49] which gives us values on a regular grid. Visualization of the magnetic field is shown in Fig. 2.14. Whenever we need to work with values outside this grid, we use trilinear interpolation described below.

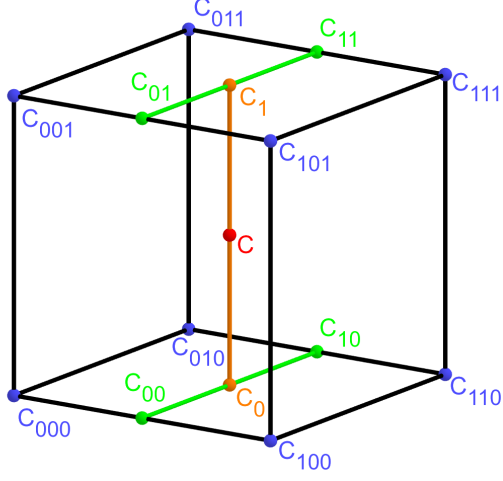


Figure 2.15 Visualization of trilinear interpolation as a composition of linear interpolations (inspired by [50]). We want to interpolate the value in the red point \mathbf{C} . First we interpolate between the four pairs of blue points sharing the last two indices along the x -axis (Eq. 2.15), then between the two pairs of the resulting green points along the y -axis (Eq. 2.16) and finally between the two resulting orange points along the z -axis to get the final red value (Eq. 2.17). Made with GeoGebra®.

Trilinear Interpolation

Trilinear interpolation is a 3D generalization of linear interpolation⁷. It can be used to interpolate a function whose values are known on a regular grid with rectangular prism cells. We use this simple method for interpolating the magnetic field, and it is later used in Sec. 4.2.2 to interpolate the Ionization Electron Map, a key component of our track reconstruction algorithm. In both cases, we use a regular cubic grid (also known as a Cartesian grid).

Let us consider a cell of our regular grid (a cube) with an edge of length a containing the point $\mathbf{C} = (x, y, z)$ where we want to interpolate a function $f: \mathbb{R}^3 \rightarrow \mathbb{R}$. We know the values of this function at the vertices of the cell $\mathbf{C}_{ijk} = (x_0 + ia, y_0 + ja, z_0 + ka)$, where $\mathbf{C}_{000} = (x_0, y_0, z_0)$ is the origin of the cell, and $i, j, k \in \{0, 1\}$ are indices. We also define the points $\mathbf{C}_{ij} = (x, y_0 + ia, z_0 + ja)$ and $\mathbf{C}_i = (x, y, z_0 + ia)$. Then the interpolated value $\hat{f}(\mathbf{C})$ can be calculated as a composition of three linear interpolations (see Fig. 2.15):

$$\hat{f}(\mathbf{C}_{ij}) = (1 - x_d) f(\mathbf{C}_{0ij}) + x_d f(\mathbf{C}_{1ij}), \quad (2.15)$$

$$\hat{f}(\mathbf{C}_i) = (1 - y_d) \hat{f}(\mathbf{C}_{0i}) + y_d \hat{f}(\mathbf{C}_{1i}), \quad (2.16)$$

$$\hat{f}(\mathbf{C}) = (1 - z_d) \hat{f}(\mathbf{C}_0) + z_d \hat{f}(\mathbf{C}_1), \quad (2.17)$$

where x_d , y_d , and z_d are given as follows:

$$x_d = \frac{x - x_0}{a}, \quad y_d = \frac{y - y_0}{a}, \quad z_d = \frac{z - z_0}{a}. \quad (2.18)$$

We can also write

$$\hat{f}(\mathbf{C}) = \sum_{i,j,k \in \{0,1\}} t_x^i t_y^j t_z^k f(\mathbf{C}_{ijk}), \quad (2.19)$$

⁷Linear interpolation in point $x \in (x_1, x_2)$ of a function $f: \mathbb{R} \rightarrow \mathbb{R}$ known in points $x_1 < x_2$ is the convex combination $\hat{f}(x) = (1 - x_d)f(x_1) + x_d f(x_2)$, where $x_d = \frac{x - x_1}{x_2 - x_1} \in (0, 1)$.

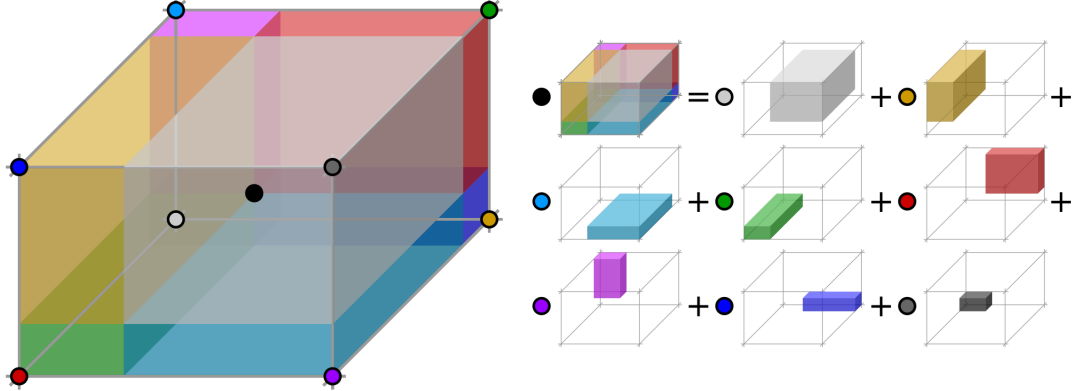


Figure 2.16 Geometric interpretation of trilinear interpolation as expressed in Eq. 2.19. The colored dots represent the values in given points and the colored boxes represent the volume in the opposite corner by which the corresponding values are multiplied. The black dot represents the interpolated value which is multiplied by the entire volume [51].

using a vector

$$t_\alpha \stackrel{\text{def}}{=} \begin{pmatrix} t_\alpha^0 \\ t_\alpha^1 \end{pmatrix} = \begin{pmatrix} 1 - \alpha_d \\ \alpha_d \end{pmatrix}, \quad (2.20)$$

where $\alpha \in \{x, y, z\}$ is an index. This gives a nice geometric interpretation to the trilinear interpolation as shown in Fig. 2.16. From this form and the figure, it is apparent that the final interpolated value does not depend on the order of axes along which we perform linear interpolations (see Fig. 2.15). Furthermore, we can write $\hat{f}(\mathbf{C})$ as a polynomial:

$$\hat{f}(\mathbf{C}) = \sum_{\alpha, \beta, \gamma \in \{0, 1\}} \sum_{i=0}^{\alpha} \sum_{j=0}^{\beta} \sum_{k=0}^{\gamma} (-1)^{(\alpha-i) + (\beta-j) + (\gamma-k)} f(\mathbf{C}_{ijk}) x_d^\alpha y_d^\beta z_d^\gamma. \quad (2.21)$$

We take advantage of this form when generalizing trilinear interpolation to irregular grid in Sec. 4.2.3.

3. Track Simulation

In order to develop and test the reconstruction algorithm, electron and positron tracks are simulated inside the first detector sector \mathcal{D}_1 (see Sec. 2.4.2) with different initial parameters (origin, initial direction and kinetic energy). Two approaches are currently used to simulate tracks, each of them for different purpose.

The **Microscopic Simulation** uses the Garfield++ toolkit [52]. Within this toolkit:

- a) Magboltz [39] is used to calculate the transport properties,
- b) the High Energy Electro-Dynamics (HEED) program [53] is used to simulate the primary particle,
- c) the class `AvalancheMicroscopic` to simulate the drift of secondary electrons created by ionization in the gas.

This is the most precise and time-consuming simulation used; our current goal is to be able to successfully reconstruct its results and determine our best-case energy resolution.

The **Runge-Kutta Simulation** uses the 4th order Runge-Kutta numerical integration to simulate the trajectory of the primary particle in the electromagnetic field inside the detector. It is relatively fast since it does not simulate the secondary particles. It is used as part of our reconstruction algorithm and for testing some parts of the reconstruction.

All of these simulations require the knowledge of the electromagnetic field (both **E** and **B**) inside the detector. A uniform electric field of $400 \text{ V}\cdot\text{cm}^{-1}$ is assumed. The magnetic field was simulated in Ansys Maxwell [49] (see Sec. 2.4.3).

3.1 Microscopic Simulation

The microscopic simulation, the most detailed simulation used in this work, is performed using the Garfield++ toolkit [52].

The electron transport properties are simulated using the program Magboltz. Two different gas mixtures were compared – 90:10 and 70:30 Ar:CO₂. The second mixture will be used in our detector. The temperature is set to 20 °C, the pressure is atmospheric.

The primary track is simulated using the program HEED, which is an implementation of the photo-absorption ionization model [53]. This program provides the parameters of ionizing collisions. HEED can also be used to simulate the transport of delta electrons; we do not account for them in the current simulation. The photons created in the atomic relaxation cascade are also not simulated (possibly causing fluorescence reabsorption, related to the spread of avalanches in Geiger-Muller detectors).

Finally, we use the microscopic tracking provided by the class `AvalancheMicroscopic` in Garfield++ to simulate the drift of the ionization electrons. Each electron is followed from collision to collision using the equation of motion and the collision rates calculated by Magboltz.

Garfield++ also contains two other classes for simulation of the drift. `AvalancheMC` uses Monte Carlo integration that requires generation of a gas file to approximate the transport parameters (we briefly considered this method, but decided that the

relatively small speed wasn't worth the loss of precision in this case, especially since the gas file generation for different angles between the field vectors is also computationally expensive). `DriftlineRKF` uses Runge-Kutta-Fehlberg integration of a phenomenological relation $\mathbf{v}_d = \mathbf{v}_d(\mathbf{E}, \mathbf{B})$, and therefore cannot account for diffusion.

3.1.1 First testing track

The first electron track simulated for testing purposes was chosen to have a special set of parameters:

- the starting point of the track is the origin of the coordinate system,
- the initial direction is along the positive x -axis,
- the momentum is $8 \text{ MeV}/c_0$ (the kinetic energy is 7.505 MeV).

Such a track moves in the XZ plane in the toroidal magnetic field of the detector, because the particle's velocity vector is always perpendicular to the field. At first, we simulated such a track in 90:10 Ar:CO₂ gas mixture, later we added a simulation in 70:30 Ar:CO₂, which we plan to use in our detector. The comparison of both simulations is in Fig. 3.1. In the first tests, the initial energy of produced ionization was set to 0.1 eV instead of the value generated by HEED.

3.1.2 Grid-like testing sample

In order to test all steps of the reconstruction, a sample of tracks with a grid-like distribution of parameters was generated on MetaCentrum. Five sets of 9702 tracks were generated with every combination of these parameters:

- electron and positron tracks,
- 11 different kinetic energies $E_{\text{kin}} \in [3 \text{ MeV}, 13 \text{ MeV}]$,
- 21 different azimuth angles $\varphi \in [-16.3^\circ, 16.3^\circ]$ and
- 21 different elevation angles $\theta \in [-17.1^\circ, 17.1^\circ]$.

A visualization of a set of e^+/e^- tracks with the same kinetic energy is shown in Fig. 3.2. In the 70:30 Ar:CO₂ atmosphere, each track takes 5-30 CPU hours to simulate. Every tenth point on the drift line was stored, the whole sample has 3.1 terabytes (or 1.4 gigabytes without drift lines).

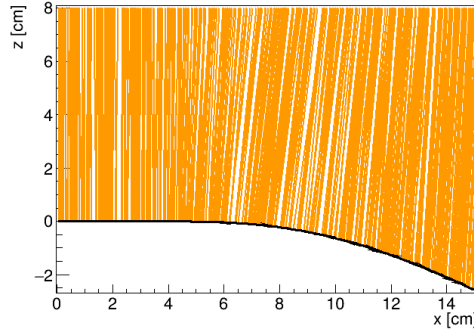
3.2 Runge-Kutta Simulation

The Runge-Kutta simulation in this work uses the Runge-Kutta 4th order (RK4) method to numerically integrate the equation of motion of a relativistic charged particle in an electromagnetic field. Given a system of first order differential equations

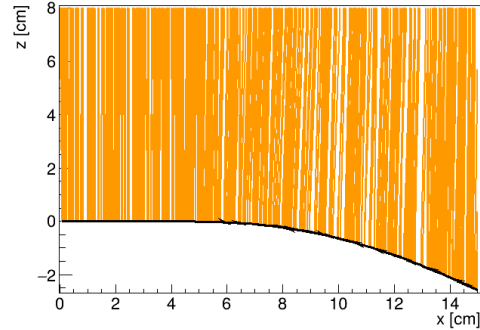
$$\frac{dy}{dt} = \mathbf{f}(t, \mathbf{y}(t)) \quad (3.1)$$

with an initial condition

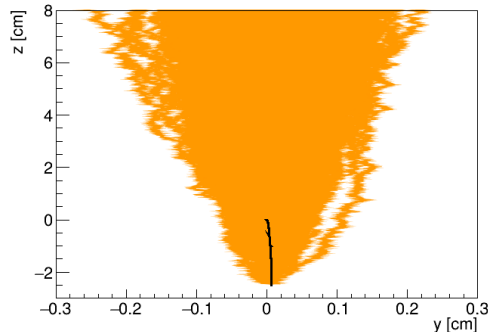
$$\mathbf{y}(t_0) = \mathbf{y}_0, \quad (3.2)$$



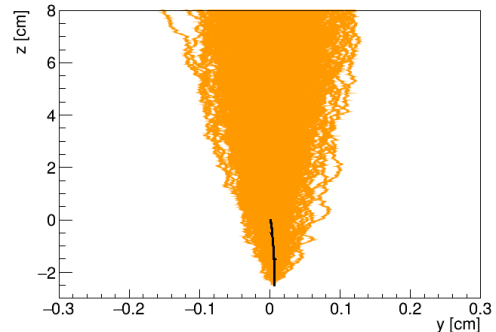
(a) 90:10 Ar:CO₂ drift lines XZ projection



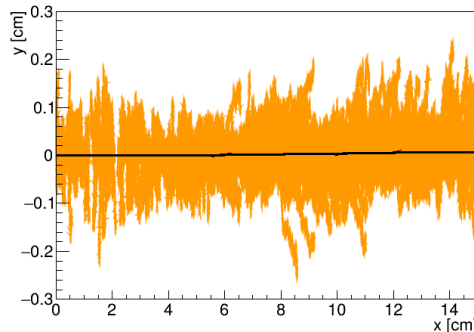
(b) 70:30 Ar:CO₂ drift lines XZ projection



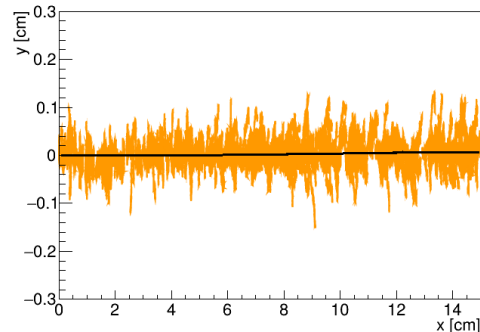
(c) 90:10 Ar:CO₂ drift lines YZ projection



(d) 70:30 Ar:CO₂ drift lines YZ projection



(e) 90:10 Ar:CO₂ drift lines XY projection



(f) 70:30 Ar:CO₂ drift lines XY projection

Figure 3.1 Comparison of drift lines for two different gas mixtures 90:10 and 70:30 Ar:CO₂. The electron track is marked in black, the drift lines of the ionization electrons are marked in orange. In this example, we assume a larger OFTPC volume with readout at 8 cm. Small curvature of the track in the YZ projection is caused by the tilt of the magnetic field in the bottom half of the Orthogonal Fields TPC (OFTPC).

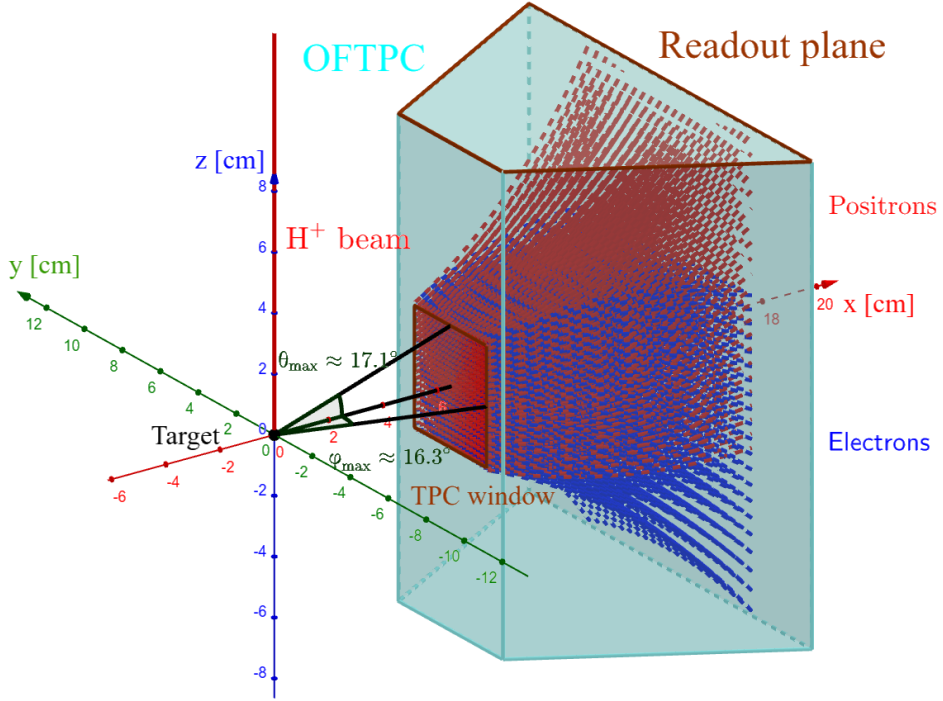


Figure 3.2 A visualization of a set of tracks from the grid-like testing sample with the same kinetic energy. Made with GeoGebra®.

we iteratively compute the estimate $\mathbf{y}_n = \mathbf{y}(t_n) = \mathbf{y}(t_0 + nh)$ as follows:

$$\mathbf{k}_1 = \mathbf{f}(t_n, \mathbf{y}_n), \quad (3.3)$$

$$\mathbf{k}_2 = \mathbf{f}\left(t_n + \frac{h}{2}, \mathbf{y}_n + \frac{h\mathbf{k}_1}{2}\right), \quad (3.4)$$

$$\mathbf{k}_3 = \mathbf{f}\left(t_n + \frac{h}{2}, \mathbf{y}_n + \frac{h\mathbf{k}_2}{2}\right), \quad (3.5)$$

$$\mathbf{k}_4 = \mathbf{f}(t_n + h, \mathbf{y}_n + h\mathbf{k}_3), \quad (3.6)$$

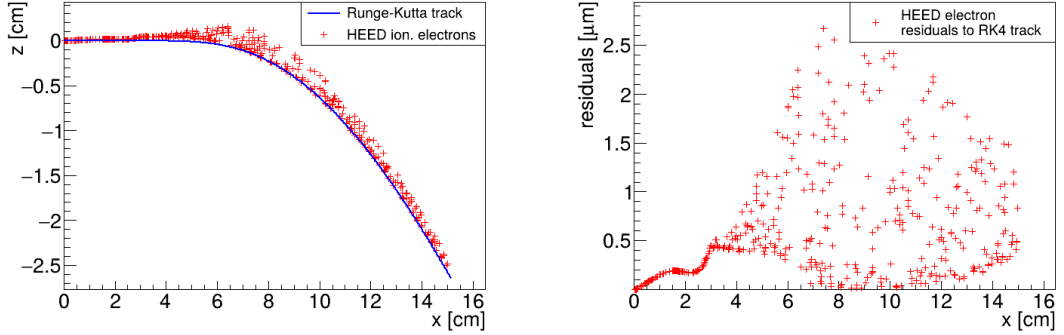
$$\mathbf{y}_{n+1} = \mathbf{y}_n + \frac{1}{6}(\mathbf{k}_1 + 2\mathbf{k}_2 + 2\mathbf{k}_3 + \mathbf{k}_4). \quad (3.7)$$

Infinitely many alternate forms of this equation are possible, with some of them being beneficial for certain special cases (trying to reach the same accuracy with lower computational cost). In our relatively simple case, where the integrated field changes slowly, the standard form with fixed step size is appropriate.

We want to integrate the equation of motion, given by the relativistic Lorentz force:

$$F_L^\mu = m \frac{du^\mu}{d\tau} = q F^{\mu\nu} u_\nu, \quad (3.8)$$

where the Einstein summation convention is used, m is the mass of the particle, q is its charge, u^μ is its four-velocity, τ is the proper time (i.e., time in the particle's frame of reference) and $F^{\mu\nu}$ is the electromagnetic tensor at given coordinates x^μ (we consider it to be time-independent in our detector). Given the electric $\mathbf{E} = (E_x, E_y, E_z)$ and the magnetic field $\mathbf{B} = (B_x, B_y, B_z)$ and using the metric



When exaggerating, the HEED ionization electrons are moved away along the shortest line connecting them to the RK4 track. The computation of this distance is described in Sec. 5.3.

signature $(+, -, -, -)$, the equation expands to

$$\frac{d}{d\tau} \begin{pmatrix} \gamma c \\ \gamma v_x \\ \gamma v_y \\ \gamma v_z \end{pmatrix} = \frac{q}{m} \begin{pmatrix} 0 & -\frac{E_x}{c} & -\frac{E_y}{c} & -\frac{E_z}{c} \\ \frac{E_x}{c} & 0 & -B_z & B_y \\ \frac{E_y}{c} & B_z & 0 & -B_x \\ \frac{E_z}{c} & -B_y & B_x & 0 \end{pmatrix} \begin{pmatrix} \gamma c \\ \gamma v_x \\ \gamma v_y \\ \gamma v_z \end{pmatrix}, \quad (3.9)$$

where c is the speed of light in vacuum, $\mathbf{v} = (v_x, v_y, v_z)$ is the particle's velocity and $\gamma = \left(1 - \frac{v^2}{c^2}\right)^{-\frac{1}{2}}$ is the Lorentz factor. Together with the equation

$$\frac{d}{d\tau} \begin{pmatrix} ct \\ x \\ y \\ z \end{pmatrix} = \begin{pmatrix} \gamma c \\ \gamma v_x \\ \gamma v_y \\ \gamma v_z \end{pmatrix} = u^\mu, \quad (3.10)$$

we get a system of eight first order differential equations for x^μ and u^μ , which we can integrate using the Runge-Kutta method described above. As a result of this integration, we get the position $\mathbf{x}(\tau_n)$, the velocity $\mathbf{v}(\tau_n)$ and the detector time $t(\tau_n)$ for every proper time $\tau_n = n\tau_{\text{step}}$. As initial conditions, we use the origin of the track (x_0, y_0, z_0) , the initial velocity direction vector $\mathbf{n} = (\cos \varphi \cos \theta, \sin \varphi \cos \theta, \sin \theta)$ and the kinetic energy E_{kin} , we then compute γ and $\|\mathbf{v}\|$:

$$\gamma = 1 + \frac{E_{\text{kin}}}{E_0}, \quad (3.11)$$

$$\|\mathbf{v}\| = c\sqrt{1 - \gamma^{-2}}. \quad (3.12)$$

An example Runge-Kutta track is compared with the corresponding microscopic track in Fig. 3.3. Example of tracks with same initial position and direction, but different energies is shown in Fig. 3.4.

3.2.1 Testing sample

In order to test the simulation and reconstruction, a sample of 1 000 000 tracks with randomized parameters (using TRandom3 from ROOT) was generated:

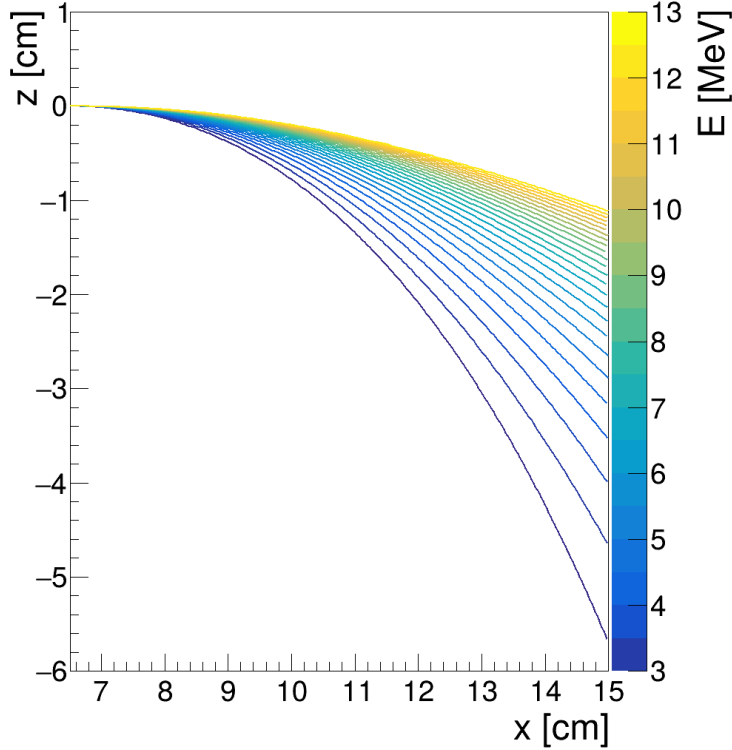


Figure 3.4 Set of 25 Runge-Kutta tracks with initial position $(6.51, 0, 0)$ cm, orientation $(1, 0, 0)$, and energies $3 - 13$ MeV.

- the Runge-Kutta step was set to 1.67 ps (coordinate time, each proper time step is adjusted by the gamma factor once at the beginning; for an 8 MeV track, $\tau_{\text{step}} = 0.1$ ps),
- the kinetic energy of the particle $E_{\text{kin}} = 3 - 13$ MeV,
- the starting point of the track is a random point in the OFTPC window,
- the initial direction is given by the line connecting a random point on the target¹ (a disc with 1 mm radius in the YZ plane).

Since the Runge-Kutta simulation is quite fast², it can be run locally on any computer.

¹To generate a random point on the target, we generate a random angle α and a random square of the distance from origin r^2 to get a uniform distribution.

²One track with $t_{\text{step}} = 1.67$ ps takes less than one millisecond to simulate.

4. Track Reconstruction

As the first step of the reconstruction algorithm, we reconstruct the track of a primary particle – either an electron or a positron. Then, using this information, we determine the energy of the particle (Chapter 5).

The **Reconstruction Assuming Steady Drift (RASD)** uses the standard TPC approach. With parallel fields, the drift inside a uniform electric field remains undistorted (as shown in Eq. 2.1). Therefore, we only need to reconstruct the z -coordinate from the drift time using the known drift velocity. We also assume that the readout coordinates (x', y', t) are known exactly, neglecting the pads and time binning.

Reconstruction using an **Ionization Electron Map** (from now on referred to as *the map*) uses a simulation of the drift of secondary (ionization) electrons within the detector volume. This simulation can then be used to interpolate the initial position of the secondary electrons. In the first iteration of this method the readout is assumed to be continuous.

We present two algorithms using the map for reconstruction. The first one uses a gradient descent algorithm along with trilinear interpolation (see Sec. 2.4.3) of the map. The second method uses interpolation on the irregular inverse grid with a polynomial.

The **Discrete Reconstruction** uses the map; instead of reconstructing the exact position of each electron, we reconstruct the center of each hit pad together with the time corresponding to the midpoint of the time bin. The electron count in each OFTPC bin (consisting of the pad and the time bin) serves as an idealized collected charge, which is then used as a weight in the energy reconstruction fit.

4.1 Reconstruction Assuming Steady Drift

As the first step, we tried to reconstruct a simulated electron track with a special set of initial parameters, described in detail in Sec. 3.1.1. The starting point is given by the origin of our coordinate system and its initial direction is given by the positive x -axis. This means the magnetic field of our detector is perpendicular to the momentum of the particle at all times, and we can reduce the problem to two-dimensional space.

For the reconstruction, we decided to use the common method used in a standard TPC[27]. We call this method *Reconstruction Assuming Steady Drift (RASD)*. This will allow us to explore the significance of the atypical behavior in our OFTPC. Additionally, we assume the readout is continuous to further simplify the problem. In this approximation, we reconstruct the initial position of each ionization electron.

The reconstruction is then defined by the following relations between the coordinates of the detector space and the readout space (see Sec. 2.4.2):

$$x = x', \quad (4.1)$$

$$y = y', \quad (4.2)$$

$$z = 8\text{ cm} - d_r = 8\text{ cm} - v_d t, \quad (4.3)$$

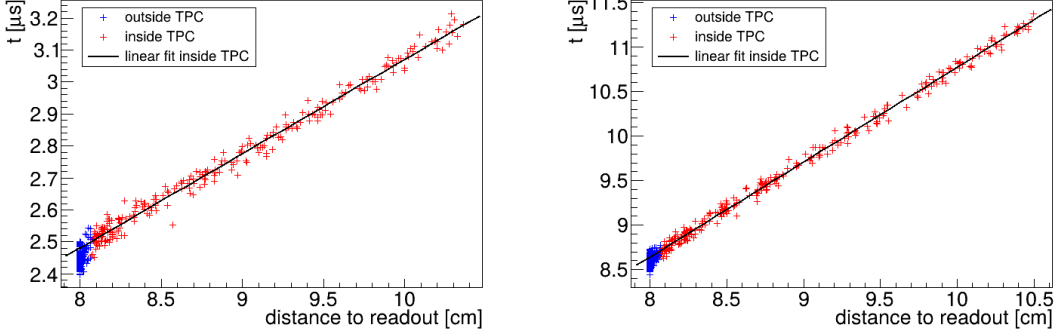


Figure 4.1 Linear fit of the drift time t dependence on the distance to the readout $d_r = 8 \text{ cm} - z$ for the ionization electrons in 90:10 (left) and 70:30 (right) Ar:CO₂ gas composition. Only electrons inside the OFTPC (red) are fitted. The parameters are $v_d = 3.39 \text{ cm}/\mu\text{s}$, $d_0 = -0.41 \text{ cm}$ for 90:10, and $v_d = 0.939 \text{ cm}/\mu\text{s}$, $d_0 = -0.11 \text{ cm}$ for 70:30 Ar:CO₂.

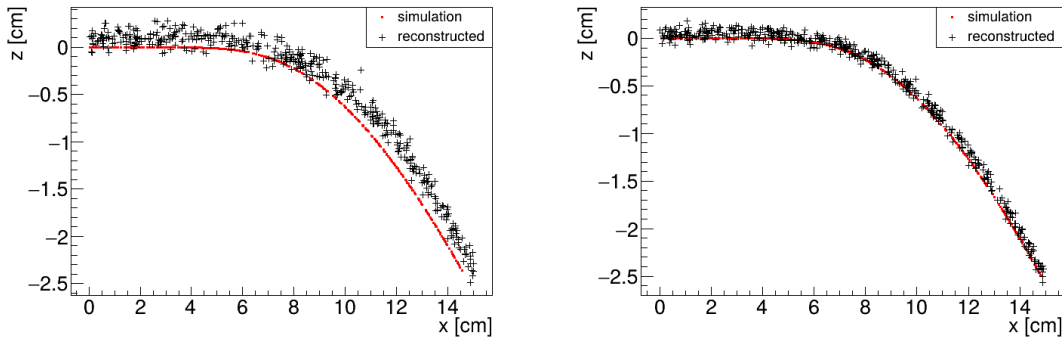


Figure 4.2 Reconstruction (black) of the starting position of ionization electrons (red) using parameters obtained from the fit (Fig. 4.1). Two gas compositions 90:10 (left) and 70:30 Ar:CO₂ (right) are compared.

where d_r is the distance to the readout, and v_d is the drift velocity of electrons in the given gas mixture. At a phenomenological level, this velocity can be considered as a function of the electric field \mathbf{E} and the magnetic field \mathbf{B} as shown in Eq. 2.1. Since we assume a uniform electric field in the detector and in this approximation we want to neglect the effect of our unusual magnetic field, we consider the drift velocity constant. We can estimate the drift velocity by fitting the dependence $d_r(t)$ of ionization electrons from a simulated track with a linear function:

$$d_r(t) = v_d t + d_0. \quad (4.4)$$

The fit was applied on two tracks with different gas composition, the result is in Fig. 4.1. The obtained parameters are then used for the reconstruction shown in Fig. 4.2. From the residuals shown in Fig. 4.3, we can see that this reconstruction algorithm leads to significant deviations from the simulated track (up to 1.1 cm for 90:10, and up to 0.3 cm for 70:30 Ar:CO₂), especially in the faster gas mixture 90:10 (as expected – for a higher mean time between collisions in Eq. 2.1, the effect of the magnetic field is bigger). These deviations are mainly caused by the shift in the x -coordinate due to the tilt of the drift lines in magnetic field. In order to account for this, we need to develop a better algorithm.

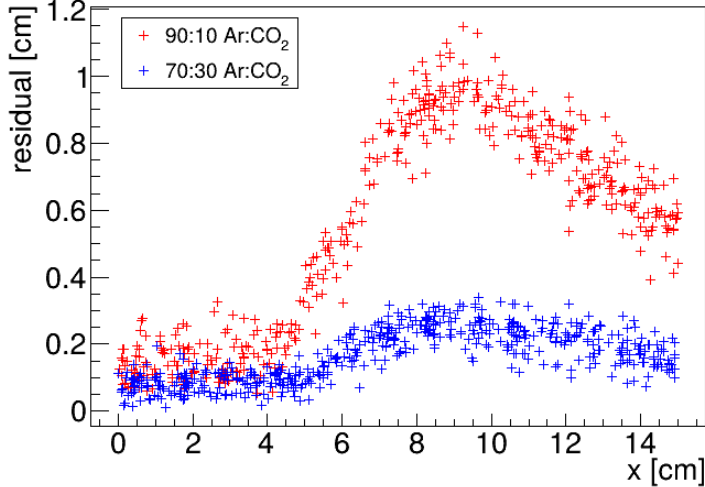


Figure 4.3 Comparison of residuals (i.e., the distance from the reconstructed point to the simulated ionization electron starting point) dependence on x for two gas mixtures 90:10 (red) and 70:30 Ar:CO₂ (blue).

4.2 Ionization Electron Map

Inside an OFTPC, the drift of the ionization electrons is significantly affected by its magnetic field as shown in Eq. 2.1, see also Fig. 3.1. We need to take this into account for accurate reconstruction. In the first approximation, we assume a continuous readout (i.e., we neglect the anode segmentation into pads). We can then reconstruct the original position of each ionization electron using its readout coordinates. For this purpose, we use the ionization electron map.

The ionization electron map represents a mapping from the detector space to the readout space (see Sec. 2.4.2). It tells us what readout coordinates (x', y', t) we can expect on average for an ionization electron created at the detector coordinates (x, y, z) . More precisely, it is a mapping to the distributions on the readout space; we can simplify this as only the means $\bar{\mathcal{M}}$ and the covariance matrices \mathcal{M}_Σ , assuming Gaussian distribution¹:

$$\bar{\mathcal{M}}: \mathcal{D} \longrightarrow \mathcal{R}, \quad (x, y, z) \longmapsto \bar{\mathbf{X}}^T \equiv (\bar{x}', \bar{y}', \bar{t}), \quad (4.5)$$

$$\mathcal{M}_\Sigma: \mathcal{D} \longrightarrow \mathbb{R}^{3 \times 3}, \quad (x, y, z) \longmapsto \Sigma \equiv \begin{pmatrix} \sigma_{x'}^2 & \text{cov}(x', y') & \text{cov}(x', t) \\ \text{cov}(y', x') & \sigma_y^2 & \text{cov}(y', t) \\ \text{cov}(t, x') & \text{cov}(t, y') & \sigma_t^2 \end{pmatrix}, \quad (4.6)$$

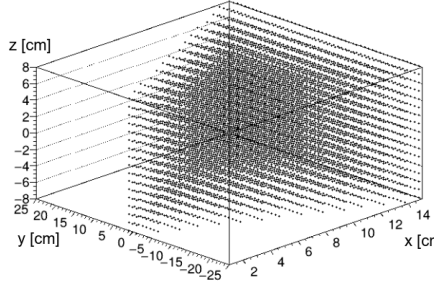
$$\mathcal{M}: \mathcal{D} \longrightarrow D(\mathcal{R}), \quad (x, y, z) \longmapsto N(\mathbf{X}) \equiv \frac{\exp\left(-\frac{1}{2}(\mathbf{X} - \bar{\mathbf{X}})^T \Sigma (\mathbf{X} - \bar{\mathbf{X}})\right)}{\sqrt{(2\pi)^3 |\Sigma|}}. \quad (4.7)$$

To get an approximation of this mapping, we simulate the drift of ionization electrons generated on a regular Cartesian grid $\mathbb{G} \subset \mathcal{D}$ with spacing l inside the volume of our OFTPC² (see the visualization in Fig. 4.4). In Fig. 4.5, you can see an example of drift lines from a test of the simulation. After testing runs, two

¹The applicability of Gaussian distribution was tested on simulated points of the map using the Mardia's test.

²The detector walls are not considered and we simulate the drift even outside of the OFTPC which allows us to interpolate even close to the walls.

Detector space \mathcal{D}



Readout space \mathcal{R}

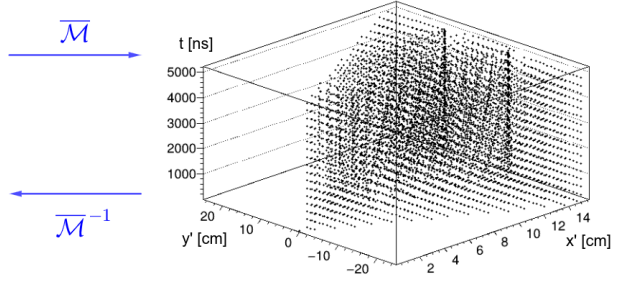


Figure 4.4 A 3D visualization of the mapping of means $\overline{\mathcal{M}}$ for the 90:10 Ar:CO₂ gas. A regular grid \mathbb{G} with $l = 1$ cm in the detector space is mapped to an irregular grid $\mathbb{G}^{-1} \equiv \overline{\mathcal{M}}(\mathbb{G})$ in the readout space. Made with GeoGebra®.

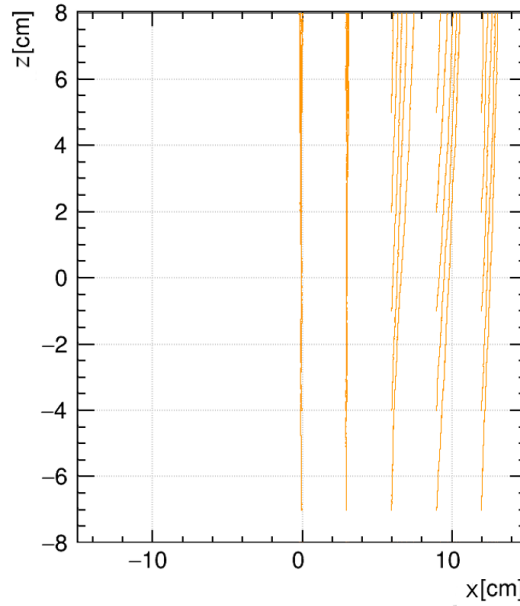


Figure 4.5 A test of the 90:10 Ar:CO₂ map simulation with spacing $l = 1.5$ cm. The resulting drift lines of evenly spaced electrons are displayed in orange.

map simulations were made with different gas composition, their parameters are shown in Tab. 4.1.

In order to get accurate results, we use the microscopic simulation of these electrons described in Sec. 3.1. It is also useful to simulate multiple (N) electrons originating from the same position so that we can account for the random fluctuations due to collisions. Using the readout coordinates of the electrons, we then estimate the means and the covariance matrix:

$$\bar{\mathbf{X}} = \frac{1}{N} \sum_{i=1}^N \mathbf{X}_i, \quad \Sigma = \frac{1}{N-1} \sum_{i=1}^N (\mathbf{X}_i - \bar{\mathbf{X}})(\mathbf{X}_i - \bar{\mathbf{X}})^T, \quad (4.8)$$

where \mathbf{X}_i represents the readout coordinates $(x'_i, y'_i, t_i)^T$ of the i -th electron. The matrix (resp. its submatrix) can then be used to plot error ellipsoid (resp. ellipse). The axes correspond to the eigenvectors, errors along these axes for a given

Parameter	90:10 Ar:CO ₂ map	70:30 Ar:CO ₂ map
N	100	100
l	1.0 cm	0.5 cm
z bounds	-8-8 cm	-8-8 cm
x bounds	0-15 cm	-1.5-15.0 cm
y bounds	$ y \leq x \cdot \tan \frac{\pi}{3}$	$ y \leq (x + 1.5 \text{ cm}) \cdot \tan \frac{\pi}{6}$
initial energy	0.1 eV	0.1 eV
init. direction	randomized	randomized

Table 4.1 Comparison of parameters of two map simulations.

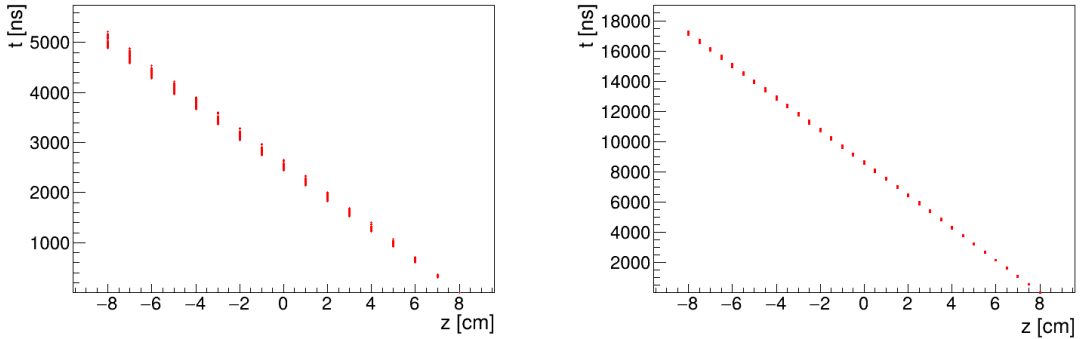


Figure 4.6 Dependence of the drift times of the simulated map $\bar{\mathcal{M}}$ on the z -coordinate. Two gas mixtures 90:10 (left) and 70:30 Ar:CO₂ (right) are compared. The spread is caused by varying Lorentz angles.

confidence level p can be computed using the chi-squared distribution

$$\sigma_i = \sqrt{\lambda_i \chi_k^2(p)}, \quad (4.9)$$

where λ_i is the corresponding eigenvalue and k is the number of degrees of freedom.

As shown in Figs. 4.6 and 4.7, the drift times in the map are no longer proportional to the z -coordinate due to the varying Lorentz angles in the inhomogeneous magnetic field (see Eq. 2.2). As expected, the effect is considerably larger in gases with higher drift velocities. Similarly, the drift distortion (i.e., its deviation from the vertical lines) is huge for the "faster" gas, but still significant for the "slower" one, as demonstrated in Figs. 4.8 to 4.10.

When evaluating the map inside the grid, we use trilinear interpolation (see Sec. 2.4.3). From now on, we will use the same symbol \mathcal{M} for this interpolated simulation.

Finally, we need to invert the map to get the original detector coordinates (x, y, z) from the given readout coordinates (x', y', t) . In our case, it is reasonable to assume that the mapping $\bar{\mathcal{M}}$ (we lose the information about the distribution, although it might be possible to recover through complex techniques; an idea, how to do this, is posed at the end of the thesis, though likely unpractical). We implemented two methods for this purpose: the gradient descent search (Sec. 4.2.2) and interpolation on the inverse grid (Sec. 4.2.3).

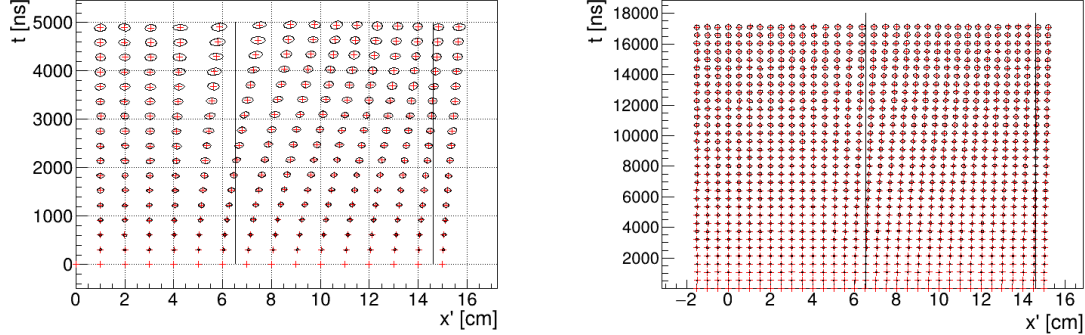


Figure 4.7 The $x't$ projection of the $\mathcal{M}(\mathbb{G}_{y=0})$ mapping of a part of the regular grid \mathbb{G} . The means $\overline{\mathcal{M}}(\mathbb{G}_{y=0})$ are marked with red crosses, and the diffusion error is denoted by black 95% confidence error ellipses computed from the diagonalized covariance matrices $\mathcal{M}_\Sigma(\mathbb{G}_{y=0})$. Two gas mixtures 90:10 (left) and 70:30 Ar:CO₂ (right) are compared. The first mixture shows differences of t for electrons with same initial z but different initial x . For the second mixture, these differences are negligible in comparison with the diffusion.

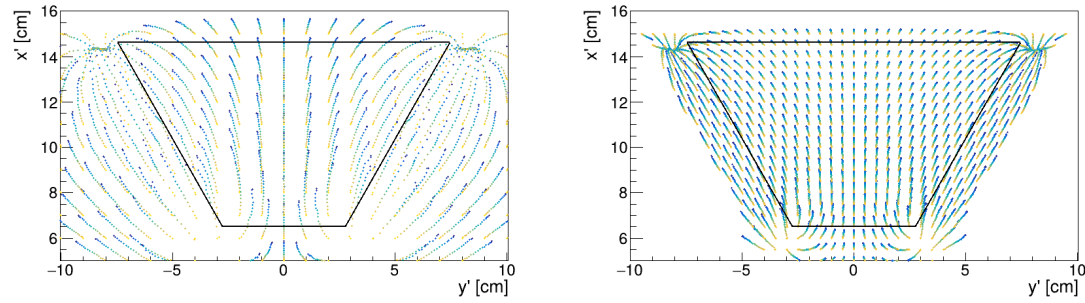
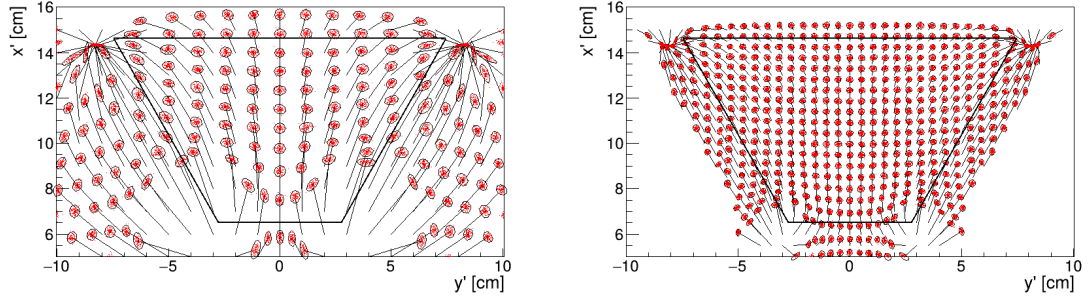
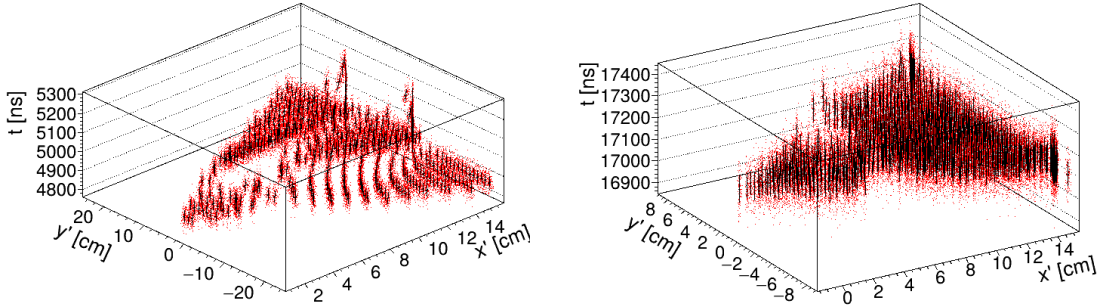


Figure 4.8 The regular grid \mathbb{G} projected by the mapping $\overline{\mathcal{M}}$ from the detector space onto the $x'y'$ plane (t is not plotted). Layers with lower z -coordinate (i.e., further away from the readout) are displayed with darker colors. The OFTPC volume is marked with black lines. Two gas mixtures 90:10 (left) and 70:30 Ar:CO₂ (right) are compared.



(a) The $x'y'$ projection of $\mathcal{M}(\mathbb{G}_{-8})$ (similar as in Fig. 4.8), the diffusion is denoted with the 95% error ellipses from the diagonalized sample covariance matrices $\mathcal{M}_\Sigma(\mathbb{G}_{-8}) \leftrightarrow$ Eq. 4.8, and computed using Eq. 4.9. The mean values $\bar{\mathcal{M}}(\mathbb{G}_{-8})$ are connected by black arrows with the corresponding starting position (x, y) of the simulated electrons. The OFTPC volume is marked with black lines.



(b) The full mapping $\mathcal{M}(\mathbb{G}_{-8})$, the diffusion is marked using standard error bars (black) from the diagonalized sample covariance matrices (Eqs. 4.8 and 4.9).

Figure 4.9 The $\mathcal{M}(\mathbb{G}_{-8})$ mapping of the bottom ($z = -8$ cm) layer \mathbb{G}_{-8} of the regular grid $\mathbb{G} \subset \mathcal{D}$. It includes both the mapping of means $\bar{\mathcal{M}}$ and of covariances \mathcal{M}_Σ . Individual electrons from the map simulation are marked with red dots. Two gas mixtures 90:10 (left) and 70:30 Ar:CO₂ (right) are compared.

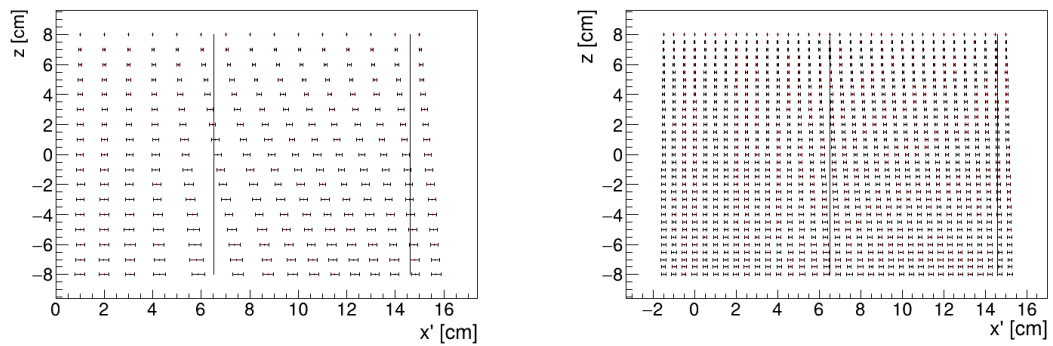


Figure 4.10 The readout coordinate x' for points on the grid $\mathbb{G}_{y=0}$ plotted against their initial coordinate z . The means are marked with red crosses, the diffusion in x' is denoted by standard error bars. Two gas mixtures 90:10 (left) and 70:30 Ar:CO₂ (right) are compared.

4.2.1 Map Simulation

Simulation of the map is a computationally heavy task. For this reason, we use the MetaCentrum grid [54] to parallelize needed calculations. At first, this was done by evenly distributing the simulated electrons across the individual jobs in a simulation with only one electron per vertex in the regular grid \mathbb{G} with a spacing of one centimeter. Later, a more efficient approach was implemented, accounting for the varying lengths of the drift of individual electrons. If we index the vertices of \mathbb{G} in the order of increasing coordinates y, x, z , we can express the number n_l of full XY layers (i.e., electrons with the same z coordinate, the mapping of one such layer is shown in Fig. 4.9b) with index less than or equal to i

$$n_l(i) = \left\lfloor \frac{i}{n_{xy}} \right\rfloor, \quad (4.10)$$

where n_{xy} is the number of electrons in each XY layer calculated simply by counting the electrons that satisfy boundary conditions for x and y . The number of electrons remaining in the top layer is then

$$n_r(i) = i \bmod n_{xy}. \quad (4.11)$$

Finally, we can calculate the sum of the drift gaps of electrons up to index i

$$d_{\text{sum}} = (z_{\max} - z_{\min})n_{xy}n_l - \frac{n_l(n_l - 1)}{2}n_{xy}l + n_r(z_{\max} - z_{\min} - n_ll). \quad (4.12)$$

We then use a binary search algorithm to find the maximum index i such that the value of this sum is less than the fraction $\frac{\text{job id}}{\max \text{ job id}}$ of the total sum. This way we obtain the minimal and the maximal index of electrons simulated in the given job. The obtained map is then stored in a custom class template `Field<MapPoint>` (used also for the magnetic field — `Field<Vector>`).

4.2.2 Gradient Descent Algorithm

The first implemented method of reconstruction uses a gradient descent algorithm to calculate an inversion of the map $\bar{\mathcal{M}}$ in a given point. Gradient descent is an iterative minimization algorithm for multivariate functions. Let $\mathbf{R} \in \mathcal{R}$ be a point in the readout space; we want to find a point $\mathbf{D} = (x, y, z) \in \mathcal{D}$ in the detector space such that

$$\bar{\mathcal{M}}(\mathbf{D}) = \mathbf{R} = (x'_{\mathbf{R}}, y'_{\mathbf{R}}, t_{\mathbf{R}}). \quad (4.13)$$

We define a function $f_{\mathbf{R}}$ in the readout space as a distance in this space:

$$f_{\mathbf{R}}(x', y', t) = \sqrt{(x' - x'_{\mathbf{R}})^2 + (y' - y'_{\mathbf{R}})^2 + v_d^2(t - t_{\mathbf{R}})^2}, \quad (4.14)$$

where v_d is an approximation of the drift velocity in the OFTPC, obtained from the reconstruction in Sec. 4.1 (see Fig. 4.2). We make an initial guess:

$$\mathbf{D}_0 = (x'_{\mathbf{R}}, y'_{\mathbf{R}}, v_d t). \quad (4.15)$$

Assuming we have the n -th estimate \mathbf{D}_n , we calculate the i -th component of the gradient of $f_{\mathbf{R}} \circ \overline{\mathcal{M}}$ numerically using central differences:

$$[\nabla(f_{\mathbf{R}} \circ \overline{\mathcal{M}})]^i(\mathbf{D}_n) \approx \frac{f_{\mathbf{R}}(\overline{\mathcal{M}}(\mathbf{D}_n + s \cdot e^i)) - f_{\mathbf{R}}(\overline{\mathcal{M}}(\mathbf{D}_n - s \cdot e^i))}{2s}, \quad (4.16)$$

where $e^i \in \mathcal{D}$ is the i -th coordinate vector and s is the step size. The step size should be sufficiently small; initially, we set it as a fraction $s = \frac{l}{10}$ of the map's grid spacing l . During the minimization, we check that $f_{\mathbf{R}}(\overline{\mathcal{M}}(\mathbf{D}_n)) < 10s$ at all times and decrease the step if needed. The next iteration can be calculated as follows:

$$\mathbf{D}_{n+1} = \mathbf{D}_n - \gamma \nabla(f_{\mathbf{R}} \circ \overline{\mathcal{M}})(\mathbf{D}_n), \quad (4.17)$$

where $\gamma \in \mathbb{R}^+$ is the damping coefficient. It should be set to a small enough value to ensure convergence, but large enough for sufficient converging speed. In order to avoid oscillation around the minimum, we also check that the size of the damped gradient does not exceed (or get too close to) the current value of the non-negative function:

$$10 \|\gamma \nabla(f_{\mathbf{R}} \circ \overline{\mathcal{M}})(\mathbf{D}_n)\| < f_{\mathbf{R}}(\mathbf{D}_n), \quad (4.18)$$

and lower γ otherwise. The minimization stops either when the error $f_{\mathbf{R}}(\overline{\mathcal{M}}(\mathbf{D}_n))$ drops below a specified value or when the number of iterations exceeds a certain limit (in this case, a message is printed into the console).

The parameters of this method can be further optimized (e.g., a better choice of γ and s , analytical computation of the gradient³); instead, we later decided to use the interpolation on the inverse grid described in the next section.

4.2.3 Interpolation on the Inverse Grid

The best current algorithm uses the interpolation on the inverse grid. Rather than inverting the trilinearly interpolated map using a numerical minimization method as in the previous section, we take advantage of the fact that the map $\overline{\mathcal{M}}$ is a bijection in the area of interest. Since we have simulated values of this map on a regular grid in the detector space \mathcal{D} , we also know the inverse map $\overline{\mathcal{M}}^{-1}$ on the irregular inverse grid in the readout space \mathcal{R} . To get an approximation of the inverse map in the entire readout space, we can use interpolation.

Since the inverse grid is irregular, trilinear interpolation cannot be applied. Given that the simulated map is dense enough to provide a good approximation considering the size of our pads, we can adopt a similar approach.⁴ As shown in Eq. 2.21 in Sec. 2.4.3, trilinear interpolation can be expressed as a polynomial:

$$\hat{f}(x, y, z) = axyz + bxy + cxz + dyz + ex + fy + gz + h, \quad (4.19)$$

where a, b, c, d, e, f, g, h are coefficients uniquely determined by the values of the function at the vertices of the interpolation cell. We can generalize this for

³The gradient can be computed analytically when using the trilinear interpolation, see Eq. 2.21.

⁴A more complicated and computationally heavy alternative would be natural neighbor interpolation or Kriging.

a function defined on an irregular grid. Given the function values at any eight points, we can write a system of eight linear equations

$$\begin{pmatrix} x_1y_1z_1 & x_1y_1 & x_1z_1 & y_1z_1 & x_1 & y_1 & z_1 & 1 \\ \vdots & \vdots \\ x_8y_8z_8 & x_8y_8 & x_8z_8 & y_8z_8 & x_8 & y_8 & z_8 & 1 \end{pmatrix} \begin{pmatrix} a \\ h \end{pmatrix} = \begin{pmatrix} f(x_1, y_1, z_1) \\ \vdots \\ f(x_8, y_8, z_8) \end{pmatrix}, \quad (4.20)$$

which has a unique solution for the coefficients for most values of (x_n, y_n, z_n) and $f(x_n, y_n, z_n)$, where $n \in \{1, \dots, 8\}$.

This approach introduces a small complication: finding the correct pseudocell (i.e., the image of eight vertices forming a cubic cell in the regular grid) in the inverse grid. The eight irregularly spaced vertices of this pseudocell do not define a unique volume, so there are multiple possible ways to partition \mathcal{R} into pseudocells, with no obvious choice among them. This problem could be solved by determining the exact volume boundary using the gradient descent search described above. However, since the difference between the interpolation polynomials is small near the boundary of the pseudocell, we choose one of them arbitrarily.

In the code, the map is stored in an array, and its individual points can be accessed using three indexes corresponding to the x , y , and z coordinates. Points outside of the area of the simulation are initialized with zeros. The search for the pseudocell finds the indices corresponding to the eight vertices. It starts by performing a binary search along the x -coordinate (comparing the x' -coordinate of the map vertices with that of the point, whose preimage we want to find) with indices corresponding to y and z fixed to half of their maximal value. After that, we fix the x and z indices and perform a binary search along y (making sure to exclude the zeros from initialization outside the simulation range beforehand), and finally, we fix the x and y indices and perform a search along z (inverted, since higher z corresponds to lower t). This procedure is then repeated until the pseudocell "contains" the preimage of the given point (meaning that for all readout coordinates x' , y' , t , there is a vertex of the pseudocell with a higher and a vertex with a lower value of that coordinate) or until 3 iterations are exceeded. We also attempt to fix the error by choosing a neighboring cell.

This approach should generally be faster than the gradient descent method, since we do not need to iterate. Currently, we are calculating the coefficients of the interpolation polynomial during the reconstruction of every point. If further optimization is needed in the future, we can precalculate them for the whole map.

4.3 Reconstruction testing

The continuous reconstruction using the map was tested on microscopic tracks with parameters described in Sec. 3.1.1. The difference between the reconstructed positions obtained using the two map inversion algorithms was found to be smaller than the uncertainty from diffusion by several orders of magnitude. In its unoptimized state, the gradient descent search was significantly slower (at least ten times) than the interpolation on the inverse grid.

An example of reconstruction of tracks in 90:10 and 70:30 Ar:CO₂ gas mixture is shown in Fig. 4.11. We can clearly see that the results have improved compare to the Reconstruction Assuming Steady Drift (RASD) (shown in Fig. 4.2).

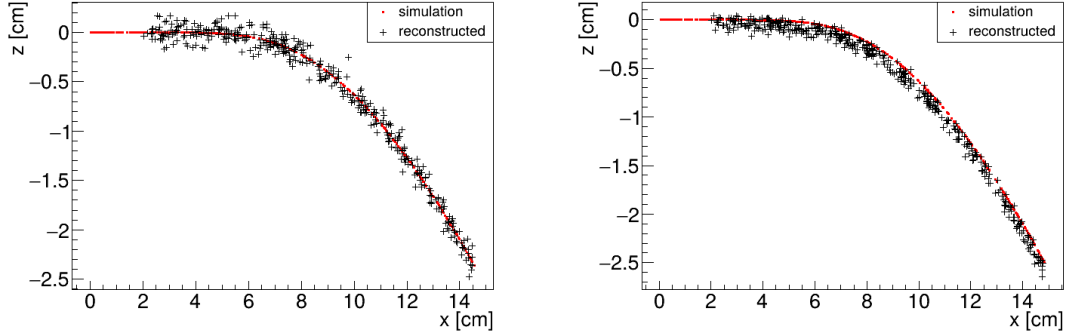


Figure 4.11 Reconstruction (black) of the starting position of ionization electrons (red) using the inversion of the ionization electron map. Two gas compositions 90:10 (left) and 70:30 Ar:CO₂ (right) are compared.

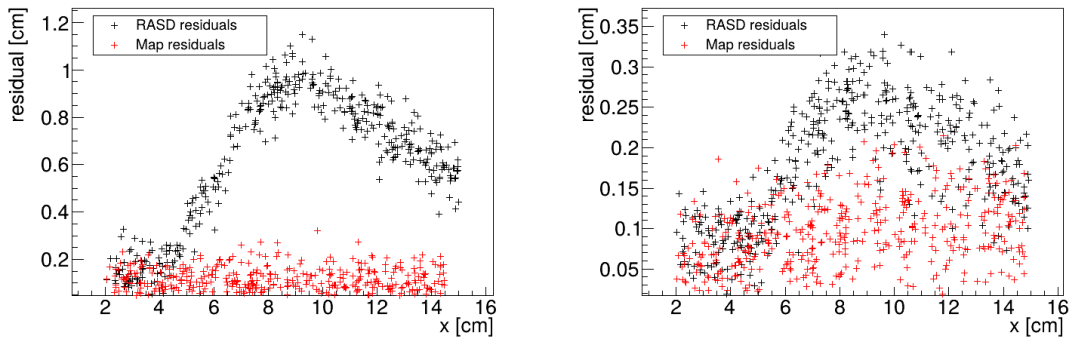


Figure 4.12 Comparison of residuals from the RASD (black) and map inversion (red) reconstruction methods. Tracks in two different gas compositions 90:10 (left) and 70:30 Ar:CO₂ (right) are compared (in the former gas mixture, the drift velocity is higher, therefore the distortion effects are more significant).

A comparison of the residuals of reconstructed positions (i.e., their distances to the real starting positions) is shown in Fig. 4.12. The histograms of residuals, as well as residuals of individual coordinates, are shown in Figs. 4.13 and 4.14. The bin width for the histograms was chosen using the Scott's rule⁵. As expected, the mean values of the coordinate residuals is zero. The only exception is the z -coordinate in the 70:30 Ar:CO₂ track, where the mean is -0.064 cm (further than one standard deviation 0.051 cm from zero). This is caused by the non-zero initial energy of the ionization electrons (neglected in the other track) which is unaccounted for in the map simulation. Since the primary electron bends towards negative z , the ionization electrons are more likely to be released in this direction (and also bend in the magnetic field towards this direction).

4.4 Discrete Reconstruction

In order to get a more realistic representation of a track measured in the OFTPC, we need to take the discretization of the position and time data into

⁵The optimal bin width for normally distributed data of size N with sample standard deviation $\hat{\sigma}$ is $\hat{\sigma} \sqrt[3]{\frac{24\sqrt{\pi}}{N}}$ [55].

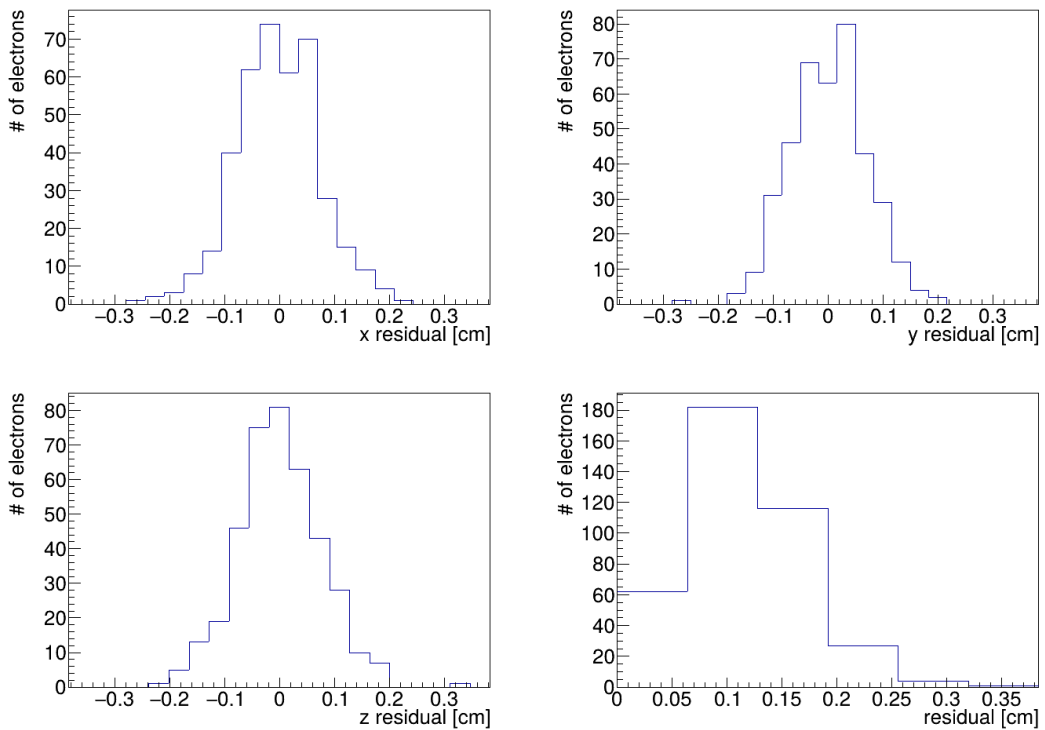


Figure 4.13 Map inversion reconstruction residuals (for the individual coordinates and total) of the testing track in 90:10 Ar:CO₂ gas mixture.

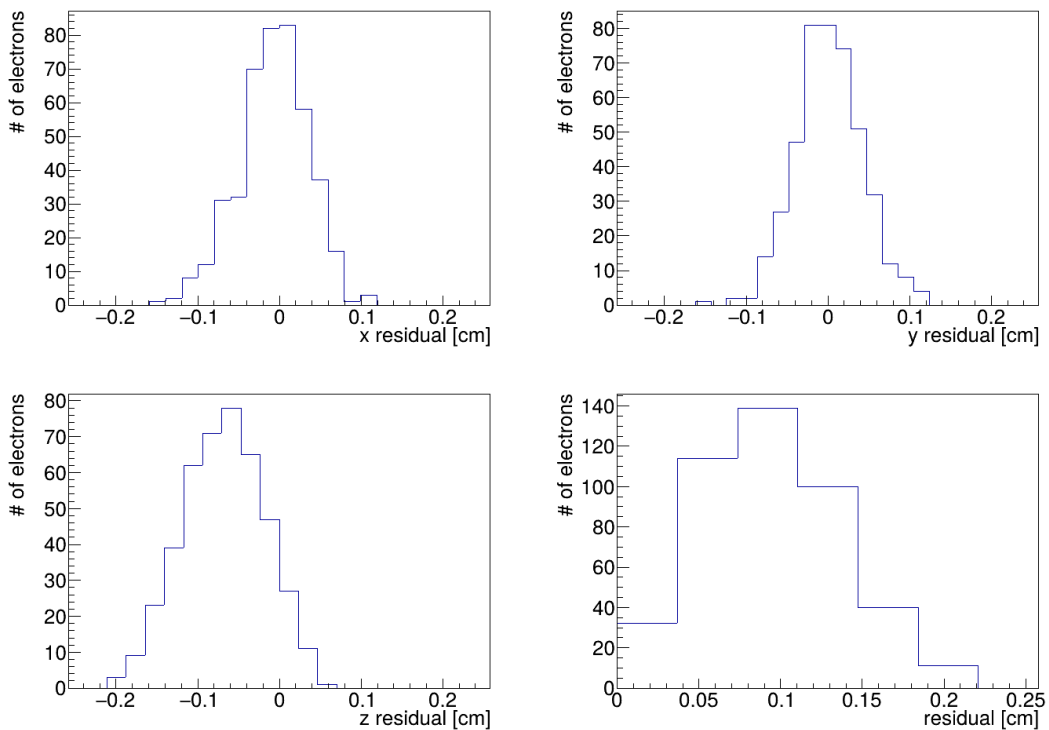


Figure 4.14 Map inversion reconstruction residuals (for the individual coordinates and total) of the testing track in 70:30 Ar:CO₂ gas mixture.

account. The readout of the OFTPC will consist of 128 pads, their layout is shown in Fig. 2.13. Time is read out in discrete bins of size $t_{\text{bin}} = 100 \text{ ns}$.

As the first approximation, we can neglect the multiplication in the triple-GEM and assume an ideal charge readout. The time measurement starts at the beginning of the electron/positron simulation. The readout coordinates $(x', y', t) \in \mathcal{R}$ of each ionization electron can be mapped to the pad coordinates $(n_{\text{pad}}, n_t) \in \mathcal{P}$:

$$n_{\text{pad}} = n : (x', y') \in \left[x_{1,n} - \frac{g}{2}, x_{2,n} + \frac{g}{2} \right] \times \left[y_{1,n} - \frac{g}{2}, y_{2,n} + \frac{g}{2} \right], \quad (4.21)$$

$$n_t = \left\lceil \frac{t}{t_{\text{bin}}} \right\rceil, \quad (4.22)$$

where $x, y_{1,n}$ and $x, y_{2,n}$ are the opposing pad corner coordinates, and g is the gap between the pads (described in detail in Sec. 2.4.2). This way, the closest pad is assigned to each readout position within the OFTPC volume⁶. The number of electrons collected by each pad (i.e., collected charge) in each time bin is then counted and serves as a weight for the energy reconstruction. The reconstructed track consists of points for each $(n, n_t) \in \mathcal{P}$, we get these by reconstructing the position of a hypothetical electron with the readout coordinates of the pad/time bin center:⁷

$$\mathcal{D} \ni (x, y, z) = \overline{\mathcal{M}} \left(x_{c,n}, y_{c,n}, \left(n_t - \frac{1}{2} \right) t_{\text{bin}} \right). \quad (4.23)$$

Examples of positions reconstructed for a single pad are shown in Fig. 4.15. For pads near the magnet poles, the interpolation becomes problematic, due to large distortion. We can use the slower, unoptimized gradient descent search instead, the results are shown in Fig. 4.16. An example of a track from the grid-like testing sample described in Sec. 3.1.2 is shown in Fig. 4.17

⁶Some positions near the wall are not handled and some pads extend beyond the OFTPC volume.

⁷Mapping the center of the pad (along with the midpoint of the time bin) is not necessarily the best approach since it might not correspond to the average parameters of an electron with these readout parameters.

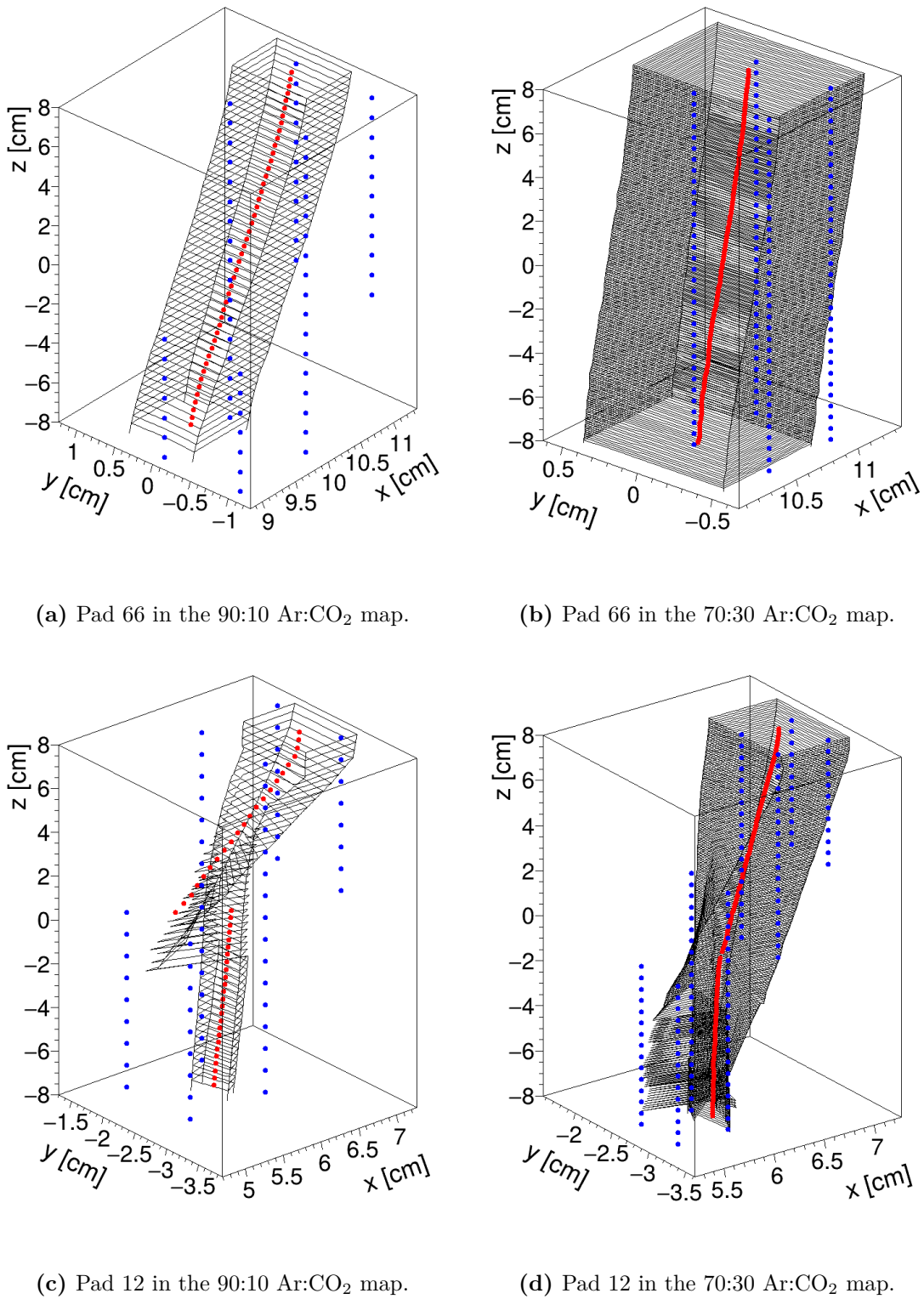


Figure 4.15 Reconstruction of detector coordinates for ionization electrons that are read out in a certain pad (number 66 near the center of the OFTPC, and number 12 near the magnet pole that suffers from large distortion effects, causing issues with interpolation on the inverse grid) and time bin. Boundaries of regions mapped to these discrete coordinates are shown in black, reconstructed center of the pad and time bin is shown in red, and map points used for the center reconstruction are shown in blue. Readout is placed at $z = -8$ cm.

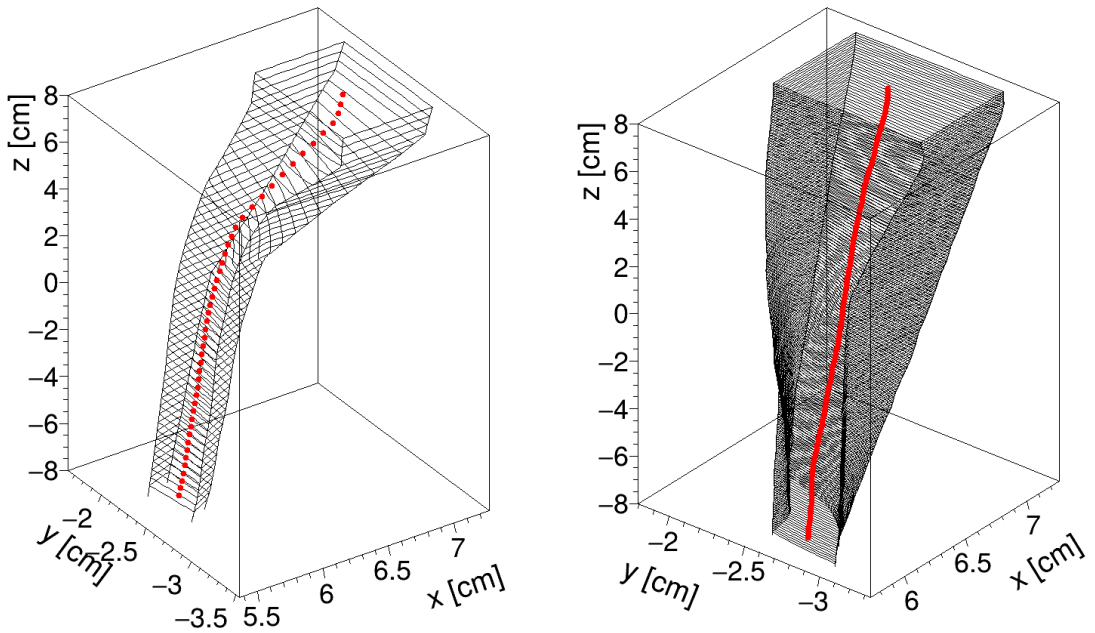


Figure 4.16 Reconstruction of detector coordinates corresponding to pad 12 (near the magnet pole) for different time bins. Unlike Fig. 4.15, we used the gradient descent search, which handles the large distortion better. In its current unoptimized state, these figures took 280 times longer to produce, compared to the interpolation on the inverse grid.

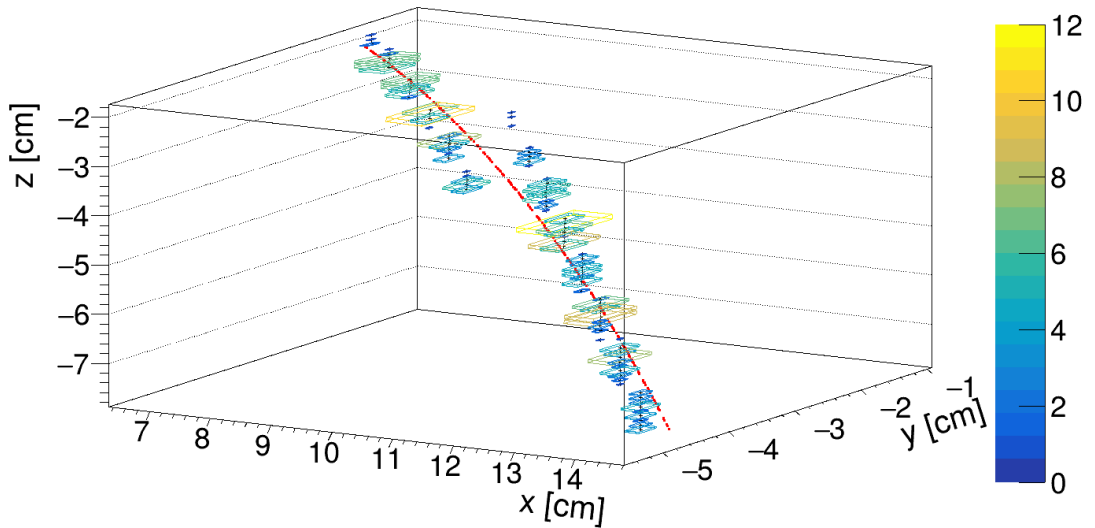


Figure 4.17 Discrete reconstruction of an 8 MeV track from the grid-like testing sample (described in Sec. 3.1.2) with minimal values of θ and ϕ initial direction angles. The simulated ionization vertices are shown in red, the reconstructed track is shown with the colored boxes. The number of electrons in each pad/time bin is denoted with the size of the boxes and their color. The apparent discontinuity is caused by the charge spreading between two pad "columns".

5. Energy Reconstruction

The second stage is the reconstruction of the particle’s energy using a fit of its reconstructed track (see Chapter 4). We have tested three ways of reconstructing the energy. Fitting is done using the MINUIT algorithm implemented in ROOT [56].

The **Cubic Spline Fit** was a tested and later rejected method of energy reconstruction. It uses smoothly connected piecewise cubic polynomials between uniformly spaced nodes. The reconstructed energy is calculated using the fit parameters by computing the radius of curvature in different points of the fitted curve using the known magnitude of the magnetic field perpendicular to the trajectory. We rejected this method because the tuning of the fit turned out to be unpractical compared to the other used methods.

The **Circle and Lines Fit** was chosen as an alternative since this corresponds to the shape of a trajectory of a charged particle crossing a finite volume with a homogeneous magnetic field. The energy of the particle can be estimated using the fitted radius and the magnitude of the perpendicular magnetic field in the middle of the OFTPC.

The **Runge-Kutta Fit** uses the 4th order Runge-Kutta numerical integration described in Sec. 3.2. Initial parameters of the track (including the particle’s energy) are optimized so that the integrated trajectory fits to the reconstructed one. This fit can also be performed as a single parameter (i.e., energy) fit if we get the initial position and orientation of the particle on the entrance to the OFTPC from previous detectors (TPX3 and MWPC, see Sec. 1.2).

5.1 Cubic Spline Fit

The first method for the estimation of the kinetic energy of the particle uses a cubic spline fit. We use an electron track simulated using the microscopic simulation, described in detail in Sec. 3.1.1. The track was reconstructed using the map described in Sec. 4.2.

In order to calculate the spline, we use the class `TSpline3` from ROOT. This allows us to evaluate the spline using the coordinates (x_n, z_n) of each node and the derivatives d_1, d_2 in the first and the last node. We can fit these parameters of a fixed amount of nodes to the simulated trajectory. We use the IMPROVE algorithm provided by the `TMinuit` class in ROOT. This algorithm attempts to find a better local minimum of the minimized function after converging.

After the fit converges, we calculate an energy estimate using the radius of curvature, which we can extract from the fitted spline equation at every point of the trajectory. The part of the spline corresponding to a given node is defined as

$$z(x) = z_n + b\Delta x + c(\Delta x)^2 + d(\Delta x)^3, \quad (5.1)$$

where $\Delta x = x - x_n$ and b, c, d are coefficients. Using this equation, we derive the

radius of curvature¹ as:

$$r(x) = \frac{(1 + z'^2(x))^{\frac{3}{2}}}{z''(x)} = \frac{(1 + (b + 2c\Delta x + 3d(\Delta x)^2)^2)^{\frac{3}{2}}}{2c + 6d\Delta x}. \quad (5.2)$$

Based on the geometry of our detector, we assume that the magnetic field satisfies $\mathbf{B}(x, 0, z) = (0, B(x, z), 0)$ for a track in the XZ plane. Since the electron is relativistic, the effect of the electric field on its trajectory is negligible. The Lorentz force \mathbf{F}_L is then always perpendicular to the momentum of the electron and acts as a centripetal force \mathbf{F}_c :

$$\begin{aligned} \mathbf{F}_L &= \mathbf{F}_c, \\ \|e\mathbf{v} \times \mathbf{B}\| &= \frac{\gamma m_e v^2}{r}, \\ ec\beta B &= \frac{E_{0e}\beta^2}{r\sqrt{1 - \beta^2}}, \end{aligned} \quad (5.3)$$

$$\begin{aligned} \sqrt{1 - \beta^2} &= \frac{E_{0e}\beta}{ecBr}, \\ \beta^2(x) &= \left[1 + \left(\frac{E_{0e}}{ecB(x, z(x))r(x)} \right)^2 \right]^{-1}, \end{aligned} \quad (5.4)$$

where e is the elementary charge, c is the speed of light in vacuum, m_e is the rest mass of electron, $E_{0e} = m_e c^2$ is its rest energy, γ is the Lorentz factor, \mathbf{v} is the velocity of the electron, and $\beta = \frac{v}{c}$. The kinetic energy for a given point on the trajectory is then given as

$$E_{\text{kin}}(x) = \left(\frac{1}{\sqrt{1 - \beta^2(x)}} - 1 \right) E_{0e}. \quad (5.5)$$

We could then average these estimates at multiple points (possibly using some weights to account for the change in accuracy) to get a single value. An example of the reconstruction for a reconstructed track is shown in Fig. 5.1. This method was later rejected in favor of the circle-and-lines fit described in the next section.

5.2 Circle and Lines Fit

Another way to estimate the particle's kinetic energy is to fit its trajectory with a circular arc with lines attached smoothly. This shape of trajectory corresponds to a movement of a charged particle through a homogeneous magnetic field perpendicular to the particle's momentum and limited to a certain volume. In general, the shape of such a trajectory with a non-perpendicularly oriented momentum is a spiral. In our case, the magnetic field is approximately toroidal and the particle motion is nearly perpendicular to it. At first, we tested a 2D version of this fit, then we adapted it to 3D.

¹For the general formula see https://en.wikipedia.org/wiki/Curvature#Graph_of_a_function.

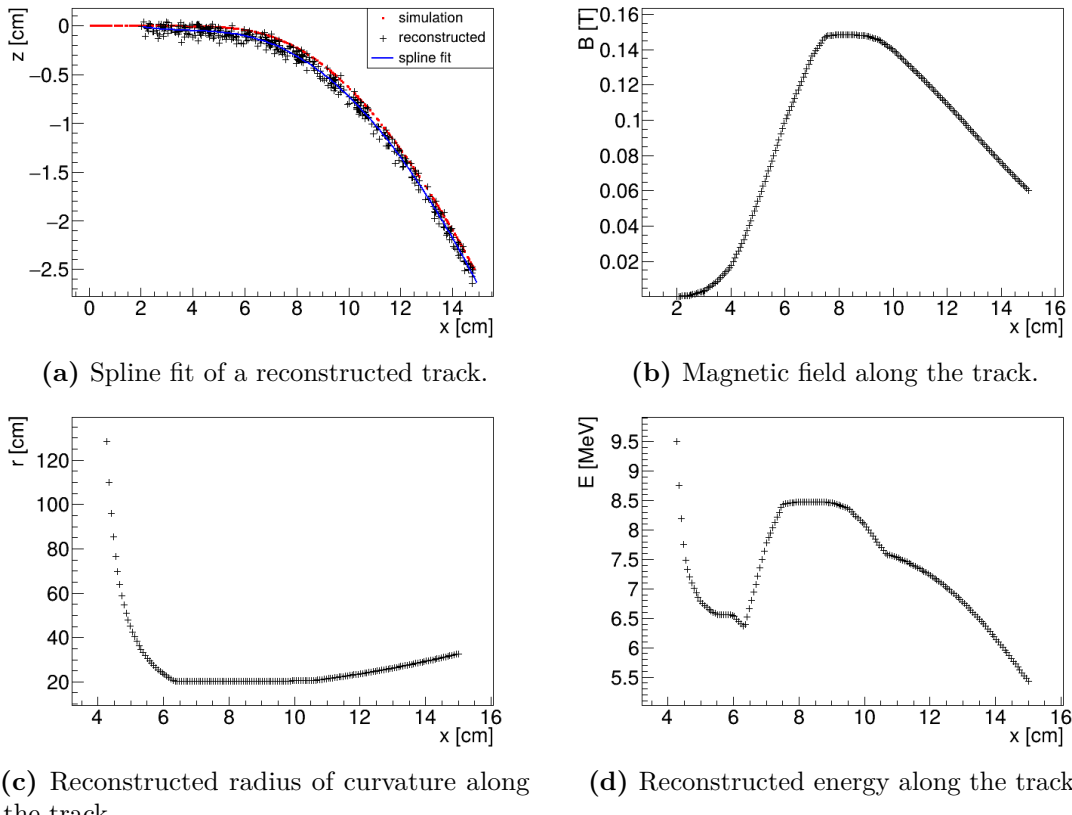


Figure 5.1 Energy reconstruction of a 7.51 MeV track in a 70:30 Ar:CO₂ gas mixture (described in detail in Sec. 3.1.1) using a cubic spline fit with four evenly spaced nodes of points reconstructed using the map.

The field in our detector is not homogeneous, it is therefore not entirely clear what value of magnetic field should be used along with the fitted radius (using Eqs. 5.4 and 5.5) to get the best estimate for the kinetic energy. Since we only use this method as the first iteration of the particle's energy that we later refine, an optimal solution of this problem is not required. Instead, we tested two options: taking the value of the field in the point, where the track crosses the middle x -coordinate of the OFTPC, and taking the average field along it.

5.2.1 Two-dimensional fit

In the 2D case, the fitted function used for the electron track² described in Sec. 3.1.1 is defined as follows:

$$z(x) = \begin{cases} a_1x + b_1 & x < x_1 \\ z_0 + \sqrt{r^2 - (x - x_0)^2} & x_1 \leq x \leq x_2 \\ a_2x + b_2 & x > x_2 \end{cases}, \quad (5.6)$$

where $a_{1,2}$ and $b_{1,2}$ are the parameters of the lines, (x_0, z_0) is the center of the circle, r is its radius, and $(x_{1,2}, z_{1,2})$ are the coordinates of the function's nodes. That means we have 9 parameters ($z_{1,2}$ are not used in the function) along with 2 continuity conditions and 2 smoothness conditions. For the fit, we use the coordinates of the nodes and the radius of the circle, which gives us 5 *independent* parameters (only the radius has to be larger than half of the distance between nodes). The continuity conditions (combined with the relations for $z_{1,2}$) are

$$z_{1,2} = a_{1,2}x_{1,2} + b_{1,2} = z_0 - \sqrt{r^2 - (x_{1,2} - x_0)^2}, \quad (5.7)$$

the smoothness conditions are

$$a_{1,2} = \frac{x_0 - x_{1,2}}{\sqrt{r^2 - (x_{1,2} - x_0)^2}}. \quad (5.8)$$

Together with Eq. 5.7 we get the values of $b_{1,2}$

$$b_{1,2} = z_{1,2} - a_{1,2}x_{1,2}. \quad (5.9)$$

For the coordinates of the center of the circle, we can use the fact that the center has to lie on the axis of its chord. In other words, there is a value of a parameter t such that, using the parametric equation of the axis

$$\begin{pmatrix} x_0 \\ z_0 \end{pmatrix} = \begin{pmatrix} \frac{x_1+x_2}{2} \\ \frac{z_1+z_2}{2} \end{pmatrix} + t \begin{pmatrix} \frac{z_2-z_1}{2} \\ \frac{x_1-x_2}{2} \end{pmatrix}. \quad (5.10)$$

At the same time, the center has to be in a distance of r from the nodes:

$$\begin{aligned} (x_1 - x_0)^2 + (z_1 - z_0)^2 &= r^2, \\ \left(\frac{x_1 - x_2}{2} + \frac{z_1 - z_2}{2}t \right)^2 + \left(\frac{z_1 - z_2}{2} + \frac{x_2 - x_1}{2}t \right)^2 &= r^2, \\ \left(\left(\frac{x_2 - x_1}{2} \right)^2 + \left(\frac{z_2 - z_1}{2} \right)^2 \right)t^2 + \left(\frac{x_2 - x_1}{2} \right)^2 + \left(\frac{z_2 - z_1}{2} \right)^2 - r^2 &= 0. \end{aligned} \quad (5.11)$$

²Electron tracks bend towards negative z , we need to use the upper part of the circle.

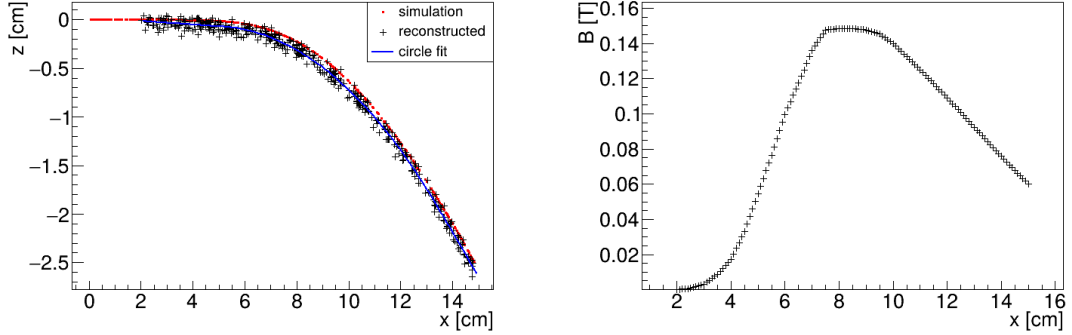


Figure 5.2 Circle-and-lines 2D energy reconstruction of a 7.51 MeV track in a 70:30 Ar:CO₂ gas mixture (described in detail in Sec. 3.1.1) reconstructed with the map. The fitted position of the nodes is $(x_1, z_1) = (5.20, -0.07)$ cm and $(x_2, z_2) = (14.43, -1.93)$ cm, the radius is $r = 20.79$ cm. The resulting energy is 7.70 MeV, the magnetic field along the track is shown on the right.

Since our electron track bends towards negative z and $x_2 > x_1$, we only care about the solution with $t > 0$

$$t = \sqrt{\frac{r^2}{\left(\frac{x_2-x_1}{2}\right)^2 + \left(\frac{z_2-z_1}{2}\right)^2} - 1}, \quad (5.12)$$

$$\begin{aligned} x_0 &= \frac{x_1+x_2}{2} + \frac{z_2-z_1}{2} \sqrt{\frac{r^2}{\left(\frac{x_2-x_1}{2}\right)^2 + \left(\frac{z_2-z_1}{2}\right)^2} - 1}, \\ z_0 &= \frac{z_1+z_2}{2} - \frac{x_2-x_1}{2} \sqrt{\frac{r^2}{\left(\frac{x_2-x_1}{2}\right)^2 + \left(\frac{z_2-z_1}{2}\right)^2} - 1}. \end{aligned} \quad (5.13)$$

The function defined in Eq. 5.6 along with Eqs. 5.8, 5.9 and 5.13 derived using the continuity and smoothness conditions (combined with the relations for $z_{1,2}$) fully define our fitted function with parameters $r, x_{1,2}, z_{1,2}$.

For the calculation of kinetic energy from the radius of the circle, we use the value of the magnetic field in the middle of the OFTPC. An example of a fit of vertices reconstructed with the map is shown in Fig. 5.2.

5.2.2 Three-dimensional fit

In three dimensions, the shape of a trajectory of a charged particle in a uniform magnetic field is a cylindrical helix. Nevertheless, since we assume that the field is approximately perpendicular to the particle's momentum at all times, we will further approximate the trajectory with a circular arc $\mathbf{X}_C(\phi)$ (with lines $\mathbf{X}_{L1}(t), \mathbf{X}_{L2}(s)$ attached smoothly).

We assume that the initial position $\mathbf{X}_0 = (x_0, y_0, z_0)$ and direction (given by the spherical angles θ, φ , see Sec. 2.4.2) are known, since this information will be provided by TPX3 and MWPC layers. The fit then has four free parameters (see Fig. 5.3):

- the length of the first line l (as measured from the initial position),
- the radius of the circular arc r ,

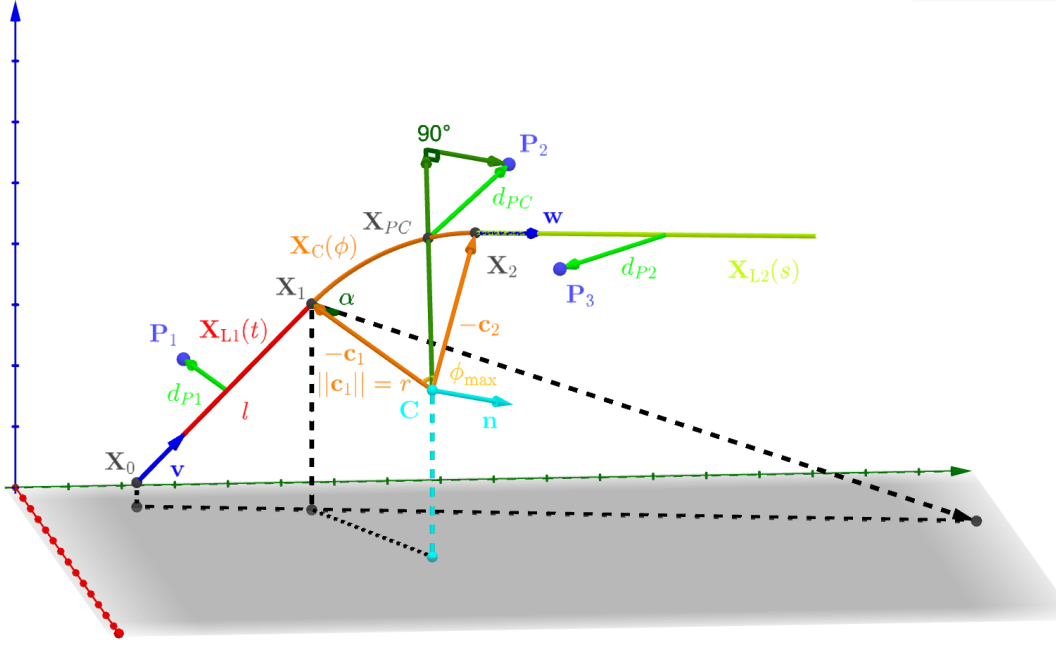


Figure 5.3 Visualization of the 3D geometry of the circle-and-lines fit and its parameters. Projection of some points on the XY plane is shown to better display the spatial arrangement. Made with GeoGebra®.

- the central angle of the arc $\phi_{\max} \in [0, 2\pi]$,
- the direction of the curvature given by the angle $\alpha \in [0, 2\pi]$ (right-handed with respect to the particle direction, $\alpha = 0$ if the particle curves towards negative z in a plane given by \hat{z} and the direction vector).

Using these parameters, we can derive a parametrization of the whole curve. Let \mathbf{v} be the initial unit direction vector, i.e., using the spherical angles

$$\mathbf{v} = (\cos \varphi \cos \theta, \sin \varphi \cos \theta, \sin \theta)^T, \quad (5.14)$$

then we can parameterize the first line as follows:

$$\mathbf{X}_{L1}(t) = \mathbf{X}_0 + t\mathbf{v} \quad t \in [0, l]. \quad (5.15)$$

This gives us the starting point of the arc

$$\mathbf{X}_1 = \mathbf{X}_{L1}(l) = \mathbf{X}_0 + l\mathbf{v}. \quad (5.16)$$

The vector \mathbf{c}_1 that lies in the plane of curvature and points from \mathbf{X}_1 to the center of curvature can be calculated using a composition of rotations. First, we rotate \mathbf{v} to point in the \hat{x} direction, the normal for $\alpha = 0$ than points in the $-\hat{z}$ direction, we apply the α rotation and reverse the rotations into the \hat{x} direction:

$$\begin{aligned}
 \mathbf{c}_1 &= R_z(\varphi)R_y(-\theta)R_x(\alpha)R_y\left(\frac{\pi}{2}\right)R_y(\theta)R_z(-\varphi)\mathbf{v}, \\
 &= R_z(\varphi)R_y(-\theta)R_x(\alpha)(-\hat{z}), \\
 &= \begin{pmatrix} \cos \varphi & -\sin \varphi & 0 \\ \sin \varphi & \cos \varphi & 0 \\ 0 & 0 & 1 \end{pmatrix} \begin{pmatrix} \cos \theta & 0 & -\sin \theta \\ 0 & 1 & 0 \\ \sin \theta & 0 & \cos \theta \end{pmatrix} \begin{pmatrix} 1 & 0 & 0 \\ 0 & \cos \alpha & -\sin \alpha \\ 0 & \sin \alpha & \cos \alpha \end{pmatrix} \begin{pmatrix} 0 \\ 0 \\ -1 \end{pmatrix}, \quad (5.17) \\
 &= \begin{pmatrix} -\sin \alpha \sin \varphi + \cos \alpha \cos \varphi \sin \theta \\ \sin \alpha \cos \varphi + \cos \alpha \sin \varphi \sin \theta \\ -\cos \alpha \cos \theta \end{pmatrix}.
 \end{aligned}$$

Similarly by rotating $\hat{\mathbf{y}}$, we can get the normal vector $\mathbf{n} = \mathbf{v} \times \mathbf{c}_1$ perpendicular to the plane of the trajectory:

$$\mathbf{n} = R_z(\varphi)R_y(-\theta)R_x(\alpha)\hat{\mathbf{y}} = \begin{pmatrix} -\cos \alpha \sin \varphi - \sin \alpha \cos \varphi \sin \theta \\ \cos \alpha \cos \varphi - \sin \alpha \sin \varphi \sin \theta \\ \sin \alpha \cos \theta \end{pmatrix}. \quad (5.18)$$

This allows us to express the coordinates of the center \mathbf{C} of the circular arc:

$$\mathbf{C} = \mathbf{X}_1 + r\mathbf{c}_1. \quad (5.19)$$

We can then get the parametrization and the endpoint of the circular arc using Rodrigues' rotation formula:

$$\begin{aligned} \mathbf{c}_2 &= \mathbf{c}_1 \cos \phi_{\max} + (\mathbf{n} \times \mathbf{c}_1) \sin \phi_{\max} + \mathbf{n}(\mathbf{n} \cdot \mathbf{c}_1)(1 - \cos \phi_{\max}), \\ &= \mathbf{c}_1 \cos \phi_{\max} - \mathbf{v} \sin \phi_{\max}, \end{aligned} \quad (5.20)$$

$$\mathbf{X}_C(\phi) = \mathbf{C} - r(\mathbf{c}_1 \cos \phi - \mathbf{v} \sin \phi) \quad \phi \in [0, \phi_{\max}], \quad (5.21)$$

$$\mathbf{X}_2 = \mathbf{X}_C(\phi_{\max}) = \mathbf{C} - r\mathbf{c}_2, \quad (5.22)$$

and if we define the direction vector of the second line, we also get its parametrization

$$\mathbf{w} = \mathbf{v} \cos \phi_{\max} + (\mathbf{n} \times \mathbf{v}) \sin \phi_{\max} = \mathbf{v} \cos \phi_{\max} + \mathbf{c}_1 \sin \phi_{\max}, \quad (5.23)$$

$$\mathbf{X}_{L2}(s) = \mathbf{X}_2 + s\mathbf{w} \quad s \in [0, \infty). \quad (5.24)$$

The fit is performed as a (weighted) least square minimization using the MIGRAD algorithm provided by the **TVirtualFitter** class in ROOT. We need to derive the distance of any point \mathbf{P} to the fitted curve. For the first line, we simply compute the parameter value of the closest point on the line:

$$\begin{aligned} t_{\mathbf{P}} &= \mathbf{v} \cdot (\mathbf{P} - \mathbf{X}_1), \\ d_{\mathbf{P}1} &= \|\mathbf{P} - \mathbf{X}_{L1}(t_{\mathbf{P}})\|. \end{aligned} \quad (5.25)$$

If the parameter value is outside of its bounds defined above, we take the boundary value instead. The distance to the second line is computed likewise. For the circular arc, we find the closest point by projecting the center connecting line onto the arc plane:

$$\mathbf{X}_{PC} = \mathbf{C} + r \frac{(\mathbf{P} - \mathbf{C}) - (\mathbf{n} \cdot (\mathbf{P} - \mathbf{C}))\mathbf{n}}{\|(\mathbf{P} - \mathbf{C}) - (\mathbf{n} \cdot (\mathbf{P} - \mathbf{C}))\mathbf{n}\|}, \quad (5.26)$$

$$d_{\mathbf{P}C} = \|\mathbf{P} - \mathbf{X}_{PC}\| \quad (5.27)$$

If the point \mathbf{X}_{PC} lies outside of the arc, distance to the closest endpoint is taken instead³. The shortest distance out of $d_{\mathbf{P}1}, d_{\mathbf{P}C}, d_{\mathbf{P}2}$ is then taken as the distance to the curve.

For the calculation of the kinetic energy from the radius, we implemented two variants:

³In some cases, the distance might be underestimated when the point is closer to the circle, the arc is a part of, than to the curve. We have attempted to fix this issue, but for an unknown reason, it led to problems with the fit convergence.

Parameter	Fit of microscopic track	Fit of reconstructed track
l	$-0.27(90)$ cm	$-0.26(62)$ cm
α	$-6.2(23)^\circ$	$-8.2(23)^\circ$
r	$17.2(48)$ cm	$16.8(28)$ cm
ϕ_{\max}	$26.1(72)^\circ$	$20.5(36)^\circ$
$E_{\text{reco}}^{\text{mid}}$	7.93 MeV	7.35 MeV
$E_{\text{reco}}^{\text{avg}}$	7.80 MeV	8.19 MeV

Table 5.1 3D circle fit parameters of an 8 MeV track from the grid-like testing sample (described in Sec. 3.1.2) with minimal values of θ and ϕ initial direction angles.

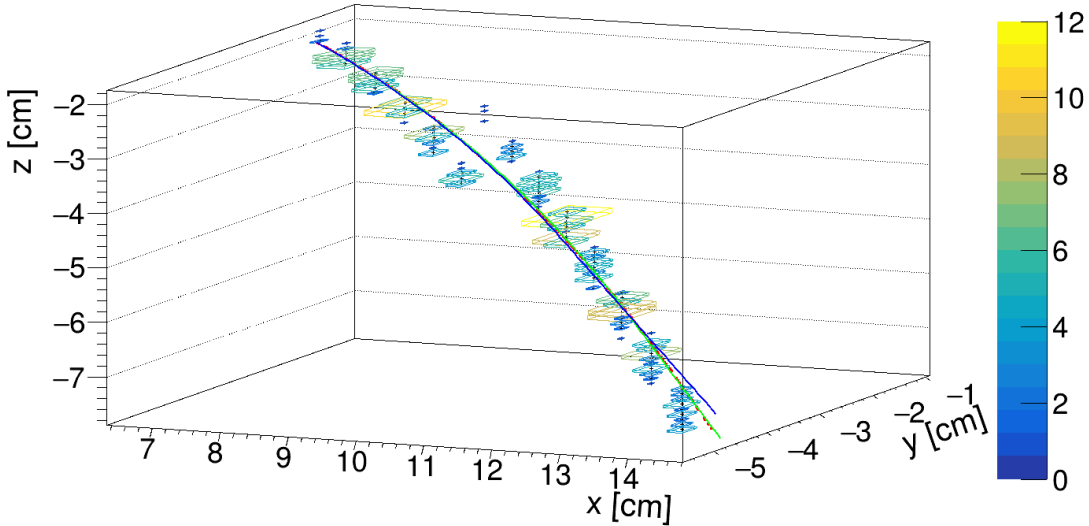
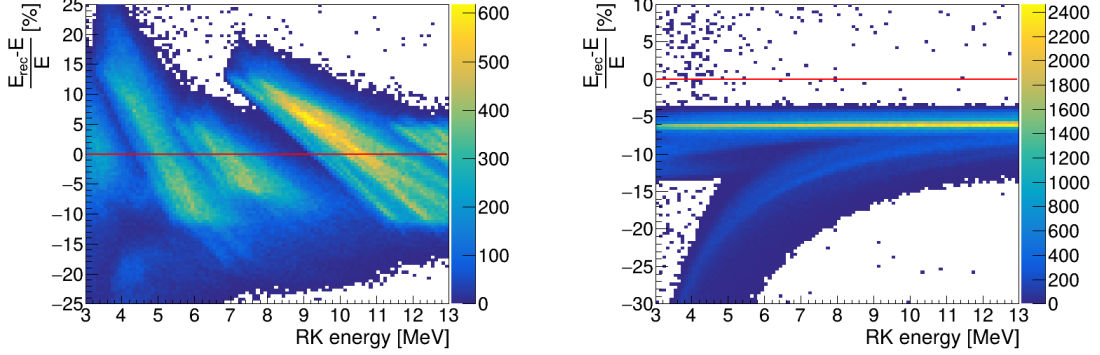


Figure 5.4 3D circle fit of an 8 MeV track (red points) from the grid-like testing sample (described in Sec. 3.1.2) with minimal values of θ and ϕ initial direction angles. Both fits of the original (green) and reconstructed track (blue) are shown. Resulting parameter values are given in Tab. 5.1.

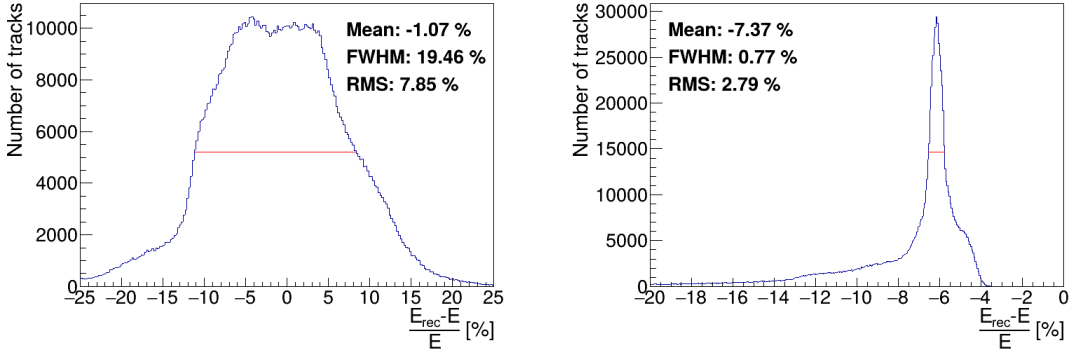
1. the "middle field" method, using the perpendicular projection to the plane of the trajectory of magnetic field at a point, where the circular arc crosses the central plane of the OFTPC (parallel to the YZ plane), and
2. the "average field" method using the average value of this projection along the circular arc.

This way, we get two energy estimates $E_{\text{reco}}^{\text{mid}}$ and $E_{\text{reco}}^{\text{avg}}$. If needed, this choice can be further optimized, however, since this method will only provide an initial guess of the kinetic energy for the more sophisticated, and computationally heavy Runge-Kutta fit, it is not necessary to reach the best precision, and fast solutions are preferred.

An example of a fitted track (both the actual initial points and the discrete reconstruction of the track) from the microscopic grid-like testing sample (described in Sec. 3.1.2) is shown in Fig. 5.4, the fitted parameters are given in Tab. 5.1.



(a) Dependence of relative error on simulated energy for both magnetic field selection methods.



(b) Overall relative error for both magnetic field selection methods. Freedman-Diaconis rule was used for bin width selection.

Figure 5.5 Relative error of the energy of Runge-Kutta tracks reconstructed with the 3D circle-and-lines fit. The middle (left) and the average field (right) methods are compared. Dependence on the initial direction angles θ and φ is small in comparison (for this reason, the plots are not shown).

5.2.3 Testing on a Runge-Kutta sample

The three dimensional circle-and-lines fit was tested on a sample of Runge-Kutta tracks with randomized parameters described in Sec. 3.2.1. These tracks of primary electrons and positrons consist of points calculated with the RK4 algorithm for a given time step. The parameter ranges in the MIGRAD minimizer have to be carefully tuned, simple exclusion of pathologic values can lead to convergence towards an edge value. After the tuning, only 4163 out of 1 000 000 tracks failed to converge to energy within 2 MeV from the simulation. We compared the two methods of choosing the magnetic fields. The resulting relative errors of reconstructed energy are shown in Fig. 5.5. When appropriate, we use the Freedman-Diaconis rule⁴ for bin width selection [57].

We see that the average field method systematically underestimates the particle's energy, but has ~ 25 times lower FWHM (only 0.77%) than the average field method. This shows that, when corrected, this method can serve as a good initial estimate of the particle's energy, before it gets refined by the Runge-Kutta fit.

⁴The Freedman-Diaconis rule is equivalent to the Scott's rule for normally distributed data, but it uses the interquartile range instead of the sample standard deviation, which makes it less sensitive to outliers.

5.3 Runge-Kutta Fit

The Runge-Kutta fit uses the Runge-Kutta 4th order (RK4) numerical integration of the equation of motion (see Sec. 3.2) to find the best values of the track parameters – the track origin, initial velocity direction and the kinetic energy. In order to speed up the energy reconstruction, an initial guess of these parameters can be obtained from the 3D circle fit described in the previous section. Furthermore, assuming we know the track origin and orientation, we can perform a single parameter fit of the kinetic energy.

The fit is performed as a least square minimization of the (weighted) distances of the track points (true ionization vertices from the simulation or reconstructed points). The simulated RK4 track consists of line segments with known endpoints, therefore we can calculate the distance of a point from this segment analogically to Eq. 5.25 with \mathbf{v} given as a unit vector in the direction of the segment.

We need to find the segment with the lowest distance. We assume, that the distance $d_{\mathbf{P}}(\tau)$ of a point \mathbf{P} to the point on the track (a curve parameterized by the proper time τ) $\mathbf{X}(\tau)$ has a single minimum (local and global), no local maximum (except the interval endpoints) and no saddle point

$$\exists! \tau_{\min} \in [0, \tau_N]: (\forall \tau \in [0, \tau_N]: d_{\mathbf{P}}(\tau) \geq d_{\mathbf{P}}(\tau_{\min})) \vee \frac{dd_{\mathbf{P}}}{d\tau}(\tau_{\min}) = 0, \quad (5.28)$$

where N is the number of RK4 steps. This is a reasonable assumption for a track with an approximate shape of a circular arc with a radius r , since the distance d from a point \mathbf{C} on the corresponding circle of a point \mathbf{P} offset by a from the arc plane and by b from the arc's center when projected on its plane is given by the law of cosines:

$$d^2 = a^2 + b^2 + r^2 - 2br \cos \alpha, \quad (5.29)$$

where α is the angle between points \mathbf{C} and \mathbf{P} as seen from the center of the arc (see Fig. 5.6). This function is strictly convex for $\alpha \in (-\frac{\pi}{2}, \frac{\pi}{2})$ and in our case, the center of the arc lies outside of the detector and α is restricted to a small interval around zero (especially considering that the initial guess should make the fitted trajectory reasonably close to any relevant point, in the worst-case scenario, the distance is overestimated, which should keep the fit from converging to such solutions).

In a more general case, if we consider the vector $\mathbf{a}(\tau) = \mathbf{P} - \mathbf{X}(\tau)$ whose size is $\|\mathbf{a}(\tau)\| = d_{\mathbf{P}}(\tau)$, then we get

$$2d_{\mathbf{P}} \frac{dd_{\mathbf{P}}}{d\tau} = \frac{dd_{\mathbf{P}}^2}{d\tau} = 2\mathbf{a} \cdot \frac{d\mathbf{a}}{d\tau} = -2\mathbf{a} \cdot \frac{d\mathbf{X}}{d\tau}, \quad (5.30)$$

therefore for the derivative of $d_{\mathbf{P}}(\tau)$ to be zero, $\mathbf{a}(\tau)$ has to be perpendicular to the tangent of the track. In 3D, for a given $\mathbf{X}(\tau)$, this condition restricts \mathbf{P} to a plane. This means that on a curving track, for any two points $\mathbf{X}(\tau_1), \mathbf{X}(\tau_2)$ with non-parallel tangents, we can find a point \mathbf{P} that has $\frac{dd_{\mathbf{P}}}{d\tau}(\tau_1) = \frac{dd_{\mathbf{P}}}{d\tau}(\tau_2) = 0$, which violates the assumption 5.28. If we have a circle-and-lines track as described in the previous sections, such a point has to lie outside of the circular sector given by the arc.

For a planar track $\mathbf{X}(\tau) = (X_1(\tau), X_2(\tau))$, the envelope of all its normals is the evolute of the curve (i.e., the set of centers of all its osculating circles). If the

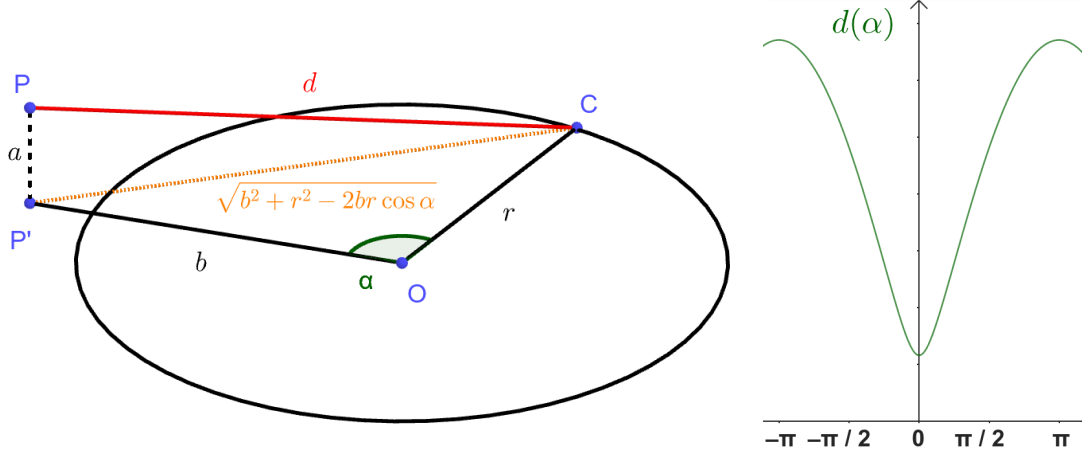


Figure 5.6 Demonstration of the convexity of the distance function $d(\alpha)$ for a circular track (see Eq. 5.29). Made with GeoGebra®.

track has a monotonous tangent angle

$$\alpha(\tau) = \text{atan} \frac{\frac{dX_2}{d\tau}}{\frac{dX_1}{d\tau}} \quad (5.31)$$

with minimal and maximal α differing by less than π (i.e., the track changes direction by less than 180°), then all intersections of the track's normals must lie in an area bordered by the evolute and the normals at the beginning and the end of the curve (from their intersection with the evolute to their mutual intersection, see Figs. 5.7 and 5.8). Together, these three boundaries define a closed shape that will lie outside of the OFTPC for a typical track in our detector⁵.

With the assumption 5.28, we can find the segment on the RK4 track with the lowest distance to a given point \mathbf{P} using a binary search algorithm. Let the distance of the point from the n -th vertex be $d_{\mathbf{P},n} = d_{\mathbf{P}}(\tau_n)$. Then the difference $\Delta d_{\mathbf{P},n} = d_{\mathbf{P},n} - d_{\mathbf{P},n-1}$ satisfies

$$\begin{aligned} \Delta d_{\mathbf{P},n} &< 0 \quad \forall n \text{ such that } \tau_n < \tau_{\min}, \\ \Delta d_{\mathbf{P},n} &> 0 \quad \forall n \text{ such that } \tau_{n-1} > \tau_{\min}. \end{aligned} \quad (5.32)$$

Therefore, we can search for the segment containing $d_{\mathbf{P},\min} = d_{\mathbf{P}}(\tau_{\min})$ with binary search starting with $\Delta d_{\mathbf{P},1}$ and $\Delta d_{\mathbf{P},N}$, then calculate the difference $\Delta d_{\mathbf{P},m}$ for the middle index $m = \left\lfloor \frac{N+1}{2} \right\rfloor$. If $\Delta d_{\mathbf{P},m} > 0$, we can replace the higher index with m , otherwise we replace the lower index. The search stops when the difference between the minimal and maximal index is one. The Fit itself is done using the MIGRAD algorithm implemented for the `TVirtualFitter` class in ROOT.

5.3.1 Testing on a microscopic sample

The Runge-Kutta fit together with the 3D circle-and-lines pre-fit was tested on a sample of tracks simulated using the microscopic simulation described in Sec. 3.1.

⁵The smallest anticipated radius of curvature is 39 cm for an electron or positron with a kinetic energy 3 MeV in a 0.3 T magnetic field. All points in the exclusion area must be farther from the track and therefore outside the OFTPC.

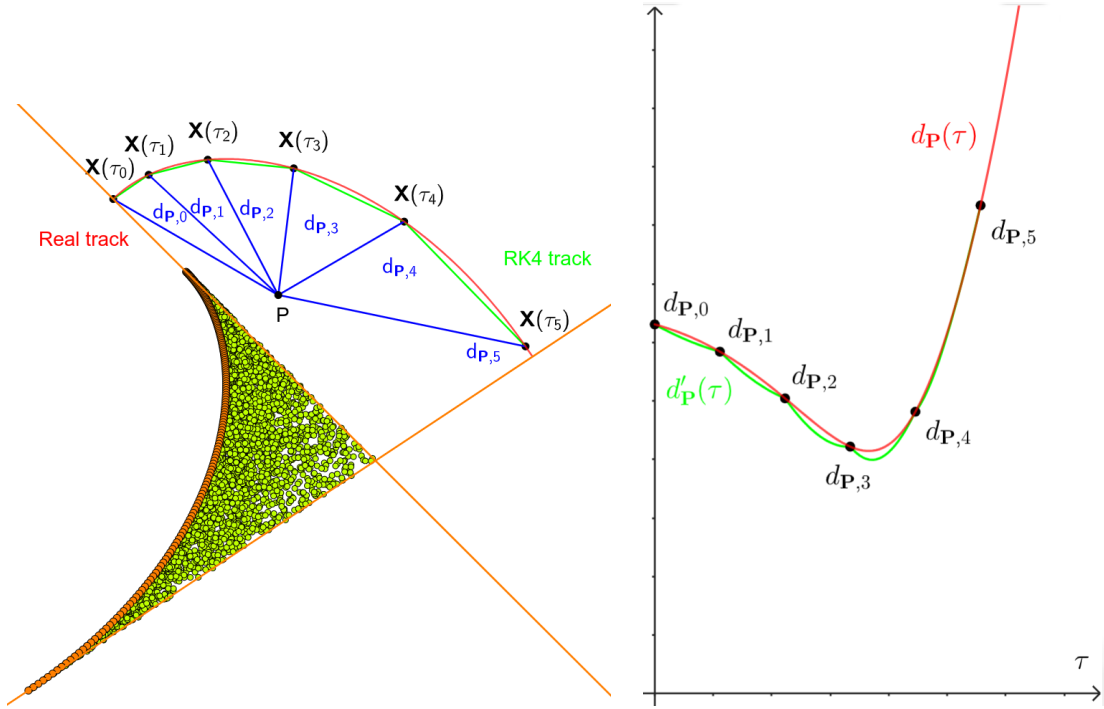


Figure 5.7 An example track (red) with a polygonal chain approximation (green, representing a RK4 simulation). The distance of the point \mathbf{P} from the chain is found using a binary search among the distances to the vertices $d_{\mathbf{P}}(\tau_i)$ (blue) and subsequently calculating the distance to segments neighboring the found vertex (thus finding the minimum of the function $d'_{\mathbf{P}}(\tau)$, function $d_{\mathbf{P}}(\tau)$ for the actual track is showed for reference). This approach works if the condition 5.28 is satisfied, which is not the case for a point from the green area bordered by the normals at endpoints and the evolute of the track (orange). Made with GeoGebra®.

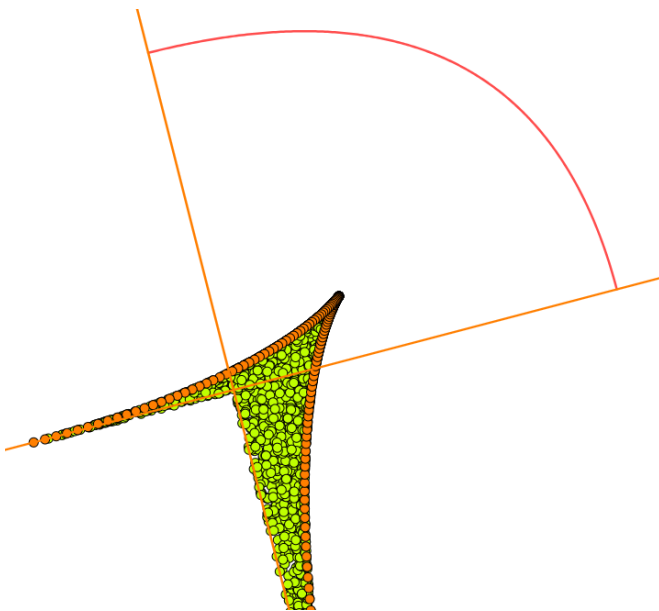


Figure 5.8 An exclusion area (green) of a track (red) bordered by its evolute and the normals at endpoints (orange), where the assumption 5.28 is violated. Unlike the track in Fig. 5.7, this track has a minimal curvature point in the middle, corresponding to the cusp on its evolute. Made with GeoGebra®.

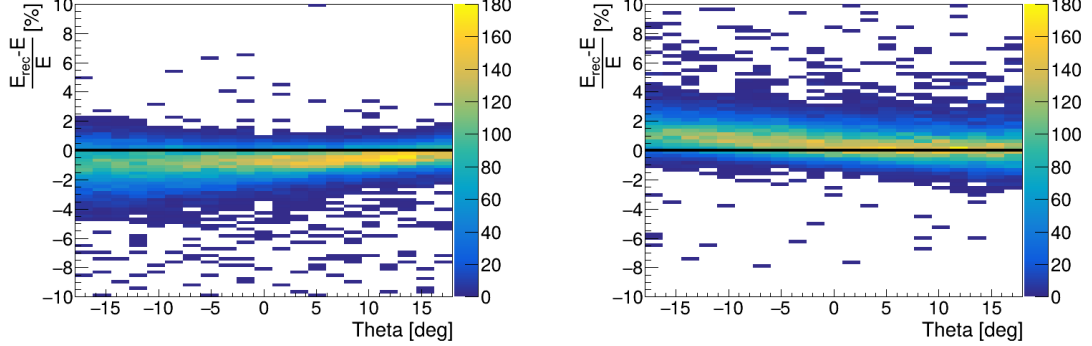


Figure 5.9 Dependence on theta of relative differences of reconstructed Runge-Kutta versus simulated energy for the Runge-Kutta fit for electrons (left) and positrons (right).

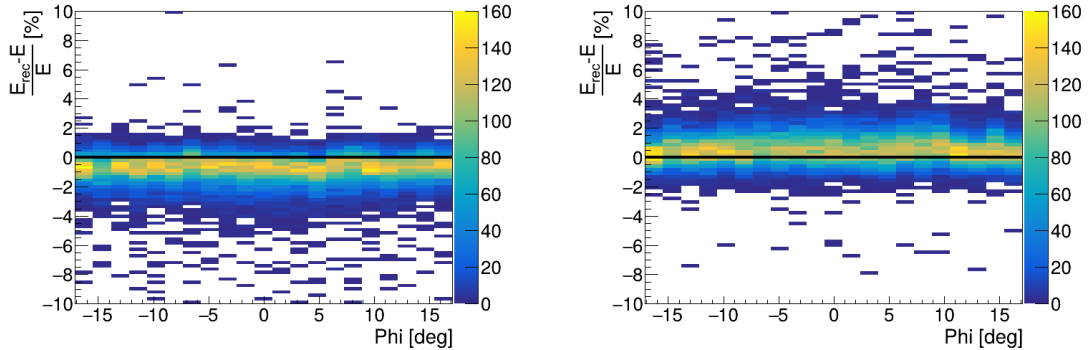


Figure 5.10 Dependence on theta of relative differences of reconstructed Runge-Kutta versus simulated energy for the Runge-Kutta fit for electrons (left) and positrons (right).

At first, few tracks with randomized initial parameters (same as the Runge-Kutta sample in Sec. 3.2.1) were generated for preliminary testing. Later, a sample with a grid-like distribution of track parameters was generated (see Sec. 3.1.2 for details). This allows us to test the performance of energy reconstruction from the microscopic tracks reconstructed with the discrete map inversion reconstruction.

The dependence of the resulting relative differences of reconstructed Runge-Kutta versus simulated energy for electron and positron tracks are shown in Figs. 5.9 to 5.11, the overall resolution without corrections is shown in Fig. 5.12. We can see that electrons, as well as tracks with high values of θ , are reconstructed with a higher precision thanks to the larger drift distance of ionization electrons, which results in their spreading across more readout channels (pads and time bins). The energy of electron tracks, especially for high energies, tends to be overestimated (and vice versa for positrons). This is related to the uncorrected shift in the map inversion z -coordinate reconstruction as seen from the residuals in Fig. 4.14. This shift is caused by non-zero initial velocities of ionization electrons that is not accounted for by the map. It has opposite directions for electrons and positrons, because the ionization electrons are more likely to follow the direction of the ionizing particle, and it deforms the track, since it strengthens as the track curves. The effect is more pronounced for higher energies, where the curve is more sensitive to slight changes, as shown in Fig. 3.4.

Since the Runge-Kutta fit is quite slow (each step of the MIGRAD algorithm has to simulate a new track), we use the circle-and-lines fit to provide a fast

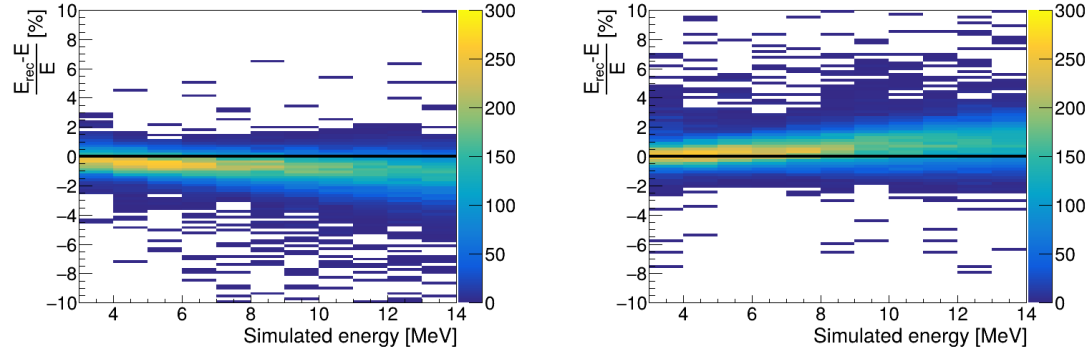


Figure 5.11 Dependence on simulated energy of relative differences of reconstructed Runge-Kutta versus simulated energy for the Runge-Kutta fit for electrons (left) and positrons (right).

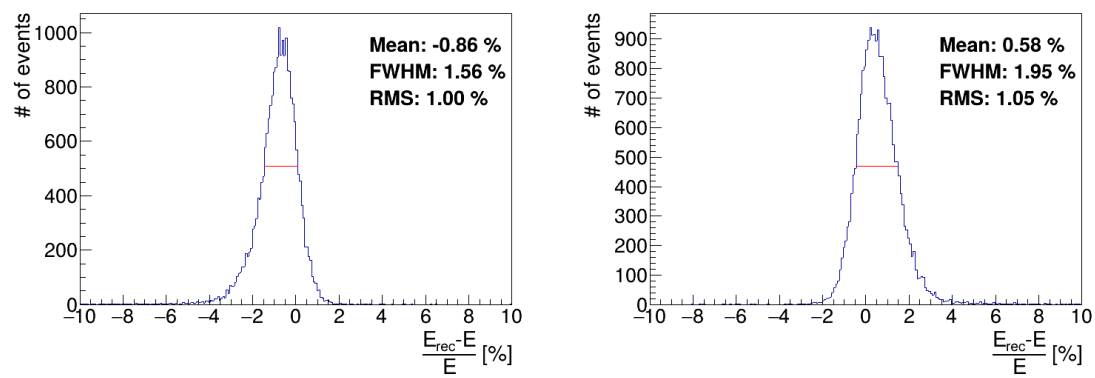


Figure 5.12 The overall relative differences of reconstructed versus simulated energy for the Runge-Kutta fit for electrons (left) and positrons (right).

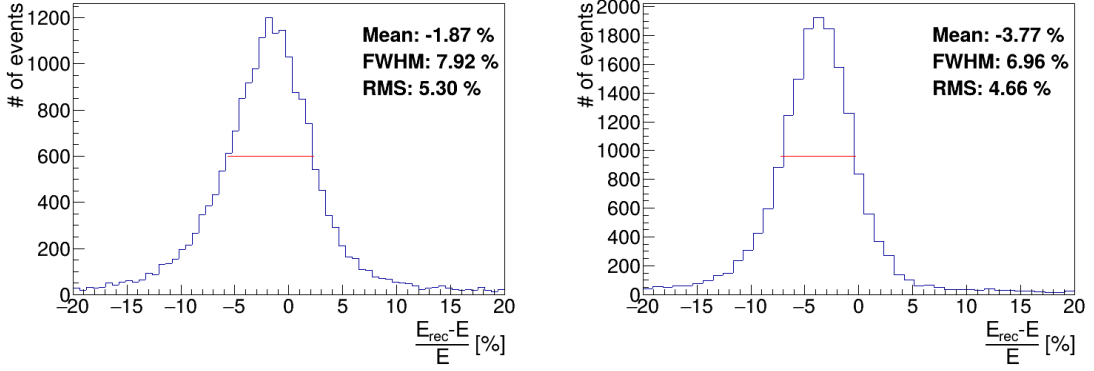


Figure 5.13 The overall relative differences of reconstructed versus simulated energy for the circle-and-lines (average field, corrected) for electrons (left) and positrons (right).

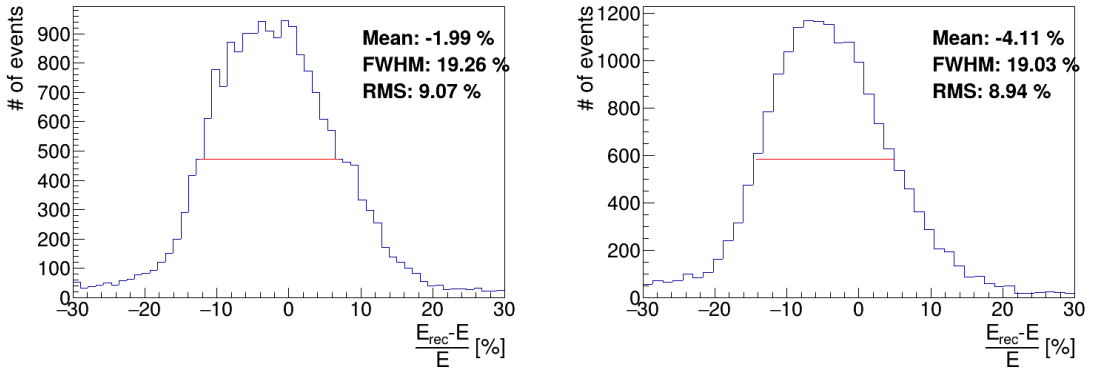


Figure 5.14 The overall relative differences of reconstructed versus simulated energy for the circle-and-lines (middle field) for electrons (left) and positrons (right).

estimate, and to ensure the fit convergence. From Fig. 5.5, we see that the average field method offers the best estimate when corrected. We can again save both estimates from the circle-and-lines fit, this time measuring its performance on a track reconstructed with discrete map inversion. The resulting histograms for electron and positron tracks are shown in Figs. 5.13 and 5.14. We again find that the average field method performs much better.

Conclusion

We have developed and implemented several methods for the reconstruction of electron and positron trajectories inside the Orthogonal Fields Time Projection Chambers (OFTPCs) that will be used in the X17 project at the Institute of Experimental and Applied Physics, Czech Technical University in Prague (IEAP, CTU) to confirm or disprove the ATOMKI anomaly [1]. We tested these methods on simulated tracks and made a preliminary estimate of achievable energy resolution.

We used the Garfield++ toolkit [52] for simulations in combination with the ROOT framework [56] for data analysis and visualization. Some of our more demanding simulations were run on the MetaCentrum grid [54]. The main method of track simulation was the microscopic simulation (provided by the `Avalanche-Microscopic` class), which follows ionization electrons from collision to collision.

Track Reconstruction

The inhomogeneous magnetic field created by permanent magnets is perpendicular to the electric field of the chambers and has a significant effect on the drift of ionization electrons (as demonstrated in Sec. 4.1). For this reason, we created the ionization electron map, i.e., a mapping from the detector space \mathcal{D} (coordinates (x, y, z)), where the initial positions of ionization electrons lie, to the readout space \mathcal{R} (coordinates (x', y', t)), where their endpoints on the readout plane lie. The map was simulated using the microscopic simulation. One hundred electrons with low initial velocity were simulated for each point on a Cartesian grid to get their mean readout coordinates and their covariance. Two gas mixtures 90:10 and 70:30 Ar:CO₂ were compared. In the former, the drift velocity is significantly higher, leading to increased effect of the magnetic field and larger diffusion (see, for example, Fig. 4.9a).

To use the map in reconstruction, we have to invert it. We implemented two methods – a gradient descent algorithm that finds a minimum in the trilinearly interpolated map, and a polynomial interpolation on the inverse grid in the readout space (where we know the inverse from the simulation). Both methods reach almost identical result for the testing track, while the latter is much faster, does not require optimization of parameters, and can be accelerated by precalculating the interpolation coefficients in the future if needed. The reconstruction was shown to be accurate with less than 2 mm FWHM, although a slight shift in the z -coordinate was detected when accounting for different initial velocities of the ionization electrons (see Figs. 4.13 and 4.14).

The discrete reconstruction takes into account the anode segmentation into pads and the finite size of the time bins. It neglects the gaps between the pads and assumes an ideal readout of charge, counting each individual electron hitting the pad. Charge multiplication in the triple-GEM stack used in the OFTPC is not taken into account. For each pad/time-bin combination, we use the map inversion to reconstruct its center. Reconstruction of detector coordinates corresponding to electrons hitting the pad 12 near the magnet pole (Figs. 4.15 and 4.16) show that interpolation on the inverse grid behaves pathologically for large distortions, unlike the much slower gradient descent algorithm, likely because of large coefficients of the quadratic and cubic terms.

Energy Reconstruction

To reconstruct energy of a particle in a OFTPC, we assess its curvature in the inhomogeneous magnetic field. Preliminary tests were done using tracks reconstructed with the map with no discretization. At first, we tested a cubic spline fit, where the radius of curvature can be determined analytically. This approach turned out to be unpractical because of relatively low speed and necessity to create the energy estimate from the radius and magnetic field at different points on the track (see Fig. 5.1).

Another tested approach (at first as a 2D version without pads, later in 3D with pads) was the fit with circular arc with smoothly attached lines, which is the shape of trajectory of a particle crossing a finite volume with homogeneous magnetic field oriented perpendicularly to the particles velocity vector. This way we get a single reconstructed radius of curvature, however, since the magnetic field varies greatly along the track inside the OFTPC volume, it is not clear, which value of magnetic field to use to calculate the energy. Two simple estimates were implemented:

1. using the value at the point, where the track crosses the middle x -coordinate, and
2. using the average value along the circular arc in the fit,

in both cases, only the component perpendicular to the plane of the fit is considered. The three dimensional version of the fit has four free parameters (radius, length of the first line, length of the circular arc, and rotation angle around the first line). In order for the fit to converge correctly in all cases, the parameter bounds have to be set carefully. Disallowing pathological values that are not expected for any real track may cause the MIGRAD algorithm to converge at the bound. The fit was successfully tested on a sample of Runge-Kutta tracks described in Sec. 3.2.1; the results in Fig. 5.5 show that the average field estimate systematically underestimates the energy of the track, but its FWHM is much smaller than that of the middle field estimate.

The best developed method was the Runge-Kutta fit. In a simplified model, we assume that the previous layers of detectors will provide us with exact initial position and direction of the particle, when entering the OFTPC. We can then use 4th-order Runge-Kutta numerical integration to simulate such a trajectory for different energies. In order to speed up the fit and ensure convergence of the fit, we use a corrected estimate from the circle-and-lines fit with average field as a starting point. We tested this method on a grid-like sample of microscopic tracks, described in Sec. 3.1.2, fitting tracks reconstructed with the discrete map inversion. As shown in Fig. 5.12, we can reach energy resolution (FWHM) 1.56 % for electrons (which curve away from the readout, enabling charge spreading across multiple channels) and 1.95 % for positrons without correcting systematic errors dependent on the track parameters, assuming an ideal charge readout with no noise and no amplification.

The code used in this thesis, and in related work, is available publicly at <https://github.com/Vavrikus/x17-utef>.

Future

In order to develop a functioning algorithm for the real detector, there are still many things left to account for. Here are some examples of what steps can or will be taken next.

Simulations

There are several important factors that need to be considered when simulating the detector response:

- Charge multiplication on the triple-GEM and limited efficiency of the read-out. In some cases, the spreading of charge between multiple pads during multiplication might have a positive effect on the resolution.
- Noise in the data. We are currently tuning an algorithm for track de-noising using a convolutional neural network [58].
- Delta electrons released by the particle.
- Electron attachment and Penning transfer in the gas mixture. Influence of even small amounts of other gases needs to be considered.
- Energy loss of the primary electrons and positrons.
- Better simulation of magnetic and electric fields; so far we have been assuming that the electric field is homogeneous. A simulation of the triple GEM could be included, but some simplifications would be necessary, since the microscopic simulation needed for such a structure is extremely time consuming.
- Account for the triggering in MWPC and Timepix3 (TPX3) detector layers. While a small uncertainty of the drift time measurement may not be relevant for the energy reconstruction in a standard TPC with a homogeneous magnetic field, a shift of the entire trajectory along the z -coordinate in our detector changes the magnetic field along the track, and therefore the reconstructed energy.
- An optimization study of the pad layout is possible with the current algorithm.

It might be also useful to use a faster simulation method for more robust reconstruction testing. Currently, a simple Monte Carlo simulation, using the covariance matrices from the map simulation, is implemented and can be used along with HEED to simulate tracks similar to the microscopic ones. The microscopic simulation is very time consuming, we have already spent 25 165.6 CPU days during the simulation of the grid-like testing sample, and partly during the map simulation.

Experimental calibration

To achieve the best results, the reconstruction needs to be calibrated using measurements from the real detector. This includes:

- measurement of the magnetic field of the permanent magnets,
- reconstruction of straight tracks from laser or muons, and
- reconstruction of electrons with known energy distribution, if possible.

Reconstruction algorithm

Several tweaks are being considered to improve the reconstruction algorithm in the future:

- Optimization — multiple Runge-Kutta fits could be run with gradually decreasing step size.
- Estimation of errors using the error of the fit.
- Accounting for the variable initial velocity of ionization electrons produced by the incident particle. The current map uses initial energy 0.1 eV, which led to systematic errors in the z -coordinate reconstruction, as shown in Fig. 4.14. Another map could be simulated with different initial direction and energy distributions, tracking the ionization electrons only until they slow down to the mean drift velocity, and using the already simulated map from there. Alternatively, we could correct the reconstructed z -coordinate based on the reconstructed curve of the track using some rough estimate obtained from a grid-like simulation of microscopic tracks.
- If a speed optimization is needed, a discrete pad map could be calculated ahead of time, instead of repeated calculation during the reconstruction. At this moment, the most computationally expensive part of the reconstruction are the individual fits. The slower gradient descent map inversion technique may be used to avoid issues with the interpolation on the inverse grid (shown in Fig. 4.15).
- At the end of the fitting procedure, we could refine the origin and the initial direction of the track obtained from the previous detector layers with some kind of global fit.
- Using maximum likelihood for the energy fit, instead of the least square method. Currently, in the discrete map inversion reconstruction, we reconstruct the center of each hit pad and time bin. However, due to the drift distortion, this may not correspond to the most likely, or even the average position to be hit by an ionization electron.

In theory, we could by taking into account the whole map \mathcal{M} (including the covariance matrices, describing the multivariate normal distribution that describes each map point well according to our preliminary tests), we could make an "inverse map" from \mathcal{R} to distributions on \mathcal{D} . We could achieve this by taking the normalized probability density of an electron with initial

coordinates (x, y, z) having readout coordinates (x', y', t) . If we fix (x', y', t) , we get an unnormalized probability density $f(x, y, z) = \mathcal{M}_{(x,y,z)}(x', y', t)$ (assuming that all initial coordinates are a priori equally likely). This could potentially improve the discrete reconstruction if we take the mean value of this probability density across the pad and time bin

$$f_{\text{pad, bin}}(x, y, z) = \frac{1}{A_{\text{pad}}\Delta t_{\text{bin}}} \int_{\text{pad, bin}} \mathcal{M}_{(x,y,z)}(x', y', t) dx' dy' dt \quad (5.33)$$

and using it for a likelihood fit instead of using least squares. This still assumes that all initial coordinates are equally likely which is clearly not the case for a primary particle track. In the future, we could even use the fast track simulation with the map (it should be possible to make around 1000 tracks or more per minute per core with current settings), create a big set of tracks with reasonable parameters and use these to get an approximation of the probability distribution of the detector response. Some approximations would be necessary when interpreting the data to decrease the degrees of freedom of this distribution (we would have to pick a set of parameters and assume that some of them are independent). This could give us an idea about the best achievable resolution (how significantly will the detector response differ for a given change in energy). If the difference is significant, we could try to further improve the likelihood fit.

Bibliography

1. KRASZNAHORKAY, A. J. et al. Observation of Anomalous Internal Pair Creation in ${}^8\text{Be}$: A Possible Indication of a Light, Neutral Boson. *Phys. Rev. Lett.* 2016, vol. 116, no. 4. ISSN 1079-7114. Available from DOI: 10.1103/physrevlett.116.042501.
2. MARX, Jay N.; NYGREN, David R. The Time Projection Chamber. *Phys. Today*. 1978, vol. 31, no. 10, pp. 46–53. ISSN 0031-9228. Available from DOI: 10.1063/1.2994775.
3. INSTITUTE OF EXPERIMENTAL AND APPLIED PHYSICS, CZECH TECHNICAL UNIVERSITY IN PRAGUE. *The search for the X17* [<https://aladdin.utef.cvut.cz/projekty/vdg/x17/>]. 2025. Project page of the Van de Graaff accelerator laboratory (VdG) at ÚTEF ČVUT — experiment X17.
4. ROSE, M. E. Internal Pair Formation. *Phys. Rev.* 1949, vol. 76, pp. 678–681. Available from DOI: 10.1103/PhysRev.76.678.
5. SAS, N. J. et al. *Observation of the X17 anomaly in the ${}^7\text{Li}(p,e^+e^-){}^8\text{Be}$ direct proton-capture reaction*. 2022. Available from arXiv: 2205.07744 [nucl-ex].
6. KRASZNAHORKAY, A. J. et al. New anomaly observed in ${}^{12}\text{C}$ supports the existence and the vector character of the hypothetical X17 boson. *Phys. Rev. C*. 2022, vol. 106, p. L061601. Available from DOI: 10.1103/PhysRevC.106.L061601.
7. KRASZNAHORKAY, A. J. et al. *New evidence supporting the existence of the hypothetic X17 particle*. 2019. Available from arXiv: 1910.10459 [nucl-ex].
8. KRASZNAHORKAY, A. J. et al. New anomaly observed in ${}^4\text{He}$ supports the existence of the hypothetical X17 particle. *Phys. Rev. C*. 2021, vol. 104, no. 4. ISSN 2469-9993. Available from DOI: 10.1103/physrevc.104.044003.
9. ESSIG, R. et al. *Dark Sectors and New, Light, Weakly-Coupled Particles*. 2013. Available from arXiv: 1311.0029 [hep-ph].
10. DE BOER, F.W.N. et al. A deviation in internal pair conversion. *Phys. Lett. B*. 1996, vol. 388, no. 2, pp. 235–240. ISSN 0370-2693. Available from DOI: [https://doi.org/10.1016/S0370-2693\(96\)01311-1](https://doi.org/10.1016/S0370-2693(96)01311-1).
11. BOER, F W N de et al. Excess in nuclear pairs near 9 MeV/ invariant mass. *J. Phys. G: Nucl. Part. Phys.* 1997, vol. 23, no. 11, p. L85. Available from DOI: 10.1088/0954-3899/23/11/001.
12. BOER, F W N de et al. Further search for a neutral boson with a mass around 9 MeV/c². *J. Phys. G: Nucl. Part. Phys.* 2001, vol. 27, no. 4, p. L29. Available from DOI: 10.1088/0954-3899/27/4/102.
13. VITÉZ, Attila et al. Anomalous Internal Pair Creation in ${}^8\text{Be}$ as a Signature of the Decay of a New Particle. *Acta Phys. Pol. B - ACTA PHYS POL B*. 2008, vol. 39, p. 483.
14. KRASZNAHORKAY, A. et al. Searching for a light neutral axial-vector boson in isoscalar nuclear transitions. *Frascati Phys. Ser.* 2012, vol. 56, p. 86.

15. TILLEY, D.R. et al. Energy levels of light nuclei A=8,9,10. *Nucl. Phys. A*. 2004, vol. 745, no. 3, pp. 155–362. ISSN 0375-9474. Available from DOI: <https://doi.org/10.1016/j.nuclphysa.2004.09.059>.
16. TILLEY, D.R. et al. Energy levels of light nuclei A = 4. *Nucl. Phys. A*. 1992, vol. 541, no. 1, pp. 1–104. ISSN 0375-9474. Available from DOI: [https://doi.org/10.1016/0375-9474\(92\)90635-W](https://doi.org/10.1016/0375-9474(92)90635-W).
17. AJZENBERG-SELOVE, F. Energy levels of light nuclei A = 11,12. *Nucl. Phys. A*. 1990, vol. 506, no. 1, pp. 1–158. ISSN 0375-9474. Available from DOI: [https://doi.org/10.1016/0375-9474\(90\)90271-M](https://doi.org/10.1016/0375-9474(90)90271-M).
18. KÁLMÁN, Péter; KESZTHELYI, Tamás. Anomalous internal pair creation. *The Eur. Phys. J. A*. 2020, vol. 56. Available from DOI: [10.1140/epja/s10050-020-00202-z](https://doi.org/10.1140/epja/s10050-020-00202-z).
19. ALEKSEJEVS, A. et al. *A Standard Model Explanation for the "ATOMKI Anomaly"*. 2021. Available from arXiv: [2102.01127 \[hep-ph\]](https://arxiv.org/abs/2102.01127).
20. FENG, Jonathan L. et al. Protophobic Fifth-Force Interpretation of the Observed Anomaly in ${}^8\text{Be}$ Nuclear Transitions. *Phys. Rev. Lett.* 2016, vol. 117, p. 071803. Available from DOI: [10.1103/PhysRevLett.117.071803](https://doi.org/10.1103/PhysRevLett.117.071803).
21. KRASZNAHORKAY, Attila J. et al. An Update of the Hypothetical X17 Particle. *Universe*. 2024, vol. 10, no. 11. ISSN 2218-1997. Available from DOI: [10.3390/universe10110409](https://doi.org/10.3390/universe10110409).
22. ANH, Tran The et al. Checking the ${}^8\text{Be}$ Anomaly with a Two-Arm Electron Positron Pair Spectrometer. *Universe*. 2024, vol. 10, no. 4, p. 168. ISSN 2218-1997. Available from DOI: [10.3390/universe10040168](https://doi.org/10.3390/universe10040168).
23. ABRAAMYAN, Kh. U. et al. *Observation of structures at ~ 17 and $\sim 38 \text{ MeV}/c^2$ in the $\gamma\gamma$ invariant mass spectra in pC , dC , and dCu collisions at p_{lab} of a few GeV/c per nucleon*. 2023. Available from arXiv: [2311.18632 \[hep-ex\]](https://arxiv.org/abs/2311.18632).
24. THE MEG II COLLABORATION et al. *Search for the X17 particle in ${}^7\text{Li}(p, e^+e^-){}^8\text{Be}$ processes with the MEG II detector*. 2024. Available from arXiv: [2411.07994 \[nucl-ex\]](https://arxiv.org/abs/2411.07994).
25. ALI, Babar et al. Measurement of angular correlations in low-energy internally-created $e-e+$ pairs using Timepix3 pixel detectors. *Radiat. Meas.* 2025, vol. 184, p. 107424. ISSN 1350-4487. Available from DOI: <https://doi.org/10.1016/j.radmeas.2025.107424>.
26. ALI, Babar et al. *Study of electron tracks in Timepix3 detector at kinetic energies of 1 and 1.5 MeV*. 2024. Available from arXiv: [2411.19081 \[physics.ins-det\]](https://arxiv.org/abs/2411.19081).
27. HILKE, H J. Time Projection Chambers. *Rep. Prog. Phys.* 2010, vol. 73, no. 11, p. 116201. Available from DOI: [{10.1088/0034-4885/73/11/116201}](https://doi.org/10.1088/0034-4885/73/11/116201).
28. NAVAS, S. et al. Review of particle physics. *Phys. Rev. D*. 2024, vol. 110, no. 3, p. 030001. Available from DOI: [10.1103/PhysRevD.110.030001](https://doi.org/10.1103/PhysRevD.110.030001).
29. GRUPEN, Claus. Physics of particle detection. In: *AIP Conference Proceedings*. AIP, 2000, vol. 536, pp. 3–34. ISSN 0094-243X. Available from DOI: [10.1063/1.1361756](https://doi.org/10.1063/1.1361756).

30. ABED ABUD, Adam et al. A Gaseous Argon-Based Near Detector to Enhance the Physics Capabilities of DUNE. 2022. Available from DOI: [10.48550/arXiv.2203.06281](https://doi.org/10.48550/arXiv.2203.06281).
31. TOWNSEND, J. S. The Conductivity produced in Gases by the Motion of Negatively-charged Ions. *Nature*. 1900, vol. 62, no. 1606, pp. 340–341. Available from DOI: [10.1038/062340b0](https://doi.org/10.1038/062340b0).
32. AIHARA, H. et al. Spatial Resolution of the PEP-4 Time Projection Chamber. *IEEE Trans. on Nucl. Sci.* 1983, vol. 30, no. 1, pp. 76–81. Available from DOI: [10.1109/TNS.1983.4332223](https://doi.org/10.1109/TNS.1983.4332223).
33. LOKEN, Stewart C. et al. Performance of the Signal Processing System for the Time Projection Chamber. *IEEE Trans. on Nucl. Sci.* 1983, vol. 30, no. 1, pp. 162–166. Available from DOI: [10.1109/TNS.1983.4332243](https://doi.org/10.1109/TNS.1983.4332243).
34. COWAN, G. D. *Inclusive π^\pm , K^\pm , and p , \bar{p} production in e^+e^- annihilation at $\sqrt{s} = 29$ GeV*. 1988. Available from DOI: [10.2172/5188194](https://doi.org/10.2172/5188194). Lawrence Berkeley National Lab. (LBNL), Berkeley, CA (United States).
35. ALME, J. et al. The ALICE TPC, a large 3-dimensional tracking device with fast readout for ultra-high multiplicity events. *Nucl. Instrum. Methods Phys. Res. Sect. A: Accel. Spectrom. Detect. Assoc. Equip.* 2010, vol. 622, no. 1, pp. 316–367. ISSN 0168-9002. Available from DOI: <https://doi.org/10.1016/j.nima.2010.04.042>.
36. HAUER, Philip. The upgraded ALICE TPC. *Nucl. Instrum. Methods Phys. Res. Sect. A: Accel. Spectrom. Detect. Assoc. Equip.* 2022, vol. 1039, p. 167023. ISSN 0168-9002. Available from DOI: <https://doi.org/10.1016/j.nima.2022.167023>.
37. DI MAURO, A. Particle identification methods other than RICH. *Nucl. Instrum. Methods Phys. Res. Sect. A: Accel. Spectrom. Detect. Assoc. Equip.* 2020, vol. 952, p. 162124. ISSN 0168-9002. Available from DOI: <https://doi.org/10.1016/j.nima.2019.04.078>. 10th International Workshop on Ring Imaging Cherenkov Detectors (RICH 2018).
38. ADAMOVÁ, D. et al. The CERES/NA45 radial drift Time Projection Chamber. *Nucl. Instrum. Methods Phys. Res. Sect. A: Accel. Spectrom. Detect. Assoc. Equip.* 2008, vol. 593, no. 3, pp. 203–231. ISSN 0168-9002. Available from DOI: [10.1016/j.nima.2008.04.056](https://doi.org/10.1016/j.nima.2008.04.056).
39. BIAGI, S.F. Monte Carlo simulation of electron drift and diffusion in counting gases under the influence of electric and magnetic fields. *Nucl. Instrum. Methods Phys. Res. Sect. A: Accel. Spectrom. Detect. Assoc. Equip.* 1999, vol. 421, no. 1, pp. 234–240. ISSN 0168-9002. Available from DOI: [https://doi.org/10.1016/S0168-9002\(98\)01233-9](https://doi.org/10.1016/S0168-9002(98)01233-9).
40. KHAW, Kim Siang et al. *Status of the muEDM experiment at PSI*. 2023. Available from arXiv: [2307.01535 \[hep-ex\]](https://arxiv.org/abs/2307.01535).
41. ACKERMANN, K.H. et al. The forward time projection chamber in STAR. *Nucl. Instrum. Methods Phys. Res. Sect. A: Accel. Spectrom. Detect. Assoc. Equip.* 2003, vol. 499, no. 2, pp. 713–719. ISSN 0168-9002. Available from DOI: [https://doi.org/10.1016/S0168-9002\(02\)01968-X](https://doi.org/10.1016/S0168-9002(02)01968-X). The Relativistic Heavy Ion Collider Project: RHIC and its Detectors.

42. ALBAYRAK, I. et al. Design, construction, and performance of the GEM based radial time projection chamber for the BONuS12 experiment with CLAS12. *Nucl. Instrum. Methods Phys. Res. Sect. A: Accel. Spectrom. Detect. Assoc. Equip.* 2024, vol. 1062, p. 169190. ISSN 0168-9002. Available from DOI: <https://doi.org/10.1016/j.nima.2024.169190>.
43. ANDERSON, E. et al. Observation of the effect of gravity on the motion of antimatter. *Nature.* 2023, vol. 621, pp. 716–722. Available from DOI: 10.1038/s41586-023-06527-1.
44. Design of a Radial TPC for Antihydrogen Gravity Measurement with ALPHA-g. In: *Proceedings of the 12th International Conference on Low Energy Antiproton Physics (LEAP2016)*. [N.d.]. Available from DOI: 10.7566/JPSCP.18.011015.
45. CAPRA, A. Antihydrogen annihilation detection: the ALPHA-g radial TPC. *PoS.* 2025, vol. EXA-LEAP2024, p. 063. Available from DOI: 10.22323/1.480.0063.
46. WIECHULA, Jens; CHRISTIANSEN, Peter. *The ALICE Time Projection Chamber* [https://www.hep.lu.se/staff/christiansen/teaching/spring_2013/the_alice_tpc.pdf]. 2013. Slides credited to J. Wiechula; hosted on Lund University website.
47. HILDÉN, T. et al. Optical quality assurance of GEM foils. *Nucl. Instrum. Methods Phys. Res. Sect. A: Accel. Spectrom. Detect. Assoc. Equip.* 2015, vol. 770, pp. 113–122. ISSN 0168-9002. Available from DOI: 10.1016/j.nima.2014.10.015.
48. AHMED, Misbah Uddin. *Simulation of the electron and ion movement through a 4-GEM stack.* 2021. Institut für Kernphysik.
49. ANSYS INC. *ANSYS Maxwell, Electromagnetic Field Simulation Software.* Canonsburg, PA, USA: ANSYS Inc., 2025. <https://www.ansys.com/products/electronics/ansys-maxwell>.
50. MARMELAD. *3D interpolation2.svg.* 2025. Available also from: https://commons.wikimedia.org/wiki/File:3D_interpolation2.svg. Licensed under CC BY-SA 3.0 (<https://creativecommons.org/licenses/by-sa/3.0/legalcode>). Accessed: 9-April-2025.
51. CMGLEE. *Trilinear interpolation visualisation.* 2025. Available also from: https://commons.wikimedia.org/wiki/File:Trilinear_interpolation_visualisation.svg. Licensed under CC BY-SA 3.0 (<https://creativecommons.org/licenses/by-sa/3.0/legalcode>). Accessed: 26-March-2025.
52. Garfield++ [<https://garfieldpp.web.cern.ch/garfieldpp/>]. [N.d.]. Accessed: 2023-05-18.
53. SMIRNOV, I.B. Modeling of ionization produced by fast charged particles in gases. *Nucl. Instrum. Methods Phys. Res. Sect. A: Accel. Spectrom. Detect. Assoc. Equip.* 2005, vol. 554, no. 1, pp. 474–493. ISSN 0168-9002. Available from DOI: <https://doi.org/10.1016/j.nima.2005.08.064>.
54. About MetaCentrum [<https://metavo.metacentrum.cz/en/about/index.html>]. 2023. Accessed: 2024-11-27.

55. SCOTT, DAVID W. On optimal and data-based histograms. *Biometrika*. 1979, vol. 66, no. 3, pp. 605–610. ISSN 0006-3444. Available from DOI: 10.1093/biomet/66.3.605.
56. BRUN, Rene; RADEMAKERS, Fons. Root — An Object Oriented Data Analysis Framework. *Nucl. Instrum. Methods Phys. Res. Sect. A: Accel. Spectrom. Detect. Assoc. Equip.* 1997, vol. 389, no. 1–2, pp. 81–86. Available from DOI: 10.1016/s0168-9002(97)00048-x. Proceedings AIHENP'96 Workshop, Lausanne, Sep. 1996, See also <https://root.cern/>, Paper published in the Linux Journal, Issue 51, July 1998.
57. FREEDMAN, David A.; DIACONIS, Persi. On the histogram as a density estimator:L2 theory. *Zeitschrift fur Wahrscheinlichkeitstheorie und Verwandte Gebiete*. 1981, vol. 57, pp. 453–476. Available also from: <https://api.semanticscholar.org/CorpusID:14437088>.
58. GAJDOŠ, Matěj et al. Denoising 3D Time Projection Chamber data using convolutional neural networks. *J. Instrum.* 2025, vol. 20, no. 05, p. C05014. Available from DOI: 10.1088/1748-0221/20/05/C05014.

Acknowledgments:

- MetaCentrum grid: Computational resources were provided by the e-INFRA CZ project (ID:90254), supported by the Ministry of Education, Youth and Sports of the Czech Republic.
- Figures 2.12, 2.15, 3.2, 4.4, 5.3 and 5.6 to 5.8 were made with GeoGebra®.
- This work was supported by the GACR - Czech Science Foundation grant GA21-21801S.

List of Figures

1.1	The ATOMKI anomalous IPC measured for different nuclei.	5
1.2	Results from the Hanoi spectrometer - angular e^+e^- pair correlations measured in the ${}^7\text{Li}(p, e^+e^-){}^8\text{Be}$ reaction at $E_p = 1225$ keV [22].	6
1.3	Results from the MEG II experiments – angular correlation of e^+e^- pairs with $E_{\text{sum}} \in [16, 20]$ MeV measured in the ${}^7\text{Li}(p, e^+e^-){}^8\text{Be}$ reaction with proton beam energies 500 and 1080 keV. The 500 keV dataset is fitted with Monte Carlo of both the IPC deexcitation and the EPC produced by gammas [24].	7
1.4	Schematics of the detector at the Van der Graaff facility at IEAP, CTU [3].	7
2.1	Particle identification in the PEP-4 TPC at SLAC based on the energy loss per distance $\frac{dE}{dx}$ in the 80:20 Ar:CH ₄ filling at 8.5 atm pressure [29, 30].	9
2.2	Schematic view of the PEP-4 TPC [33]. A charged particle produced in a collision in the beam pipe creates a spiral ionization track in the magnetic field. The central cathode then accelerates ionization electrons towards the endcap anode wires where they are multiplied and read out. A TPC sector with a detailed view of one of the pad rows is shown on the right [34].	12
2.3	Schematic view of the ALICE TPC [36]. The readout at each endcap is divided into 18 sectors, each subdivided into an Inner Readout Chamber (IROC) with one GEM stack and Outer Readout Chamber (OROC) with three GEM stacks. A visualization of a GEM stack is on the right [37].	13
2.4	Experimental setup of the CERES/NA45 experiment with two Ring Imaging Cherenkov Counters (RICHs) on the left and a rTPC on the right. The magnetic field (red) is generated by two solenoidal coils (blue) with opposite polarity. Produced ionization electrons drift outward radially towards the readout chamber (yellow) [38].	14
2.5	Cross section of a CERES/NA45 readout MWPC. The wires are stretched in the azimuthal direction above the pad plane. The gating grid controls the passage of electrons and ions. [38].	14
2.6	Schematic view of the BONuS12 rTPC [42].	15
2.7	Schematic view of the ALPHA-g detector [44].	16
2.8	Schematic view of the ALICE MWPC readout (working principle) [46].	17
2.9	Gas Electron Multiplier (GEM).	18
2.10	Garfield simulation of an avalanche in a GEM hole [48]. An incoming electron (orange) is accelerated in the strong electric field of the GEM and causes further ionization multiplying the number of free electrons (orange). Most of the produced cations (red) are captured by the GEM cathode.	18
2.11	MICRO-MEsh GAseous Structure (Micromegas) [28].	19
2.12	Schematics of the first sector OFTPC with detector space coordinates. Made with GeoGebra®.	21

2.14 Magnetic field simulation results. The OFTPC volume and the vacuum tube are marked with black lines, the magnets are marked with red lines. In current design of the real detector, magnets are slightly shifted compared to the simulation.	22
2.13 Pad layout of the OFTPC and its parameters. Pads 102, 124 and 127 are irregular, the rest has the same dimensions.	22
2.15 Visualization of trilinear interpolation as a composition of linear interpolations (inspired by [50]). We want to interpolate the value in the red point C . First we interpolate between the four pairs of blue points sharing the last two indices along the x -axis (Eq. 2.15), then between the two pairs of the resulting green points along the y -axis (Eq. 2.16) and finally between the two resulting orange points along the z -axis to get the final red value (Eq. 2.17). Made with GeoGebra®.	23
2.16 Geometric interpretation of trilinear interpolation as expressed in Eq. 2.19. The colored dots represent the values in given points and the colored boxes represent the volume in the opposite corner by which the corresponding values are multiplied. The black dot represents the interpolated value which is multiplied by the entire volume [51].	24
3.1 Comparison of drift lines for two different gas mixtures 90:10 and 70:30 Ar:CO ₂ . The electron track is marked in black, the drift lines of the ionization electrons are marked in orange. In this example, we assume a larger OFTPC volume with readout at 8 cm. Small curvature of the track in the YZ projection is caused by the tilt of the magnetic field in the bottom half of the Orthogonal Fields TPC (OFTPC).	27
3.2 A visualization of a set of tracks from the grid-like testing sample with the same kinetic energy. Made with GeoGebra®.	28
3.3 A comparison of the HEED track from the microscopic simulation in Sec. 3.1.1 with a Runge-Kutta track with the same initial parameters and $\tau_{\text{step}} = 0.1$ ps (reducing the step further doesn't make a visible difference). In the view of the tracks on the left, the distance of the HEED ionization electrons from the RK4 track is exaggerated 1000 \times . On the right, the dependence of the HEED electrons residuals (i.e., their shortest distance to the RK4 track) on their z -coordinate is shown.	29
3.4 Set of 25 Runge-Kutta tracks with initial position (6.51, 0, 0) cm, orientation (1, 0, 0), and energies 3 – 13 MeV.	30
4.1 Linear fit of the drift time t dependence on the distance to the readout $d_r = 8$ cm – z for the ionization electrons in 90:10 (left) and 70:30 (right) Ar:CO ₂ gas composition. Only electrons inside the OFTPC (red) are fitted. The parameters are $v_d = 3.39$ cm/ μ s, $d_0 = -0.41$ cm for 90:10, and $v_d = 0.939$ cm/ μ s, $d_0 = -0.11$ cm for 70:30 Ar:CO ₂	32

4.2	Reconstruction (black) of the starting position of ionization electrons (red) using parameters obtained from the fit (Fig. 4.1). Two gas compositions 90:10 (left) and 70:30 Ar:CO ₂ (right) are compared.	32
4.3	Comparison of residuals (i.e., the distance from the reconstructed point to the simulated ionization electron starting point) dependence on x for two gas mixtures 90:10 (red) and 70:30 Ar:CO ₂ (blue).	33
4.4	A 3D visualization of the mapping of means $\bar{\mathcal{M}}$ for the 90:10 Ar:CO ₂ gas. A regular grid \mathbb{G} with $l = 1$ cm in the detector space is mapped to an irregular grid $\mathbb{G}^{-1} \equiv \bar{\mathcal{M}}(\mathbb{G})$ in the readout space. Made with GeoGebra®.	34
4.5	A test of the 90:10 Ar:CO ₂ map simulation with spacing $l = 1.5$ cm. The resulting drift lines of evenly spaced electrons are displayed in orange.	34
4.6	Dependence of the drift times of the simulated map $\bar{\mathcal{M}}$ on the z -coordinate. Two gas mixtures 90:10 (left) and 70:30 Ar:CO ₂ (right) are compared. The spread is caused by varying Lorentz angles.	35
4.7	The $x't$ projection of the $\mathcal{M}(\mathbb{G}_{y=0})$ mapping of a part of the regular grid \mathbb{G} . The means $\bar{\mathcal{M}}(\mathbb{G}_{y=0})$ are marked with red crosses, and the diffusion error is denoted by black 95% confidence error ellipses computed from the diagonalized covariance matrices $\mathcal{M}_{\Sigma}(\mathbb{G}_{y=0})$. Two gas mixtures 90:10 (left) and 70:30 Ar:CO ₂ (right) are compared. The first mixture shows differences of t for electrons with same initial z but different initial x . For the second mixture, these differences are negligible in comparison with the diffusion.	36
4.8	The regular grid \mathbb{G} projected by the mapping $\bar{\mathcal{M}}$ from the detector space onto the $x'y'$ plane (t is not plotted). Layers with lower z -coordinate (i.e., further away from the readout) are displayed with darker colors. The OFTPC volume is marked with black lines. Two gas mixtures 90:10 (left) and 70:30 Ar:CO ₂ (right) are compared.	36
4.9	The $\mathcal{M}(\mathbb{G}_{-8})$ mapping of the bottom ($z = -8$ cm) layer \mathbb{G}_{-8} of the regular grid $\mathbb{G} \subset \mathcal{D}$. It includes both the mapping of means $\bar{\mathcal{M}}$ and of covariances \mathcal{M}_{Σ} . Individual electrons from the map simulation are marked with red dots. Two gas mixtures 90:10 (left) and 70:30 Ar:CO ₂ (right) are compared.	37
4.10	The readout coordinate x' for points on the grid $\mathbb{G}_{y=0}$ plotted against their initial coordinate z . The means are marked with red crosses, the diffusion in x' is denoted by standard error bars. Two gas mixtures 90:10 (left) and 70:30 Ar:CO ₂ (right) are compared.	37
4.11	Reconstruction (black) of the starting position of ionization electrons (red) using the inversion of the ionization electron map. Two gas compositions 90:10 (left) and 70:30 Ar:CO ₂ (right) are compared.	41
4.12	Comparison of residuals from the RASD (black) and map inversion (red) reconstruction methods. Tracks in two different gas compositions 90:10 (left) and 70:30 Ar:CO ₂ (right) are compared (in the former gas mixture, the drift velocity is higher, therefore the distortion effects are more significant).	41

4.13	Map inversion reconstruction residuals (for the individual coordinates and total) of the testing track in 90:10 Ar:CO ₂ gas mixture.	42
4.14	Map inversion reconstruction residuals (for the individual coordinates and total) of the testing track in 70:30 Ar:CO ₂ gas mixture.	42
4.15	Reconstruction of detector coordinates for ionization electrons that are read out in a certain pad (number 66 near the center of the OFTPC, and number 12 near the magnet pole that suffers from large distortion effects, causing issues with interpolation on the inverse grid) and time bin. Boundaries of regions mapped to these discrete coordinates are shown in black, reconstructed center of the pad and time bin is shown in red, and map points used for the center reconstruction are shown in blue. Readout is placed at $z = -8$ cm.	44
4.16	Reconstruction of detector coordinates corresponding to pad 12 (near the magnet pole) for different time bins. Unlike Fig. 4.15, we used the gradient descent search, which handles the large distortion better. In its current unoptimized state, these figures took 280 times longer to produce, compared to the interpolation on the inverse grid.	45
4.17	Discrete reconstruction of an 8 MeV track from the grid-like testing sample (described in Sec. 3.1.2) with minimal values of θ and ϕ initial direction angles. The simulated ionization vertices are shown in red, the reconstructed track is shown with the colored boxes. The number of electrons in each pad/time bin is denoted with the size of the boxes and their color. The apparent discontinuity is caused by the charge spreading between two pad "columns".	45
5.1	Energy reconstruction of a 7.51 MeV track in a 70:30 Ar:CO ₂ gas mixture (described in detail in Sec. 3.1.1) using a cubic spline fit with four evenly spaced nodes of points reconstructed using the map.	49
5.2	Circle-and-lines 2D energy reconstruction of a 7.51 MeV track in a 70:30 Ar:CO ₂ gas mixture (described in detail in Sec. 3.1.1) reconstructed with the map. The fitted position of the nodes is $(x_1, z_1) = (5.20, -0.07)$ cm and $(x_2, z_2) = (14.43, -1.93)$ cm, the radius is $r = 20.79$ cm. The resulting energy is 7.70 MeV, the magnetic field along the track is shown on the right.	51
5.3	Visualization of the 3D geometry of the circle-and-lines fit and its parameters. Projection of some points on the XY plane is shown to better display the spatial arrangement. Made with GeoGebra®.	52
5.4	3D circle fit of an 8 MeV track (red points) from the grid-like testing sample (described in Sec. 3.1.2) with minimal values of θ and ϕ initial direction angles. Both fits of the original (green) and reconstructed track (blue) are shown. Resulting parameter values are given in Tab. 5.1.	54

5.5	Relative error of the energy of Runge-Kutta tracks reconstructed with the 3D circle-and-lines fit. The middle (left) and the average field (right) methods are compared. Dependence on the initial direction angles θ and φ is small in comparison (for this reason, the plots are not shown).	55
5.6	Demonstration of the convexity of the distance function $d(\alpha)$ for a circular track (see Eq. 5.29). Made with GeoGebra®.	57
5.7	An example track (red) with a polygonal chain approximation (green, representing a RK4 simulation). The distance of the point \mathbf{P} from the chain is found using a binary search among the distances to the vertices $d_{\mathbf{P}}(\tau_i)$ (blue) and subsequently calculating the distance to segments neighboring the found vertex (thus finding the minimum of the function $d'_{\mathbf{P}}(\tau)$, function $d_{\mathbf{P}}(\tau)$ for the actual track is showed for reference). This approach works if the condition 5.28 is satisfied, which is not the case for a point from the green area bordered by the normals at endpoints and the evolute of the track (orange). Made with GeoGebra®.	58
5.8	An exclusion area (green) of a track (red) bordered by its evolute and the normals at endpoints (orange), where the assumption 5.28 is violated. Unlike the track in Fig. 5.7, this track has a minimal curvature point in the middle, corresponding to the cusp on its evolute. Made with GeoGebra®.	58
5.9	Dependence on theta of relative differences of reconstructed Runge-Kutta versus simulated energy for the Runge-Kutta fit for electrons (left) and positrons (right).	59
5.10	Dependence on theta of relative differences of reconstructed Runge-Kutta versus simulated energy for the Runge-Kutta fit for electrons (left) and positrons (right).	59
5.11	Dependence on simulated energy of relative differences of reconstructed Runge-Kutta versus simulated energy for the Runge-Kutta fit for electrons (left) and positrons (right).	60
5.12	The overall relative differences of reconstructed versus simulated energy for the Runge-Kutta fit for electrons (left) and positrons (right).	60
5.13	The overall relative differences of reconstructed versus simulated energy for the circle-and-lines (average field, corrected) for electrons (left) and positrons (right).	61
5.14	The overall relative differences of reconstructed versus simulated energy for the circle-and-lines (middle field) for electrons (left) and positrons (right).	61

List of Tables

4.1	Comparison of parameters of two map simulations.	35
5.1	3D circle fit parameters of an 8 MeV track from the grid-like testing sample (described in Sec. 3.1.2) with minimal values of θ and ϕ initial direction angles.	54

List of Abbreviations

- ALPHA** Antihydrogen Laser Physics Apparatus
- BONuS12** Barely Off-shell NeUtron Structure 12 GeV
- GEM** Gas Electron Multiplier
- HEED** High Energy Electro-Dynamics
- IEAP, CTU** Institute of Experimental and Applied Physics, Czech Technical University in Prague
- IPC** Internal Pair Creation
- EPC** External Pair Creation
- FTPC** Forward TPC
- FWHM** Full Width at Half Maximum
- LArTPC** Liquid Argon TPC
- Micromegas** MICRO-MEsh Gaseous Structure
- muEDM** muon Electric Dipole Moment
- MPGD** Micro-Pattern Gaseous Detector
- MWPC** Multi-Wire Proportional Chamber
- OFTPC** Orthogonal Fields TPC
- PCB** Printed Circuit Board
- RASD** Reconstruction Assuming Steady Drift
- RHIC** Relativistic Heavy Ion Collider
- RICH** Ring Imaging Cherenkov Counter
- RK4** Runge-Kutta 4th order
- RPC** Resistive Plate Chamber
- RPWELL** Resistive Plate WELL
- rTPC** radial-drift TPC
- THGEM** THick GEM
- ToA** time-of-arrival
- ToT** time-over-threshold
- TPC** Time Projection Chamber

TPX3 Timepix3

μ-PIC Micro-Pixel Gas Chamber

μ-RWELL Micro-RWELL